UNIVERSITE PAUL CEZANNE AIX-MARSEILLE III
Ecole doctorale: Physique et Science De la Matière

TITLE

Optical microlenses and nanoantennas

THESE

to obtain the title of

PhD of Science of Aix-Marseille University

Speciality : Optics and photonics

Defended by

Alexis Devilez

on October, the 20^{th} 2010

Thesis supervised by Brian Stout and Nicolas Bonod

prepared at the Fresnel Institute

Jury :

Reviewers :	A. Femius Koenderink	-	AMOLF (Amsterdam, The Netherlands)
	Romain Quidant	-	ICFO (Barcelona, Spain)
Examinators :	Nicolas Bonod	-	Institut Fresnel (Marseille, France)
	Remi Carminati	-	Institut Langevin (Paris, France)
	Brian Stout	-	Institut Fresnel (Marseille, France)
	Gérard Tayeb	-	Institut Fresnel (Marseille, France)

Contents

Chapter 1
Introduction

The advances in nanosciences, and the improvement of nanofabrication techniques in particular, have strongly encouraged investigations of the optical properties of nanostructured components. In particular, small aggregates of particles and inclusions have emerged as key elements in nano-optical physics for the conception of new, efficient and compact optical components operating at micro-nanometer scale. This manuscript presents numerical studies employing particles for tailoring the electromagnetic interactions of light within the medium surrounding the particles.

A common approach to increase light matter/interactions consists in focusing light to small volumes in order to enhance the local electromagnetic intensity. A combination of convergent lenses or mirrors are commonly employed to achieve the high excitation rates required in a variety of applications such as fluorescent spectroscopy or optical datastorage. These systems however operate from the far field domain so that the focal zone is located far from the focusing system and involves only propagating light. The dimensions of the focal volumes obtained are consequently limited by diffraction effects (Rayleigh criterion). The use of small particles as near-field focusing systems provides highly compact and efficient systems that can furthermore utilize evanescent field contributions and the specific properties of metallic structures in the optical frequency range which support plasmon resonances. These latter resonances increase the interactions of light with nanometric particles which are much smaller than the incident optical wavelength. This results in strongly localized electromagnetic fields providing a potential downscaling of classical optical and electromagnetic devices.

Investigations of light interactions with such small systems require complete modeling techniques employing the electrodynamical theory of Maxwell. Our approach consists in generalizing Mie theory which is one of the few vectorial three-dimensional modal methods in electromagnetism enabling an analytical resolution of the Maxwell equations for spherical objects. It should be stressed that the results and methods presented in this manuscript are not restricted to spherical particles, but can be extended to non-spherical objects such as ellipsoids.

The studies in this manuscript required us to develop several extensions and modifications of generalized Mie theory. A matrix balancing method was developed in order to stabilize the numerical inversions involved in multiple scattering theory [1]. We elaborated a spectral development of vector multipolar waves on a plane wave basis in order to analyze the physical properties of highly focused beams and 'jets' [2]. Finally, we recently developed analytical formula for calculating the radiation enhancement properties of nano-antennas [3].

An important distinction is performed in this manuscript according to the respective dielectric (lossless) or metallic nature of the material composing the particles. Dielectric particles of micrometric dimensions will be investigated in this manuscript as efficient tools for 'focusing' light (*i.e.* concentrating light in small volumes) as an extension of classical macroscopic focusing systems such as microscope objectives. It will be demonstrated that a straightforward focusing of light

can be achieved by these compact dielectric systems in a non-resonant regime, thus operating in a large bandwidth frequency domain. It will be emphasized that this basic component produces a variety of intensity patterns in its near field according to characteristics of the incident illuminating beam. When illuminated by a plane wave, the focusing properties of the microsphere are notably adapted to optical datastorage or nanoparticles detection [2, 4], while under focused beam illumination, the resulting focal volume is suitable for enhancing fluorescent spectroscopy signals [5, 6]. This latter property is a striking result of the investigations performed during this PhD since we highlight that a surprising three-dimensional confinement of light can be achieved with this simple component [7, 8]. Nevertheless, although strong confinements can be obtained with these simple dielectric components, they are incommensurate with those achieved when employing metallic structures supporting electromagnetic resonances when illuminated at optical frequencies.

These resonances enhance the electromagnetic cross-sections of small metallic particles allowing light to interact with particles much smaller than the optical wavelength. The Localized Surface Plasmon Resonances (LSPRs) can be understood as resonant oscillations of the free electron gas of the particles creating charge density at their surface. This results in intense fields occurring in the vicinity of the particles producing focusing effects in nanometer scaled volumes. Strong couplings between individual localized plasmon resonances can provide even greater fields which are localized in the dielectric medium enclosed between the particles, thus providing efficient nanolensing effects. More interestingly, the strong interactions between individual localized plasmon resonances have recently attracted an additional interest since they enable an accurate control of the focal position with spatial resolutions on the order of $\lambda/10$ via the excitation of antisymmetric modes [9].

A question will consequently arise then as how a single active emitter will radiate in the presence of the nanoparticles? This topic has recently given rise to the concept of nanoantenna. This concept, analogous to radiofrequencies antennas consists in increasing the couplings between propagative radiations and single emitting systems such as fluorescent molecules or quantum dots. It can be then proven by invoking the reciprocity theorem, that spontaneous emission rates can be enhanced in the presence of resonant plasmonic nanoparticles. In addition, the strong interactions of an emitting dipole with a single nanoparticle or a chain of nanoparticles enable a redirection of light emission [10]. These properties will be investigated in the second part of the manuscript and it will result in a strategy to design optical antennas employing a judicious combination of dielectric and metallic materials [11].

CHAPTER 2

Transfer matrix for spherical scatterers

Contents

2.1 Introduction

Interaction of light with small particles has attracted much interest in optics. A major motivation for this problem can be found in the need to understand the atmospheric pertubations that affect astronomic observations and more generally that affect free space traveling wave detection [12]. Although these investigations were first undertaken to explain far field properties of disturbed radiations, the solution of the physical problem requires a microscopic modeling of the interactions.

A first approximation consists in neglecting the coherent interactions of light with the nearby object, thereby reducing the problem to the interaction of light with a single scatterer. Coherent multiple scattering that occurs when distance separations between the particles are small will be detailed later in chapter 5 in the framework of the Mie theory and multiple scattering equations. The multiple scattering method will still require the electromagnetic response of the individual object.

Rayleigh was the first to perform a dipolar approximation of the particle response in a quasistatic picture. This electrostatic approach provides an explanation of the blue coloration of the sky due to enhanced scattering of light at the small wavelengths of the optical range. The electrostatic response of small spherical particles will be detailed in chapter 5. However, this approach is insufficient for describing the scattering of light by particles of sizes close to the wavelength.

In 1908, Mie proposed an analytical solution of the vectorial electromagnetic problem of the interaction of light with spherical particles. The key idea consists in expanding the electromagnetic field upon vectorial spherical partial waves and verifying the EM boundary conditions. This historical period coincides with great advances in quantum and solid states physics and not surprisingly,

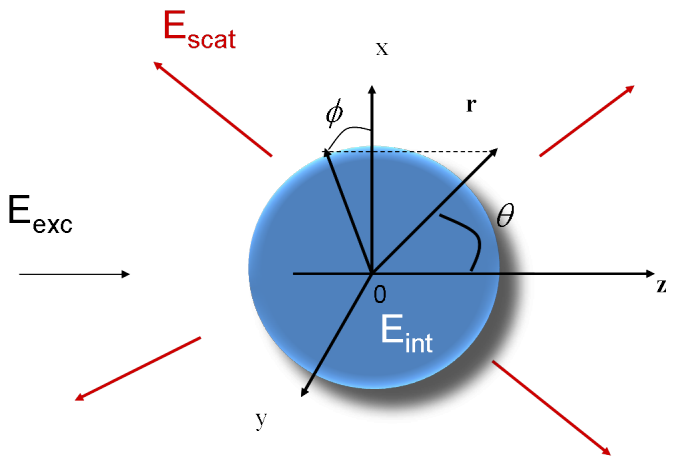

Figure 2.1: Sketch of the electromagnetic problem of light scattering by spherical objects. The external field is composed of the excitation field plus the scattered field. The spherical coordinates system is also displayed: the coordinates of a point (r, θ, φ) are defined in terms of the distance r, the inclination angle θ and the azimuthal angle φ.

strong analogies between the Lorentz-Mie formalism and electron interactions with atoms can be found. Indeed, Mie extended the concept of scalar spherical waves to vectorial spherical waves allowing a description of the electromagnetic field polarization. The spherical expansion then enables a straightforward satisfaction of the boundary conditions leading to a linear relation between the incident and the scattered field. A matrix formalism, that we will discuss later, enables the definition of a transfer matrix of the isolated particle independently of the applied excitation field. This transfer matrix contains all the optogeometrical informations required to describe the time harmonic electromagnetic response of the particle and will be combined with multiple scattering equations in chapter 5 to accurately calculate the EM field in aggregates of arbitrary sized spherical particles.

It must be stressed that only a few number of modal and thus analytical solutions exist to tackle three-dimensional problems in electromagnetism. Although, the analytical framework introduces specificity about shape of the particles, it also enables rapid calculations of the fields. All the numerical simulations presented in this manuscript have been performed using a modal Mie theory. A modular FORTRAN code has been developed to give a rapid access to various physical parameters such as the field intensity, the electromagnetic cross sections or the Poynting vectors. This chapter aims to review the fundamentals of the Mie theory by defining the elements of the transfer matrix for a single scatterer and provides references to publications containing further details. Since the transfer matrix is defined on the basis set of vectorial multipolar waves, the question of the expansion of the excitation field is of fundamental importance. A variety of excitation fields generated from the far field are currently employed in nano-optics such as plane waves or focused beams. One also encounters near-field excitation such as the dipole emission of fluorophores and quantum dots as well as evanescent fields. All these excitation fields will be defined in terms of the vector spherical waves.

In addition, the modal method gives a straightforward access to the eigen-modes of the spherical

structure. Such modes, frequently called Whispering Gallery Modes, have been intensively investigated for their high quality factors of practical interest for biosensing [13], lasing systems [14, 15] or EM transport via Coupled Resonator Optical waveguide (CROW) [16]. These resonances are directly related to Mie coefficients and it appears relevant to begin this manuscript by recalling properties of these well-known resonances.

2.2 Generalized Mie Theory

The Mie theory is based on an analytical solution of the Helmholtz equation in spherical coordinates for EM vector fields. The solutions (or eigen-vectors of the Maxwell propagation equation) will provide a relevant basis of vector functions for solving the boundary conditions at a spherical interface. In a source free homogeneous, non magnetic medium. The time harmonic Maxwell equations yields that the electric field must satisfy the Maxwell propagation equation:

$$\nabla \times (\nabla \times \mathbf{E}) - k_b^2 \mathbf{E} = 0 \tag{2.1}$$

where $k_b = \sqrt{\varepsilon_b \mu_b}\omega/c = 2\pi n_b/\lambda_0$ is the associated wavenumber in the source free homogeneous medium (λ_0 is the wavelength in vacuum).

2.2.1 Scalar resolution in spherical coordinates

As a first step, we solve the homogeneous Helmholtz equation in the scalar case, the vectorial solutions will then be obtained from the scalar solution:

$$\triangle \varphi + k_b^2 \varphi = 0 \tag{2.2}$$

where φ is the scalar wave function. The solution in spherical coordinates is fully detailed in [17]. The separation of the radial and angular variables in spherical coordinates leads to resolving two independent differential equations. Furthermore, two independent solutions are required to provide a complete basis for an arbitrary solution of Eq. (2.2):

$$Rg\left\{\varphi_{n,m}(k_b \mathbf{r})\right\} \equiv j_n(k_b \mathbf{r}) Y_{n,m}(\theta, \phi) \tag{2.3}$$

$$\varphi_{n,m}(k_b \mathbf{r}) \equiv h_n^+(k_b \mathbf{r}) Y_{n,m}(\theta, \phi) \tag{2.4}$$

where $j_n(x)$ are the first kind spherical Bessel functions and $h_n^+(x) = j_n(x) + iy_n(x)$ are the outgoing spherical Hankel functions defined using the $y_n(x)$ second kind spherical Bessel functions. They can be defined in terms of the cylindrical Bessel functions $J_n(x)$ and $H_n(x)$ as:

$$j_n(x) \equiv \left(\frac{\pi}{2x}\right)^{1/2} J_{n+1/2}(x) \tag{2.5}$$

$$h_n^+(x) \equiv \left(\frac{\pi}{2x}\right)^{1/2} H_{n+1/2}^+(x) \tag{2.6}$$

It should be noticed that the Hankel functions $h_n^+(x) = j_n(x) + iy_n(x)$ have an essential singularity when $x \to 0$. The regular parts $Rg\{h_n^+(x)\} = j_n(x)$ do not diverge for any finite value of x. Although one could build a complete basis set using these two Bessel functions $j_n(x)$ and $y_n(x)$, the $h_n^+(x)$ Bessel functions provide a more physical solution since they correspond to outgoing propagating waves. The $Y_{n,m}(\theta, \phi)$ are the normalized spherical harmonics defined using associated Legendre functions:

$$Y_{n,m}(\theta, \phi) \equiv P_n^m(\cos\theta)e^{im\phi} \tag{2.7}$$

It can be observed that the solutions are characterized by two quantum integers n and m resulting from constraints associated with the separation of the radial and the angular variables. This is fully analogous to the three dimensional Shrödinger equation leading to an angular quantization of the electronic eigenmodes.

$$n = 0, 1...., \infty \quad \text{et } m = -n, ...n$$

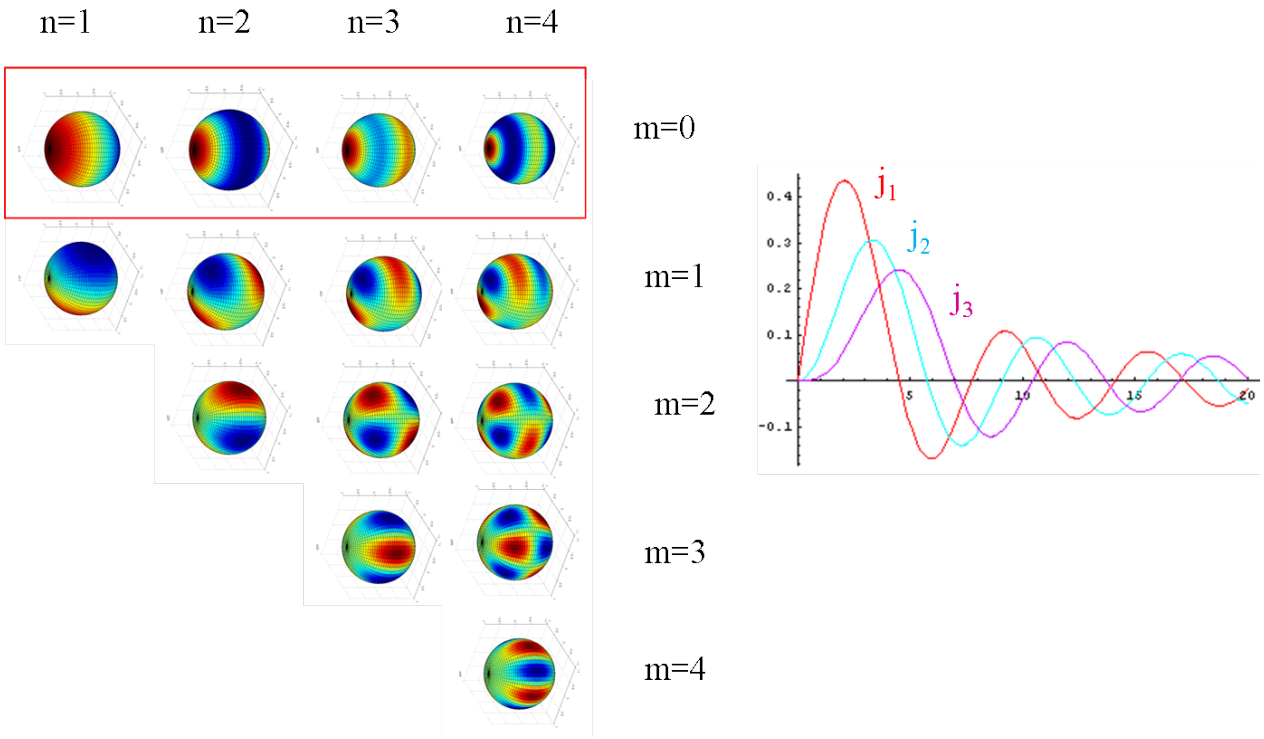

Figure 2.2: (a) Colored illustration of the angular dependence of the amplitude of scalar spherical harmonics and (b) radial dependence of the spherical Bessel functions j_1, j_2 and j_3.

Fig. 2.2 graphically illustrates the angular dependence of the spherical harmonics $Y_{n,m}(\theta, \phi)$ and the radial dependency of the scalar solution $\varphi(x)$. The amplitude of the scalar spherical harmonics over a unitary spherical surface is displayed in Fig. 2.2(a) for the four first orders (i.e $n = 1$ to $n = 4$) and the first kind Bessel function is displayed from $n = 1$ to $n = 3$. Increasing the multipole orders enables to describe more rapid angular variations of the field.

2.2.2 Vectorial Multipolar Waves and Vector Spherical Harmonics (VSHs)

2.2.2.1 Vector Spherical waves

From the scalar solution, one can construct a vectorial wave solution by defining:

$$\mathbf{M}_{n,m}(k_b\mathbf{r}) \equiv \frac{\nabla \times [\mathbf{r}\varphi_{n,m}(k_b\mathbf{r})]}{\sqrt{n(n+1)}} \tag{2.8}$$

$$\mathbf{N}_{n,m}(k_b\mathbf{r}) \equiv \frac{\nabla \times \mathbf{M}_{n,m}(k_b\mathbf{r})}{k_b} \tag{2.9}$$

2.2.2.2 Vector Spherical Harmonic Functions

It is also convenient to define the Vector Spherical Harmonics Functions (VSHs):

$$\mathbf{r} = r\widehat{\mathbf{r}}$$

$$\mathbf{Y}_{n,m}(\theta,\phi) \equiv Y_{n,m}(\theta,\phi)\widehat{\mathbf{r}} \tag{2.10}$$

$$\mathbf{X}_{n,m}(\theta,\phi) \equiv \mathbf{Z}_{n,m}(\theta,\phi) \times \widehat{\mathbf{r}} \tag{2.11}$$

$$\mathbf{Z}_{n,m}(\theta,\phi) \equiv \frac{r\nabla Y_{n,m}(\theta,\phi)}{\sqrt{n(n+1)}} \tag{2.12}$$

The Vector Spherical Harmonics define a complete orthogonal basis for describing the angular variations for any vector field. The outgoing vector spherical waves can be written in terms of the VSHs:

$$\mathbf{M}_{n,m}(k_b\mathbf{r}) \equiv h_n^+(k_b\mathbf{r})\mathbf{X}_{n,m}(\theta,\phi) \tag{2.13}$$

$$\mathbf{N}_{n,m}(k_b\mathbf{r}) \equiv \frac{1}{k_b r}[\sqrt{n(n+1)}h_n^+((k_b\mathbf{r}))\mathbf{Y}_{n,m}(\theta,\phi) + \xi_n'((k_b\mathbf{r}))\mathbf{Z}_{n,m}(\theta,\phi)] \tag{2.14}$$

where we have introduced the Riccati-Bessel functions:

$$\begin{gathered}\psi_n(x) \equiv x j_n(x) \quad \text{and its derivative} \quad \psi_n'(x) \equiv j_n(x) + x j_n'(x) \\ \xi_n(x) \equiv x h_n^+(x) \quad \text{and its derivative} \quad \xi_n'(x) \equiv h_n^+(x) + x[h_n^+(x)]'\end{gathered}$$

The regular solutions can be written:

$$Rg\{\mathbf{M}_{n,m}(k_b\mathbf{r})\} \equiv j_n(k_b\mathbf{r})\mathbf{X}_{n,m}(\theta,\phi) \tag{2.15}$$

$$Rg\{\mathbf{N}_{n,m}(k_b\mathbf{r})\} \equiv \frac{1}{k_b r}[\sqrt{n(n+1)}j_n((k_b\mathbf{r}))\mathbf{Y}_{n,m}(\theta,\phi) + \psi_n'((k_b\mathbf{r}))\mathbf{Z}_{n,m}(\theta,\phi)] \tag{2.16}$$

2.2.3 Field expansion in homogeneous media

We have constructed a basis set of vector wave solutions of the vector Maxwell propagation equation. Any vector wave solution can be expanded on a set of multipolar eigenwaves. The incident field is commonly expanded on the regular waves:

$$\mathbf{E}_{\text{inc}} = E \sum_{n=1}^{\infty} \sum_{m=-n}^{n} [Rg\{\mathbf{M}_{n,m}(k_b\mathbf{r})\}a_{n,m}^{(h)} + Rg\{\mathbf{N}_{n,m}(k_b\mathbf{r})\}a_{n,m}^{(e)}] \tag{2.17}$$

where $a_{n,m}^{(h)}$ et $a_{n,m}^{(e)}$ are the respective coefficients of $\mathbf{E}_{\text{inc}}$ according to $Rg\{\mathbf{M}_{n,m}(k_b\mathbf{r})\}$ and $Rg\{\mathbf{N}_{n,m}(k_b\mathbf{r})\}$.

In a similar manner, the internal field can be expanded on the regular multipolar waves with the coefficients $s_{n,m}^{(e)}$ and $s_{n,m}^{(h)}$. One can easily assume that the field scattered by the object is an outgoing field. The scattered field is then described using the outgoing multipolar waves:

$$\mathbf{E}_{\text{scat}} = E \sum_{n=1}^{\infty} \sum_{m=-n}^{n} [\mathbf{M}_{n,m}(k_b\mathbf{r})f_{n,m}^{(h)} + \mathbf{N}_{n,m}(k_b\mathbf{r})_{n,m}^{(e)}] \tag{2.18}$$

where $f_{n,m}^{(h)}$ et $f_{n,m}^{(e)}$ are the respective coefficients of $\mathbf{E}_{\text{scat}}$ developped on $\mathbf{M}_{n,m}(k_b\mathbf{r})$ and $\mathbf{N}_{n,m}(k_b\mathbf{r})$. One can introduce a matrix formalism, by placing the VSWs as elements of a row vector:

$Rg\{\mathbf{\Psi}^t(k_b\mathbf{r})\} \equiv \{Rg\{\mathbf{M}_1\}, ..., Rg\{\mathbf{M}_\infty\}, Rg\{\mathbf{N}_1\}, ..., Rg\{\mathbf{N}_\infty\}\}$

while placing the coefficients in a column vector:

$$a = \begin{bmatrix} \vdots \\ a_p^{(h)} \\ \vdots \\ a_p^{(e)} \\ \vdots \end{bmatrix}$$

We have introduced a single integer index $p \equiv n(n+1) - m$ to replace the two integer indices n, m. This transformation has the following inverse relations: $n(p) = \sqrt{p}$ and $m(p) = -p + n(n+1)$. With this matrix notation, one can write the incident field in a compact manner:

$$\mathbf{E}_{\text{inc}} = ERg\{\mathbf{\Psi}^t(k_b\mathbf{r})\}a \tag{2.19}$$

In a more general manner, one can define the excitation field on an object (j) as the total field minus the field scattered by the object itself:

$$\mathbf{E}_{\text{exc}}^{(j)} = ERg\{\mathbf{\Psi}^t(k_b\mathbf{r}_j)\}e^{(j)} \tag{2.20}$$

where $\mathbf{r}_j \equiv \mathbf{r} - \mathbf{x}_j$ and $\mathbf{x}_j$ is the position of the center of the scattering object. This definition will be particularly useful in the context of multiple scattering (c.f. Appendix A). For a single scatterer, the incident and excitation field are the same.

The field inside the object j can be similarly expressed:

$$\mathbf{E}_{\text{int}}^{(j)} = ERg\{\mathbf{\Psi}^t(k_s\mathbf{r})\}s^{(j)} \tag{2.21}$$

where k_s is the wavenumber inside the particle defined as $k_s = n_s/n_b k_b$ with n_s the refractive index of the particle and $k_b = 2\pi n_b/\lambda_0$ is the wavevector in the background medium, with n_b the refractive index of the surrounding medium and λ_0 the wavelength in vacuum. The scattered field is expressed as:

$$\mathbf{E}^{(j)}_{\text{scat}} = E\boldsymbol{\Psi}^t(k_b\mathbf{r}_j)f^{(j)} \tag{2.22}$$

The "regular" part is not required here since the field scattered by the object is an outgoing wave.

2.2.4 Generalized Mie Theory: T-Matrix of an isotropic sphere

We define the transfert matrix $t^{(j)}$ of an object j as the matrix relation between the excitation and the scattered field coefficients:

$$f^{(j)} \equiv t^{(j)}e^{(j)} \tag{2.23}$$

2.2.4.1 Calculations of the field components in the vector spherical harmonics basis: boundary conditions.

To obtain the components of the scattered field as a function of the incident field, the boundary conditions need to be solved. These interface conditions are easily solved using the expansion on the vector spherical harmonics.

$$\mathbf{E}(\mathbf{r}) = \sum_{n=0}^{\infty}\sum_{m=-n}^{n}\left[E^{(Y)}_{n,m}(r)\mathbf{Y}_{n,m}(\theta,\phi) + E^{(X)}_{n,m}(r)\mathbf{X}_{n,m}(\theta,\phi) + E^{(Z)}_{n,m}(r)\mathbf{Z}_{n,m}(\theta,\phi)\right] \tag{2.24}$$

$$= \sum_{p=0}^{\infty}\left[E^{(Y)}_{p}\mathbf{Y}_{p}(\theta,\phi) + E^{(X)}_{p}\mathbf{X}(\theta,\phi) + E^{(Z)}_{p}\mathbf{Z}(\theta,\phi)\right] \tag{2.25}$$

The VSHs basis is orthogonal and a straightforward identification between equations (2.13, 2.14) and 2.24 shows that the radial functions of the external field are:

$$E^{(Y)}_{e,p}(r) = E\sqrt{n(n+1)}\left[\frac{j_n(k_b r)}{k_b r}e^{(e)}_p + \frac{h^+_n(k_b r)}{k_b r}f^{(e)}_p\right] \tag{2.26}$$

$$E^{(X)}_{e,p}(r) = \frac{E}{k_b r}\left[\psi_n(k_b r)e^{(h)}_p + \xi_n(k_b r)f^{(h)}_p\right]$$

$$E^{(Z)}_{e,p}(r) = \frac{E}{k_b r}\left[\psi'_n(k_b r)e^{(e)}_p + \xi'_n(k_b r)f^{(e)}_p\right]$$

The expansion inside the sphere gives

$$E^{(Y)}_{s,p}(r) = E\sqrt{n(n+1)}\frac{j_n(k_s r)}{k_s r}s^{(e)}_p \tag{2.27}$$

$$E^{(X)}_{s,p}(r) = \frac{E}{k_s r}\psi_n(k_s r)s^{(h)}_p$$

$$E^{(Z)}_{s,p}(r) = \frac{E}{k_s r}\psi'_n(k_s r)s^{(e)}_p$$

On can deduce the components of the corresponding magnetic field $\mathbf{H}$ thanks to the Maxwell-Faraday equation

$$\mathbf{H} = \frac{1}{i\omega\mu_0\mu_r}(\nabla \times \mathbf{E}) \tag{2.28}$$

and utilizing the following relations for the curl of the VSWFs

$$\begin{aligned} \nabla \times \mathbf{M}_p(k_b\mathbf{r}) &= k_b\mathbf{N}_p(k_b\mathbf{r}) \\ \nabla \times \mathbf{N}_p(k_b\mathbf{r}) &= k_b\mathbf{M}_p(k_b\mathbf{r}) \end{aligned} \tag{2.29}$$

We can then deduce the expansion of the excitation and scattered magnetic fields:

$$\mathbf{H}_{\text{scat}}(\mathbf{r}) = \frac{k_b}{i\omega\mu_e\mu_0}E\sum_{p=1}^{\infty}\left[\mathbf{N}_p(k_b\mathbf{r})f_p^{(h)} + \mathbf{M}_p(k_b\mathbf{r})f_p^{(e)}\right] \tag{2.30}$$

$$\mathbf{H}_{\text{exc}}(\mathbf{r}) = \frac{k_b}{i\omega\mu_e\mu_0}E\sum_{p=1}^{\infty}\left[Rg\left\{\mathbf{N}_p(k_b\mathbf{r})\right\}e_p^{(h)} + Rg\left\{\mathbf{M}_p(k_b\mathbf{r})\right\}f_p^{(e)}\right] \tag{2.31}$$

And in the same manner as the electric field, we deduce the $\mathbf{H}$ field components both outside,

$$\begin{aligned} H_{e,p}^{(Y)}(r) &= \frac{a_p}{i\omega\mu_0\mu_b}\frac{E}{r}\left[j_n(k_br)e_p^{(h)} + h_n^+(k_br)f_p^{(h)}\right] \\ H_{e,p}^{(X)}(r) &= \frac{1}{i\omega\mu_0\mu_e}\frac{E}{r}\left[\psi_n(k_br)e_p^{(e)} + \xi_n(k_br)f_p^{(e)}\right] \\ H_{e,p}^{(Z)}(r) &= \frac{1}{i\omega\mu_0\mu_e}\frac{E}{r}\left[\psi_n'(k_br)e_p^{(h)} + \xi_n'(k_br)f_p^{(h)}\right] \end{aligned}$$

and inside the sphere:

$$\begin{aligned} H_{s,p}^{(Y)}(r) &= \frac{\sqrt{n(n+1)}}{i\omega\mu_0\mu_s}\frac{E}{r}j_n(k_sr)s_p^{(h)} \\ H_{s,p}^{(X)}(r) &= \frac{1}{i\omega\mu_0\mu_s}\frac{E}{r}\psi_n(k_sr)s_p^{(e)} \\ H_{s,p}^{(Z)}(r) &= \frac{1}{i\omega\mu_0\mu_s}\frac{E}{r}\psi_n'(k_sr)s_p^{(h)} \end{aligned}$$

One should remark that $E_p^{(Y)}(r)\mathbf{Y}_p(\theta,\phi)$ and $H_p^{(Y)}(r)\mathbf{Y}_p(\theta,\phi)$ are directed normally to a spherical surface while $E_p^{(X)}(r)\mathbf{X}(\theta,\phi)$, $E_p^{(Z)}(r)\mathbf{Z}(\theta,\phi)$, $H_p^{(X)}(r)\mathbf{X}(\theta,\phi)$ and $H_p^{(Z)}(r)\mathbf{Z}(\theta,\phi)$ are tangential to it.

The VSHs basis is orthogonal so that the continuity of the tangential components of $\mathbf{E}$ and $\mathbf{H}$ is:

$$E_{e,p}^{(X)}(r) = E_{s,p}^{(X)}(r),\ E_{e,p}^{(Z)}(r) = E_{s,p}^{(Z)}(r) \tag{2.32}$$

$$H_{e,p}^{(X)}(r) = H_{s,p}^{(X)}(r),\ H_{e,p}^{(Z)}(r) = H_{s,p}^{(Z)}(r) \tag{2.33}$$

2.2.4.2 Elements of the T-matrix for a single spherical particle

The coordinates f_p can be then expressed in terms of the e_p coefficients by imposing the continuity of the tangential **E** and **H** fields and eliminating the internal coefficients s_p :

$$f_p^{(h)} = \frac{\mu_s \psi_n'(k_e R)\psi_n(k_s R) - \rho_s \mu_e \psi_n'(k_s R)\psi_n(k_e R)}{\rho_s \mu_e \psi_n(k_s R)\xi_n'(k_e R) - \mu_s \xi_n(k_e R)\psi_n'(k_s R)} e_p^{(h)} \equiv t_n^{(h)} e_p^{(h)} \tag{2.34}$$

$$f_p^{(e)} = \frac{\mu_s \psi_n'(k_s R)\psi_n(k_b R) - \rho_s \mu_b \psi_n'(k_b R)\psi_n(k_s R)}{\rho_s \mu_b \psi_n(k_s R)\xi_n'(k_b R) - \mu_s \xi_n(k_b R)\psi_n'(k_s R)} e_p^{(e)} \equiv t_n^{(e)} e_p^{(e)} \tag{2.35}$$

where $\rho_s \equiv \frac{k_s}{k_b} = n_s/n_b$ is the refractive index contrast parameter.

These can be expressed in a matrix form:

$$\begin{bmatrix} f_p^{(h)} \\ f_p^{(e)} \end{bmatrix} = t \begin{bmatrix} e_p^{(h)} \\ e_p^{(e)} \end{bmatrix} \tag{2.36}$$

where the individual t-matrix for an isolated scatterer $[t]$ is a diagonal matrix:

$$[t] = \begin{bmatrix} t_n^{(h)} & 0 \\ 0 & t_n^{(e)} \end{bmatrix} \tag{2.37}$$

We use the lower-case t here to distinguish it from the multiple scattering T-matrix treated later on. The t-matrix for a single spherical scatterer has been readily obtained thanks to the Vector Spherical Harmonics. This t-matrix contains all the opto-geometrical properties of the spherical particle and provides a description of the particle response independently of the incident field. One can then change the features of the incident field without recalculating the t-matrix. Furthermore, this approach will prove practical benefits for treating the multiple scattering of light in aggregates of particles (see Appendix A).

2.2.4.3 Plane waves expression in the multipolar framework

One readily remarks that a multipole expansion of a plane wave field is not trivial. In particular, the expansion of a plane wave over all space requires an infinite number of multipole orders. The coefficients of an incident plane wave on the multipole expansion can be written as [17]:

$$a_{n,m}^{(h)} = 4\pi i^n \mathbf{X}_{n,m}^*(\theta_k, \varphi_k).\widehat{\mathbf{e}_i} \tag{2.38}$$

$$a_{n,m}^{(e)} = 4\pi i^{n-1} \mathbf{Z}_{n,m}^*(\theta_k, \varphi_k).\widehat{\mathbf{e}_i} \tag{2.39}$$

where θ_k and φ_k give the direction of the incident wave-vector $\mathbf{k}_{\text{inc}}$. Although the plane wave expansion on multipolar waves requires an infinite numbers of multipole, a finite number of multipoles is sufficient for a local expansion close to a particle.

2.2.4.4 Davis expansion of focused beam on the multipolar framework

The multipolar expansion of focused beams by classical microscope objectives, in the manuscript, is based on Davis-type approach [18] extended to the non-paraxial domain. In this approach, one adopts a vector potential analysis which automatically imposes $div(\mathbf{E}) = 0$ to a given order in s where $s \equiv \frac{1}{2k_b z_r} \equiv \tan\theta_0/2$ is the dimensionless beam shape parameter, with z_r the Rayleigh length of the focused beam and θ_0 is the opening angle of the numerical aperture. For an axisymmetric power density, it leads to the following expansion in the VSWF framework:

$$a_{n,m}^{(h)} = 4\pi i^n g_n(s)\mathbf{X}_{n,m}^*(\theta,\varphi).\widehat{\mathbf{e}_i} \tag{2.40}$$

$$a_{n,m}^{(e)} = 4\pi i^{n-1} g_n(s)\mathbf{Z}_{n,m}^*(\theta,\varphi).\widehat{\mathbf{e}_i} \tag{2.41}$$

where the g_n are beam structure coefficients describing the beam shape. If we furthermore impose a Lorenzian distribution of the axial beam intensity, g_n is equal to:

$$g_n(s) = \frac{i^{-n+1}[j_{n-1}(\frac{i}{2s^2}) - \frac{2s^2}{i}(n+1)j_n(\frac{i}{2s^2})]}{2s^2[(1+8s^4)\sinh(\frac{1}{2s^2}) - 4s^2\cosh(\frac{1}{2s^2})]} \tag{2.42}$$

A first approximation was made by Gousebet *et al.* [19–21] in the context of so-called localized approximation:

$$g_n(s) = e^{-s^2(n-1)(n+2)} \tag{2.43}$$

leading to the expansion in the VSW framework:

$$\begin{aligned} a_{n,m}^{(h)} &= 4\pi i^n e^{-s^2(n-1)(n+2)}\mathbf{X}_{n,m}^*(\theta,\varphi).\widehat{\mathbf{e}_i} \\ a_{n,m}^{(e)} &= 4\pi i^{n-1} e^{-s^2(n-1)(n+2)}\mathbf{Z}_{n,m}^*(\theta,\varphi).\widehat{\mathbf{e}_i} \end{aligned}$$

This simple formula agrees relatively well with the exact results given in Eq. (2.42) for s up to 0.25 corresponding to a divergence angle of 30°. Due to its simplicity, we will employ this approximation for modeling highly focused beams even though for large apertures, Eq. (2.42) gives more realistic results. Several theoretical studies have investigated more realistic beams. Such modelings however require specific modeling of the given experimental configuration [22, 23] and the previous formulation remains a first order approximation that enables rapid and simple modeling of a focused beam. Although the Davis approach is reputed to fail for tightly focused beams, experimental measurements correlated with our numerical simulations (c.f. section 4.2) tend to validate this choice.

2.3 Multipolar resonances: Whispering Gallery Modes

In the previous section, we have obtained an analytical relation between the incident excitation coefficients and the scattered field coefficients (Eq. (2.34) and Eq. (2.35)). The Mie coefficients establish a relation that remains valid for any type of spherical particles even with complex permittivity such as metals. In this manuscript, both metallic and dielectric materials will be modeled in this framework. In the first part of the manuscript, only purely dielectric materials are studied (the

refractive index is real) so that no dissipation occurs in the particle. However, it is important to realize that the refractive index of the spherical object strongly influences its scattering properties. The focusing properties of dielectric microspheres in low refractive contrasts conditions will be investigated in chapter 3.

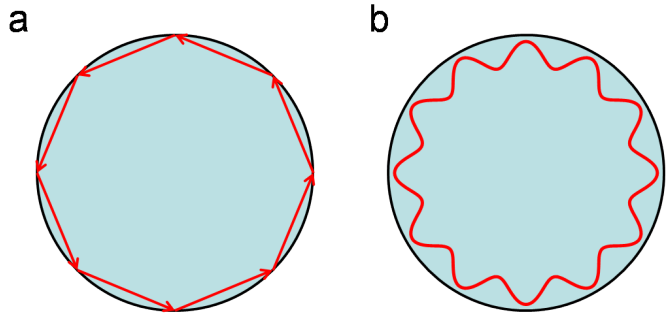

Figure 2.3: (a) Layout of the geometric interpretation of Whispering Gallery Modes: internal reflections are responsible for trapping light inside the particle. (b) Layout of the wave interpretation of Whispering Gallery Modes: a standing wave is established leading to resonant fields inside the particle.

Morphological resonances were first investigated in the context of sound waves by Lord Rayleigh to explain properties of so called whispering galleries. Indeed, the circular or ellipsoidal domes of such large rooms permit whispers from one person to be clearly heard in any location close to the walls of the room. Rayleigh showed that standing waves resonances were created in the circular cavity enhancing the amplitude of the field around the cavity. These resonances have been consequently called Whispering Gallery Modes (WGMs). Excitation of WGMs in the visible range in spherical micrometric cavities attracted a particular interest in the 60's since the high quality factors [24, 25] of the resonances enable intense fields inside the particle. Quality factors of 10^9 principally limited by the intrinsec absorption in the material have been observed and spherical microparticles have been since investigated for molecular sensing [13], lasing systems [14, 15], optical waveguiding [16, 26, 27] and delay lines [28].

Oscillating systems have specific resonant frequencies at which, a driving force produces large oscillating response even for weak applied amplitudes. Since the Mie coefficients link the coordinate vector of the scattered field to the incident field, they should exhibit maxima at their resonance frequencies. Let us focus our attention on the Mie coefficients (Eq. (2.44) and Eq. (2.45)). These coefficients have denominators which exhibit numerous zeros for complex values of k_bR. The spectral position as well as the strength of these resonances depend both on k_bR and on the contrast ratio $\rho = n_s/n_b$.

$$t_n^{(h)} \equiv \frac{\mu_s \psi_n'(k_bR)\psi_n(k_sR) - \rho_s\mu_b\psi_n'(k_sR)\psi_n(k_bR)}{\rho_s\mu_b\psi_n(k_sR)\xi_n'(k_bR) - \mu_s\xi_n(k_bR)\psi_n'(k_sR)} \tag{2.44}$$

$$t_n^{(e)} \equiv \frac{\mu_s \psi_n'(k_sR)\psi_n(k_bR) - \rho_s\mu_b\psi_n'(k_bR)\psi_n(k_sR)}{\rho_s\mu_b\psi_n(k_sR)\xi_n'(k_bR) - \mu_s\xi_n(k_bR)\psi_n'(k_sR)} \tag{2.45}$$

These zeros can be first distinguished according to the mode number n involved. Fig. 2.4 shows the amplitude map of the magnetic coefficients of order 6, $|t_6^{(h)}|$ when $k_bR = 2\pi n_bR/\lambda_0$ varies in the complex plane, for a microsphere of diameter 2 μm and of refractive index $n_s = 2$. The distribution is given in terms of the real part (horizontal axis) and the imaginary part (vertical axis) of the incident wavelength. One can notice that several peaks can be observed for different real values of the wavelength. The corresponding imaginary part illustrates the confinement of the field inside the particle and the width of the corresponding resonance on the real axis is directly related to the amplitude of the imaginary part [29, 30]. Magnetic coefficients have been displayed here because they have a weaker imaginary part than the electric coefficients so that they are more easily coupled with the external field.

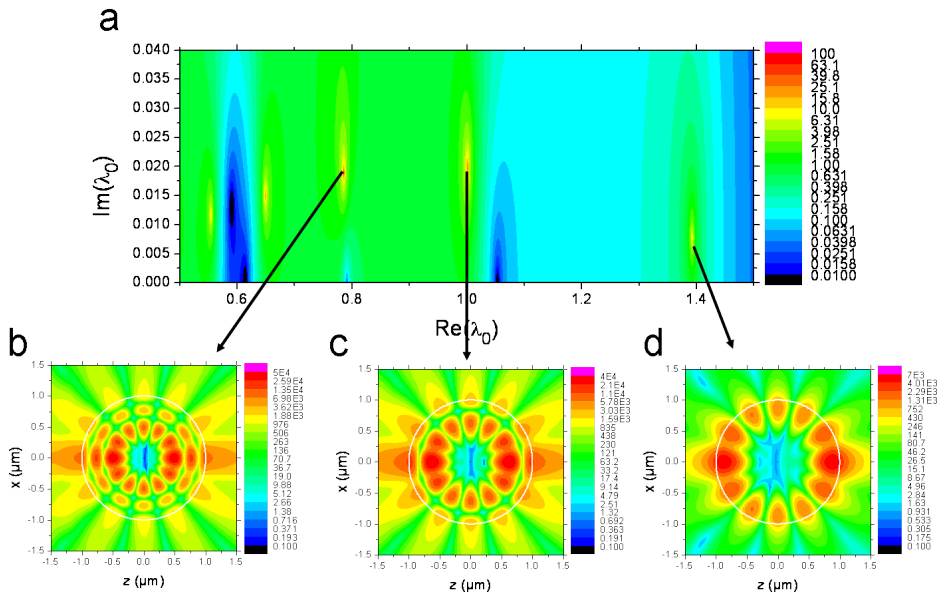

Figure 2.4: (a) Amplitude map of the magnetic coefficients $|t_6^h|$ when $k_bR = 2\pi n_bR/\lambda_0$ varies in the complex plane. The refractive index of the 2 μm diameter microsphere is set to $n_s = 2$ and the distribution is given in terms of the real part (horizontal axis) and the imaginary part (vertical axis) of the incident wavelength. (b), (c) and (d) Intensity maps for complex illumination for the first order resonances occuring at respectively (b) $\lambda_0 = 0.786 + i*0.0188$, (c) $\lambda_0 = 1.0017 + i*0.02$ and (d) $\lambda_0 = 1.392 + i*0.0078$.

Intensity maps of the electric field are displayed in Fig. 2.4 for three different resonances, at (b) $\lambda_0 = 0.786 + i*0.0188$, (c) $\lambda_0 = 1.0017 + i*0.02$ and (d) $\lambda_0 = 1.392 + i*0.0078$. These maps show that strong intense fields occur inside the particle. The resonance at the longer wavelength (Fig. 2.4(d)) shows a single circular field confined at the internal surface of the microsphere. The standing waves established in the particle exhibits $2n = 12$ highly intense peaks regularly distributed along the surface. For smaller wavelengths,(Fig. 2.4(b)and (c)) several rings are produced in the particle. The numbers of peak along the radial direction is so called the order of the resonance l. The lowest order $l = 1$ corresponds to Fig. 2.4(d) and a decrease wavelength enables the excitation of higher order resonance as $l = 2$ in Fig. 2.4(c) and $l = 3$ in Fig. 2.4(b).

A formal analogy can be made with quantum mechanism. As mentioned in the introduction, Mie formulation is strongly analog to the elastic scattering of electron waves on an atom. In the same manner as an electron can be coupled into atomic eigenstate and confined around the nucleus, the photon can be coupled to quantified eigen modes in the dielectric particles. The refractive index acts as a potential well that trap the electromagnetic field in the orbital region of the dielectric particle [29]. The available states depend on the energy of the incident wave that can be distributed over high order orbitals.

2.4 Conclusion

In this chapter, the fundamental elements of the generalized Mie theory have been reported. The expansion of the electromagnetic field on the Vector Spherical Waves enables the analytical resolution of boundaries conditions. As a result, all the scattering properties of spherical objects are encompressed in a transfer matrix matricial formalism independent of the incident field. Calculations performed in this manuscript will employ this framework. As an example, we have investigated morphological resonances occuring in spherical dielectric particles and pointed out the close relation with the elements of the T-matrix. In the next chapters, the Mie theory will be employed to investigate various situations such as light focusing by low refractive index particles (chapter 3 and chapter 4) and interactions of light with metallic nanoparticles (chapter 5 to chapter 7).

CHAPTER 3

Focusing light with near-field operating microlens

Contents

3.1 Introduction to focusing systems

Convergent dielectric lenses such as glass lenses can be considered as the most common optical components. As an example, magnifying lenses have been commonly employed to produce a magnified image of the object of interest. Sherlock Holmes is the most famous example of the popular usage of this particular type of lenses but its invention is said to date at least from the XV^{th} century before J.C. Although, this simple object is no longer employed in modern optics, this well-known object can in a first approach illustrate our purpose about light focusing.

We know that a magnifying lens may set fire to an underneath object during a sunny day. In this case, the incident light enters the system and is concentrated in the focal region. Consequently, the light energy density is increased in the focal region increasing by the way potential interactions between light and matter. Currently, light focusing is employed for applications such as data storage, optical nanopatterning or in biophotonic for fluorescence spectroscopy. In this manuscript, we

are more interested in increasing light/matter interactions rather than in producing a perfect two-dimensional image. In particular, we are interested in focusing light using spherical micrometric lenses.

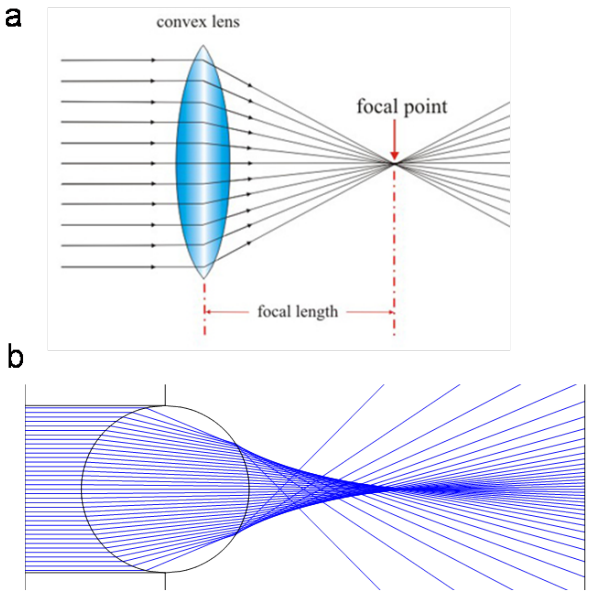

Figure 3.1: (a) Schematic of an ideal lens in the geometrical approximation. The incident plane wave is focused in a single focal point. (b) Geometrical ray tracing of a spherical lens performed using the commercial software *ZEMAX* . Rays converge at different positions on the optical axis, illustrating the geometric spherical aberration.

Considering an ideal convergent lens in the geometric approximation as illustrated in Fig. 3.1(a), the propagating incident light would be focused in a single position called the focal point. Such focusing remains an ideal case and focusing systems may suffer from geometrical aberrations at large opening angles. In particular, spherical lenses have not often been employed to focus light since they intrinsically suffer from strong geometrical aberrations. The ray tracing for a spherical lens performed using the commercial software *ZEMAX* displayed in Fig. 3.1(b) shows a typical spherical aberration. It is easy to notice that light rays are not focused at the same position along the optical axis. This shows that spherical lenses are not suitable for focusing light particularly for rays crossing the lens far from the optical axis (also called non-paraxial domain).

Modern optical systems have been since corrected from the major geometrical aberrations [31] but other limitations remain. Indeed, even perfectly corrected systems have to face the fundamental diffraction limit when attempting to focus light in very small volumes. The focal volumes of tighlty focused beams result from the interferences of propagating electromagnetic waves and the spatial variations in the field distribution depend directly on the incident wavevectors of the focused beam as well as on the relative phase of the different contributions. The achievement of small focal volumes requires high angular openings objectives as well as the phase matching of the incident angular components to produce a clear focal volume. The correction of diffraction aberrations [32] will result in a minimal focal volume on the order of the incident wavelength and a fundamental

boundary spatial resolution of optical systems is given by the Rayleigh limit. Perfectly corrected systems such as state of art high numerical microscope objectives enable to concentrate light in volumes as small as $(\lambda/2)^3$ but at the price of complex optical systems.

Focusing of light is currently employed to produce extremely localized effects such as material damaging for data storage (CD, DVD, BluRays), or laser surgery, and a need for compact and cost effective materials is needed. The advances in nanofabrication technics and the fundamental limitations of far field focusing systems recommend the use of near field and compact operating microlenses to focus light.

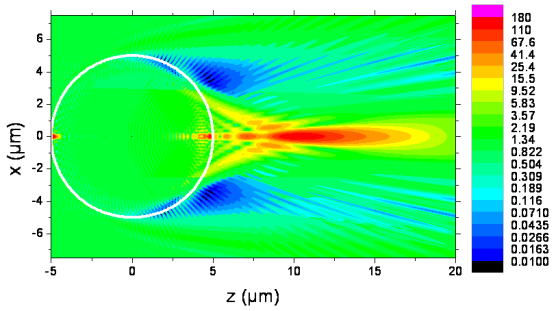

Figure 3.2: Intensity colored map of a 10 μm diameter polystyrene (n_s = 1.6) particle immersed in water (n_b = 1.33) illuminated by a plane wave at λ_0 = 633 nm.

The ability of microspheres to focus light and enhance the local electromagnetic field was first utilized to remove particles from a substrate in laser dry cleaning technique [33, 34] and arrays of particles-lenses were proposed in 2003 as a means to pattern a substrate with neither mask nor lithographic processes [35] offering various patterns when illuminating the array at different angles [36].

Nevertheless, the focusing properties of microparticles have attracted a renewed interest since the work of Chen et al. [37–39]. Their FDTD simulations showed that when cylinders [37] or spheres [38] are illuminated by plane waves, narrow beams are produced in the near field of the shadow-side surface. These beams typically have FWHM (Full Width at Half Maximum) smaller than the incident wavelength over distances of several wavelengths and have been named "photonic jets". Moreover, the intensity can be hundreds of times higher than the incident intensity [38]. Fig. 3.2 shows the electric field intensity (Hermitian square of the electric field) in the vicinity of a 10 μm diameter sphere illuminated by an optical plane wave. The existence of photonic jets has since been experimentally confirmed in the microwave range of frequencies [40], and directly observed in the optical spectrum with a confocal microscope operating in detection mode [4].

The advent of nanosciences and biotechnology have contributed to consider microparticles as useful tools for high resolution nano-particles detection [37–39], fluorescence microscopy improvements [41, 42], Raman scattering enhancement [43], datastorage [44] and nanopatterning [35, 36, 45]. A deeper understanding of this beam is nevertheless needed to fully exploit the potential performance of microspheres as optical components.

An analytical study of light focusing by axially symmetric systems has been performed using wave propagation theory in systems having spherical aberrations, extending the geometrical

optics approach [46]. The field is developed on high-order Bessoid integrals which are vectorial three-dimensional generalizations of the Pearsey Integral. Applied to microspheres, this formalism describes "photonic jets" as resulting from off-axis rays converging towards different points with different angles as a consequence of spherical aberrations. In this framework, photonic jets are approximated as Bessel beams of variable cross section. This description provides physical insights, tending towards Mie theory for size parameters above 30.

For smaller spheres, the agreement is less accurate in part due to evanescent field contributions that are not taken into account in the geometric optics framework. A spectral analysis of the photonic jets has previously been carried out by Itagi et al. [47] for cylinders. They concluded that the evanescent field only makes small contributions to photonic jets properties which are mainly due to a particular phase distribution. Chen et al. also affirmed that photonic jets do not involve evanescent fields [37], but this still need to be closely examined for spherical problems invoking a complete three-dimensional analysis.

In this manuscript, a thourough study of photonic jet beams is performed and we investigate in particular the conditions suitable for its production. A comparison with focused beams is made for didactic purposes to point out the performance of microparticles as microlenses. A three dimensional analytical plane wave expansion of the field will then be undertaken to quantify contributions of the different spatial frequencies in photonic jets field distributions (section 3.3) including evanescent field contributions. This study will readily lead us to compare photonic jets with Bessel beams.

3.2 Optical properties of photonic jets in direct space

The clear focusing properties of microspheres encourages further investigations. In particular, the conditions for the generation of photonic jets remains ill-defined and the focal properties of the resulting beam depends on several parameters such as the size and the dielectric material of the microsphere as well as the illuminating wavelength and the surrounding background. A question has also arisen concerning the benefits to employ such beams for biological applications. Experimental studies have shown that a solution containing microspheres can enhance two-photon fluorescence by 35 percent via the local electric field enhancement due to photonic jets [41]. However, as far as we know, no single-photon fluorescence enhancement has been reported.

In the current state of the art, fluorescent spectroscopy is performed using tightly focused beams produced by high numerical aperture microscopes. The question arises whether photonic jets can outperform such far-field focused beams. For didactic purposes, a comparison of the dimensions of photonic jets with focused beams will be performed (section 3.2.1).

3.2.1 Photonic jets in aqueous medium direct space

We consider typical conditions occuring in biophotonic experimentations. In general, biological molecules at interest freely evolve in aqueous media of refractive index close to $n_b = 1.33$. The intensity pattern produced by a polystyrene-like microsphere ($n_s = 1.6$) of diameter 2 μm illuminated by a plane wave is simulated in Fig. 3.3. The incident plane wave propagates at a wavelength λ_0

= 633 nm in vacuum, along the z-axis for increasing z values (i.e. from the left to the right) and is polarized along the x-axis. Fig. 3.3(a) displays the electric field intensity distribution in the $x0z$ plane and Fig. 3.3(b) in the $y0z$ plane.

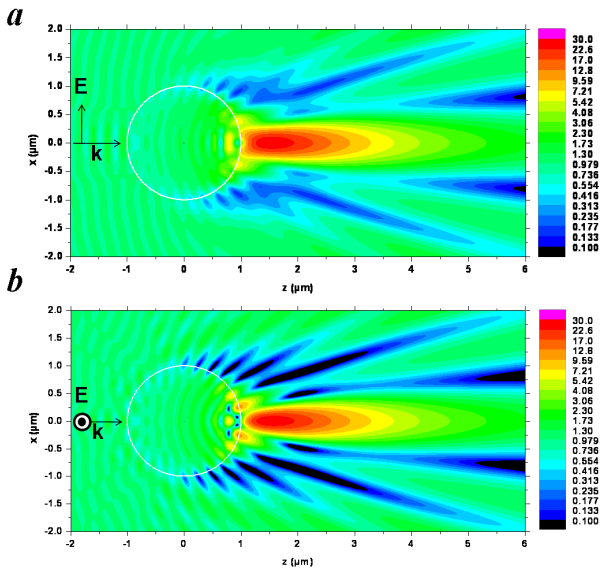

Figure 3.3: Intensity colored map of a photonic jet (a) in the $x0z$ plane and (b) in the $y0z$ plane. The polystyrene microsphere (n_s = 1.6), 2 μm in diameter is illuminated by a plane wave at λ_0 = 633 nm. The electric field of the incident plane wave is polarized along the x-axis. Calculations are performed with N = 30.

These colored maps clearly highlight the typical features of a photonic jet: an intense field is generated outside the sphere and exhibits a longitudinal extent exceeding several micrometers while its transverse dimensions remain on the order of the incident wavelength along the propagation. One can notice that Fig. 3.3(a) and Fig. 3.3(b) are slightly different. The linear incident polarization induces an anisotropy in the intensity distribution, so that the transverse dimension of the photonic jet is slightly larger along the polarization direction than in the orthogonal plane. It can also be interesting to notice that the intensity distribution exhibits interferences effects giving rise to local maxima and minima. These secondary maxima are angularly regularly distributed and highlight the diffractive and multipolar nature of photonic jets.

To proceed further in the characterization of photonic jets, the intensity sections of the photonic jet produced in the same conditions as in Fig. 3.3 (λ_0 = 633, n_s = 1.6, n_b = 1.33) are displayed in Fig. 3.4 along the three Cartesian axis: (a) along the propagation axis z, (b) along the polarization axis x and (c) along the orthogonal axis y. The transverse sections displayed in Fig. 3.4(b) and Fig. 3.4(c) are calculated at the local maximum of Fig. 3.4(a), i.e. at $z = z_{\text{Imax}} = 1.52\,\mu$m.

The intensity distribution along the z axis, displayed in Fig. 3.4(a), highlights two different behaviors. Inside the microsphere (the position of the sphere surface is illustrated by the vertical green line), the intensity pattern shows oscillations with a local maximum close to the sphere surface. These oscillations are due to internal reflection giving rise to complex interferences pattern (see Fig. 3.3). In the surrounding medium ($z \geq 1\ \mu$m), the field distribution exhibits a smooth

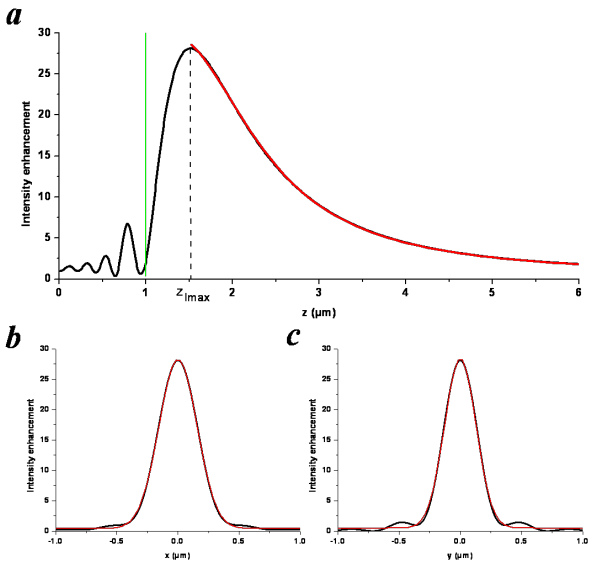

Figure 3.4: (a) Cross-sections of the intensity enhancement along the z-axis for a photonic jet produced in the same conditions as in Fig. 3.3 ($\lambda_0 = 633$, $n_s = 1.6$, $n_b = 1.33$). The green line represents the edge of the sphere surface located at $z = 1$ μm. The red line fits a Lorentzian distribution. (b) Intensity cross-section along the transverse axis x at $z = z_{\text{Imax}} = 1.52$ μm and (c) cross-section along the transverse axis y at $z = z_{\text{Imax}} = 1.52$ μm. In (b) and (c) the red lines follow a Gaussian type distribution.

distribution with a local maximum occuring 500 nm beyond the sphere surface that reveals the focusing of light in a photonic jet. It must be stressed that contrary to Gaussian beams, the intensity distribution of photonic jets along the z-axis is not symmetric with respect to the maximum intensity and we have found that the intensity enhancement can be fitted in its decreasing part by a Lorentzian distribution (red line in Fig. 3.4(a)). Furthermore, the intensity enhancement along the transverse axis can be fitted as Gaussian distributions (red lines in Fig. 3.4(b) and Fig. 3.4(c)). These remarks can be of practical interest since well-known Gaussian beams follow similar field distributions. Therefore, by defining the diffraction length of the photonic jet, z_r, as the half width at the half maximum (HWHM) of the Lorentzian fit, and the width at the diffraction focus, w_0, as the half width at the I_{max}/e^2 of the Gaussian fit, a comparison with well-known focused beams can be performed.

Table 3.1: Comparison of lengths and widths of the photonic jet with an equivalent Gaussian beam.

beam type	Gaussian beam s = 0.32	Photonic jet beam
length z_r	0.45 μm	1.00 μm
width w_{0x}	320 nm	310 nm
width w_{0y}	260 nm	260 nm

As an example a quantitative comparison is performed in Table 3.1. We consider a focused Gaussian-like beam simulated using Davis formulas with an angular opening parameter s = 0.32

(c.f. chapter 2), and a photonic jet with similar waists $w_{0x} = 320$ nm and $w_{0y} = 260$ nm. As a result, for an equivalent waist, this photonic jet exhibits a twice longer length than its Gaussian beam counterpart. One could conclude that photonic jets have a greater length than classical Gaussian beams. However this statement is only valid when photonic jets have a maximal intensity far away from the surface. It must be reminded that the intensity distribution of photonic jets along the z-axis is not symmetric with respect to the maximum intensity and this conclusion is not exactly valid. For instance, when the field is located on the surface or very close to it, the length of the focal volume can become quite small since a part of the energy is located inside the particle. It thus becomes essential to establish different ranges of size parameters and dielectric contrasts to clearly define the suitable conditions for producing photonic jets.

3.2.2 Features of photonic in direct space

Photonic jets are produced by a scattering response of a dielectric microsphere illuminated by optical plane waves. On contrary to Whispering Gallery modes which are resonant response occuring at precise frequencies (c.f. chapter 2), photonic jets are non resonant responses occuring over a large range of illumination frequencies. Nevertheless, the focal properties of the resulting beam depends on several parameters such as the size and the dielectric material of the microsphere as well as the illumination wavelength and the surrounding background. More precisely, Mie coefficients show that the scattered field depends on the size parameters $k_bR = 2\pi n_b/\lambda_0$ and k_sR as well as the refractive index contrast $\rho = n_s/n_b$.

In order to provide an idea of the photonic jets properties in a compact form, we focus our attention on two situations where the dielectric contrast between the particle and the surrounding medium is low index contrast $\rho = n_s/n_b = 1.6/1.33 = 1.2$ and for higher index contrast $\rho = n_s/n_b = 1.6/1 = 1.6$. The incident wavelength is chosen in the red range of color at $\lambda_0 = 633$ nm.

The position and the amplitude of the maximum intensity enhancement along the z-axis are respectively displayed in Fig. 3.5(a)(c) and Fig. 3.5(b)(d) as a function of the particle radius. The calculations are performed for a polystyrene sphere embedded in a medium of refractive index $n_b = 1.33$ (refractive index contrast $\rho = 1.2$) in Fig. 3.5(a), (b) and in vacuum in Fig. 3.5(c), (d) (refractive index contrast $\rho = 1.6$).

The focal position (identified with the maximum intensity) is displayed in Fig. 3.5(a)(c) and exhibits a smooth linear dependence with respect to the microsphere radius. The green line corresponds to the $y = x$ function indicating the position of the edge of the microsphere surface. This linear behavior is at first surprising but is consistent with the linear dependence of the focal position in the geometrical optics for thick lenses [31]:

$$f_{\text{geo}} = \frac{\rho R}{2(\rho - 1)} \tag{3.1}$$

However, the proportions of the linear coefficient are slightly different. A linear fit (red line in Fig. 3.5) shows that for low index contrast situations ($\rho = 1.2$ in Fig. 3.5(a)), the focal position increases as $z_{\text{Imax}} = 2.15R$ while in the case of $\rho = 1.6$, it varies as $z_{\text{Imax}} = 1.2R$. When employing Eq. (3.1) to calculate the focal position, it gives that for $\rho = 1.2$ and $\rho = 1.6$, we respectively obtain $f_{\text{geo}} = 3R$ and $f_{\text{geo}} = 1.33R$ (dashed lines in Fig. 3.5). It results that the focal position for a 1 μm

sphere illuminated at $\lambda_0 = 633$ nm occurs at the surface of the sphere as soon as $n_s/n_b > 1.6$ while in the geometrical framework it occurs for a refractive index $n_s = 2$.

From Fig 3.5(a)(c), we can conclude that the generation of photonic jets having a maximum intensity far from the surface requires low index contrasts: $\rho < 1.6$. If the contrast is larger but less than 2, the size of the microsphere has to be sufficient to detach the focal position from the microparticle.

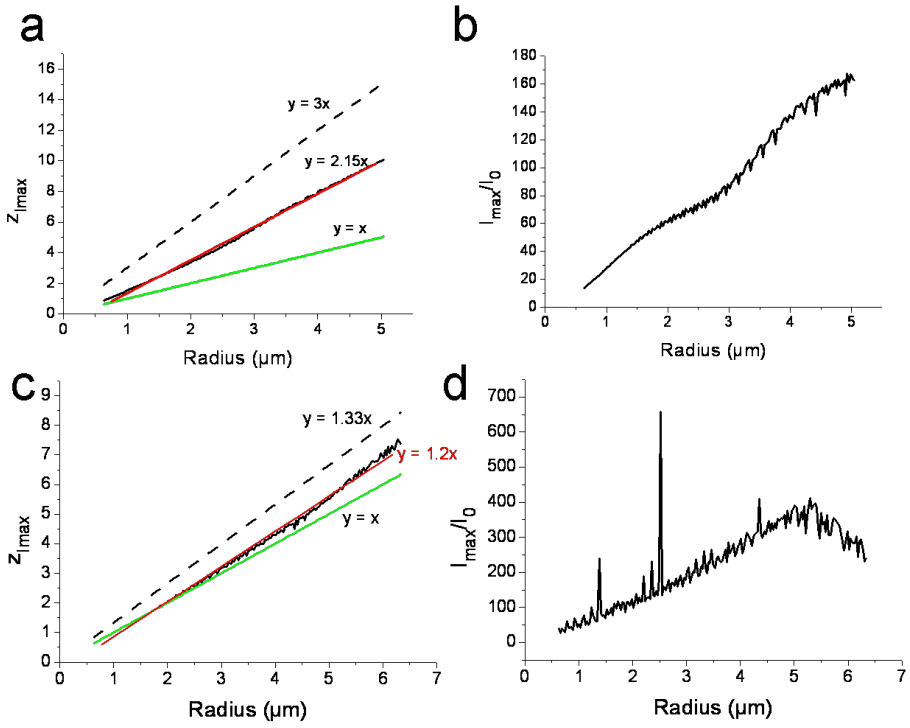

Figure 3.5: (a), (c) Calculated z_{Imax} position of photonic jets (full black lines) and its linear fit (red line) as a function of the raius of the microsphe. Ths geometric focal position f_{geo} (dashed lines) and the position of the surface (green line $y = x$) are also displayed. (b), (d) Amplitude $I_{\max}$ of the maximum intensity enhancement. (a) and (b) The 2 μm polystyrene sphere ($n_s = 1.6$) is immersed in water $n_b = 1.33$, (c) and (d) the polystyrene sphere is embedded in vacuum $n_b = 1$.

The amplitude enhancement (normalized by the incident intensity I_0) at the focal position of photonic jets displayed Fig. 3.5(b)(d) highlights fundamentally different features according to the refractive index contrast ρ. While plots in Fig. 3.5(b) show for low index contrasts a smooth increasing distribution of $I_{\max}$ with moderate amplitudes, numerous peaks appear in the plots for higher contrasts in Fig. 3.5(d) of amplitude enhancement. This behavior are due to the excitation of Whispering Gallery Modes.

For the sake of completeness, Fig. 3.6(a) and (c) display the waists (half width at $I_{\max}/e^2$) and Fig. 3.6(a) and (c) the lengths z_r (Half Width at Half Maximum) for respectively $\rho = 1.2$ and $\rho = 1.6$ for increasing radii of the particle R. These plots exhibit increasing curves with rapid oscillations. These oscillations are limited in amplitude and a qualitative study can still be undertaken. From Fig. 3.6(a) and (c), one can notice that the waist of the photonic jet is comprised between 0.25 μm

$< w_0 < 0.45$ μm for the two contrasts. The waists of photonic jets depend slightly on the contrast ratio but above all on the size of the nanoparticle (or the incident wavelength)and remains shorter than the incident wavelength reaching $\lambda_b/2$ for a 1 μm polystyrene particle immersed in vacuum. It must be stressed that these results are obtained with a simple microsphere straightforwardly illuminated by a plane wave, thus highlighting the extremely good focusing properties of this simple optical component.

More interestingly, the length z_r of the photonic jet depends strongly on the contrast ratio. For $\rho = 1.6$ the length can be extremely short (around 200 nm for $R = 1$ μm) but is increased up to 1 μm for $R > 6$ μm. In contrast, for $\rho = 1.2$ the length of the photonic jet is greater than 1 μm reaching 3 μm for radii $R > 5$ μm.

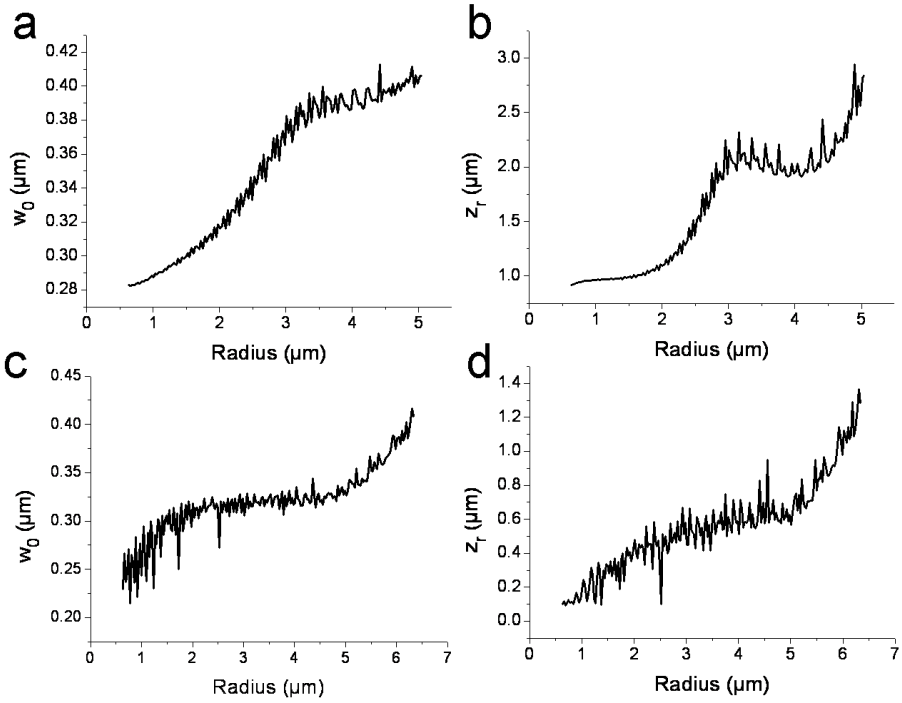

Figure 3.6: (a), (c) Width z_0 and (b), (d) length z_r of the focal volume exiting the microsphere. (a) and (b) The 2 μm polystyrene sphere ($n_s = 1.6$) is immersed in water $n_b = 1.33$, (c) and (d) the polystyrene sphere is embedded in vacuum $n_b = 1$.

This study has highlighted how the generation conditions of photonic jets can influence their properties such as their focal position, their intensity enhancements as well as the waists and the lengths of their focal volumes. Plane wave illumination of a microsphere can result in quite narrow and short focal volumes for high index contrasts and one can question whether the denomination photonic jets is still relevant in such situations. We thus consider that photonic jets as it is commonly defined, are beams of elongated focal volumes extending far from the microsphere. It results that the conditions for the generation of photonic jets in the optical range lies in a trade-off between the index contrast ratio and the size of the particle.

3.3 Optical properties of photonic jets in reciprocal space

Photonic jets are beams which are focused in the near field of the microlens where scattering may generate evanescent fields. In a general manner, the scattering process redistributes light over all the directions of the complex space. Real components of the wave vectors correspond to light propagating in a given angular direction while the complex components remain in the vicinity of the particle. To estimate the contribution of both propagative and evanescent fields in the photonic jet morphology, a rigorous angular spectral analysis of the scattered field was undertaken. The analytical development, which consists in expanding the partial waves on plane waves, has been fully detailed in Appendix B. A summarize of this study is presented in this chapter in order to reveal the physical insight introduced by this approach.

3.3.1 Plane waves expansion in the multipole framework

The layout of the angular expansion is displayed in Fig. 3.7. We are interested in the investigation of the evanescent field contributions of the scattered electric field along the propagation direction z. Indeed, evanescent waves (i.e. k_z is purely imaginary) are associated with high radial components K defined from the k-vector as $k_z = \sqrt{\mathbf{k}_b{}^2 - \mathbf{K}^2}$. Large amplitudes of K produce high spatial frequency contributions responsible for rapid variations of the field in the plane $x0y$.

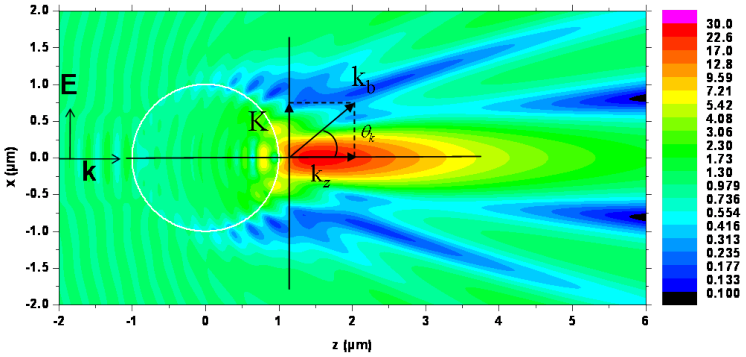

Figure 3.7: Layout of the spectral expansion superposed with the intensity colored map of the photonic jet investigated in Fig. 3.3, ($N = 30$).

The multipole development of the scattered field can be expressed as:

$$\overrightarrow{\mathbf{E}}_{scat}(r,\theta,\phi) = E_0 \sum_{n=1}^{\infty} \sum_{m=-n}^{n} f_{n,m}^{(h)} \overrightarrow{\mathbf{M}}_{n,m}(k_b r,\theta,\phi) + f_{n,m}^{(e)} \overrightarrow{\mathbf{N}}_{n,m}(k_b r,\theta,\phi) \tag{3.2}$$

We express the transverse vector $\mathbf{K}$ as

$$\mathbf{K} = \mathbf{k}_{//} = K\cos(\phi_k)\widehat{\mathbf{x}} + K\sin(\phi_k)\widehat{\mathbf{y}} \tag{3.3}$$

The multipolar waves functions can be expanded on the plane waves functions in terms of the Vector Spherical Harmonics (VSHs):

$$\mathbf{M}_{nm}(r_{//},\phi,z) = \frac{i^{-n}}{2\pi k_b}\int_{K=0}^{\infty}\int_{\phi_k=0}^{2\pi} KdKd\phi_k\ \mathbf{X}_{nm}\left(\widehat{\mathbf{k}}\right)\frac{\exp\left(i(\mathbf{K}\cdot\mathbf{r}_{//}+k_z|z|)\right)}{k_z} \tag{3.4}$$

$$\mathbf{N}_{nm}(r_{//},\phi,z) = \frac{i^{-n+1}}{2\pi k_b}\int_{K=0}^{\infty}\int_{\phi_k=0}^{2\pi} KdKd\phi_k\ \mathbf{Z}_{nm}\left(\widehat{\mathbf{k}}\right)\frac{\exp\left(i(\mathbf{K}\cdot\mathbf{r}_{//}+k_z|z|)\right)}{k_z} \tag{3.5}$$

where $(r_{//},\theta,\phi)$ are the cylindrical coordinates. One can observe that the VSHs can be considered as the angular spectrum of the multipolar waves. Full calculations are relegated to Appendix B and lead to a spectral expansion of the field in terms of cylindrical Bessel functions of the radial coordinate.

$$\overrightarrow{\mathbf{E}}_{scat}(r_{//},\phi,z) = E_0\int_0^{\infty}\frac{K}{k_b}d\frac{K}{k_b}\begin{bmatrix} A(\frac{K}{k_b},\phi,z)J_0(Kr_{//})\frac{\{\widehat{\mathbf{x}}+i\widehat{\mathbf{y}}\}}{\sqrt{2}} \\ B(\frac{K}{k_b},\phi,z)J_1(Kr_{//})\widehat{\mathbf{z}} \\ C(\frac{K}{k_b},\phi,z)J_2(Kr_{//})\frac{\{\widehat{\mathbf{x}}-i\widehat{\mathbf{y}}\}}{\sqrt{2}} \end{bmatrix} \tag{3.6}$$

with

$$A(\frac{K}{k_b},\phi,z) = \sum_{n=0}^{\infty} f_{n,m}^{(h)}A_n^{(h)} + f_{n,m}^{(e)}A_n^{(e)} \tag{3.7}$$

$$B(\frac{K}{k_b},\phi,z) = \sum_{n=0}^{\infty} f_{n,m}^{(h)}B_n^{(h)} + f_{n,m}^{(e)}B_n^{(e)} \tag{3.8}$$

$$C(\frac{K}{k_b},\phi,z) = \sum_{n=0}^{\infty} f_{n,m}^{(h)}C_n^{(h)} + f_{n,m}^{(e)}C_n^{(e)} \tag{3.9}$$

$$\tag{3.10}$$

The full expression of the weighting functions $A_n^{(h,e)}$, $B_n^{(h,e)}$, $C_n^{(h,e)}$ are relegated to Appendix B.

3.3.2 Results and discussions

The amplitude and phase of the weighting functions A, B and C at $\phi = 0$ and $z = 1.005$ μm have been plotted respectively in Fig. 3.8(a), (b) and (c) as a function of the radial wave vector K/k_0 for a photonic jet produced in water by a 2 μm diameter polystyrene microsphere illuminated by a plane wave of $\lambda_0 = 633$ nm. As we have assumed a circularly polarized electric field, one observes that the A coefficient corresponding to no polarization mixing is predominant weighting a 0^{th} order Bessel function J_0.

This is particularly clear in the low spatial frequency range $K/k_0 < 0.5$ where the polarization mixing amplitudes of B, and C never exceed 10. All 3 coefficients exhibit an oscillating behavior with respect to K/k_0. We henceforth focus our attention on the predominant coefficient A.

The radial spectrum |A| has the following features: a generally decreasing and oscillating feature in the region $0 \leq K/k_b \leq 1$ corresponding to propagative fields, a singularity originating from the pole of the homogeneous background medium Green function at $K/k_b = 1$ and a monotonically decreasing behavior when $K \geq k_b$ for evanescent field contributions.

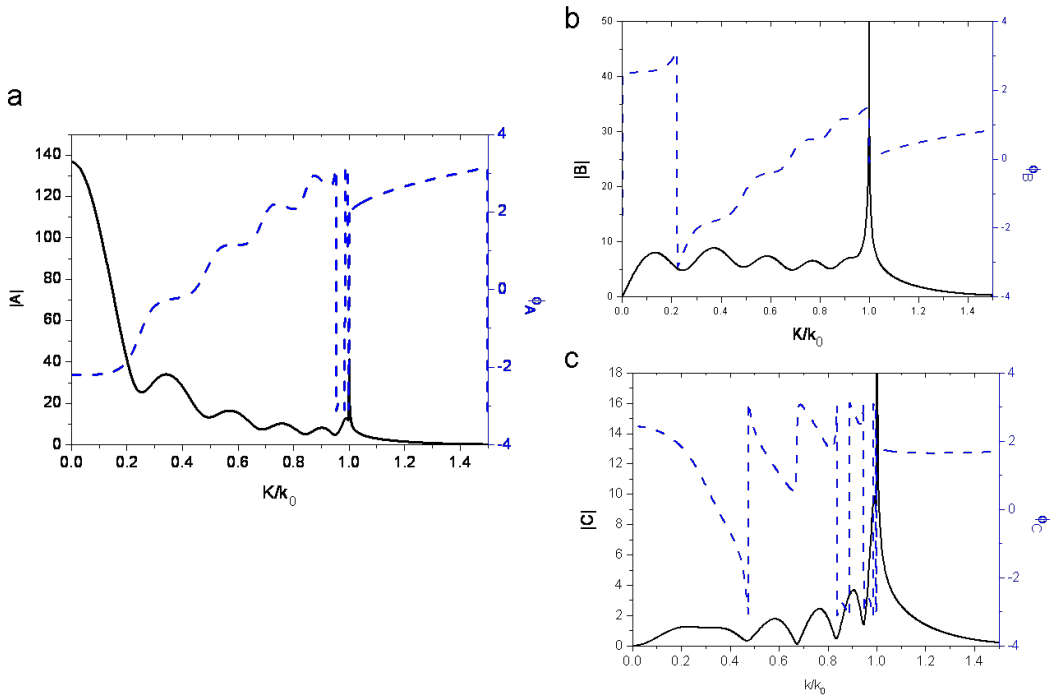

Figure 3.8: Spectral coefficients A, B and C (see Eq. (B.20)) at $\phi = 0$ and $z = 1.005$ μm of a photonic jet produced in water by a 2 μm diameter polystyrene microsphere illuminated by a plane wave at $\lambda_0 = 633$ nm. Amplitude (full line, left axis) and phase (dashed line, right axis) of (a) A, (b) B and (c) C.

From the zero-frequency to the first minimum, the spectral distribution can be fitted by a narrow Gaussian-type distribution. The secondary maxima and minima observed in the higher spatial propagative frequencies enrich the jet spectrum and result in photonic jets having features that differ from Gaussian beams in direct space.

3.3.3 Field reconstruction

To understand the role of contributions originating from spatial frequency components, we carried out a numerical experiment consisting in removing some spectral contributions. Fig. 3.9(a) shows the intensity colored map fully reconstructed by integrating over all the contributions K/k_b from 0 to ∞. This map is simulated in the same conditions as Fig. 3.3 and validates the spectral reconstruction technique. Due to restrictions in the expansion, the field has been calculated for the half-space of interest for $z > 1$ μm only and the white circles represent the edge of the microsphere. Fig. 3.9(b) displays the field distribution when removing the high spatial frequencies $K/k_b \geq 1$ corresponding to the evanescent field contributions. As we expected from Ref. [2, 47], the evanescent field only slightly contributes to the field distribution. The contributions of low and high propagating spatial frequencies are more striking. Fig. 3.9(c) shows the intensity colored map obtained when the low spatial frequencies ($K/k_b \leq 0.25$) have been removed. The associated intensity map shows a clear reduction of the longitudinal extent of the photonic jet. This simple numerical experiment

indicates that low transverse spatial frequencies strongly contribute to the elongated focal volume of photonic jets. One can remark however that the field intensity reaches similar amplitudes as in Fig. 3.7 demonstrating that the energy is mainly contained in the higher spatial frequencies.

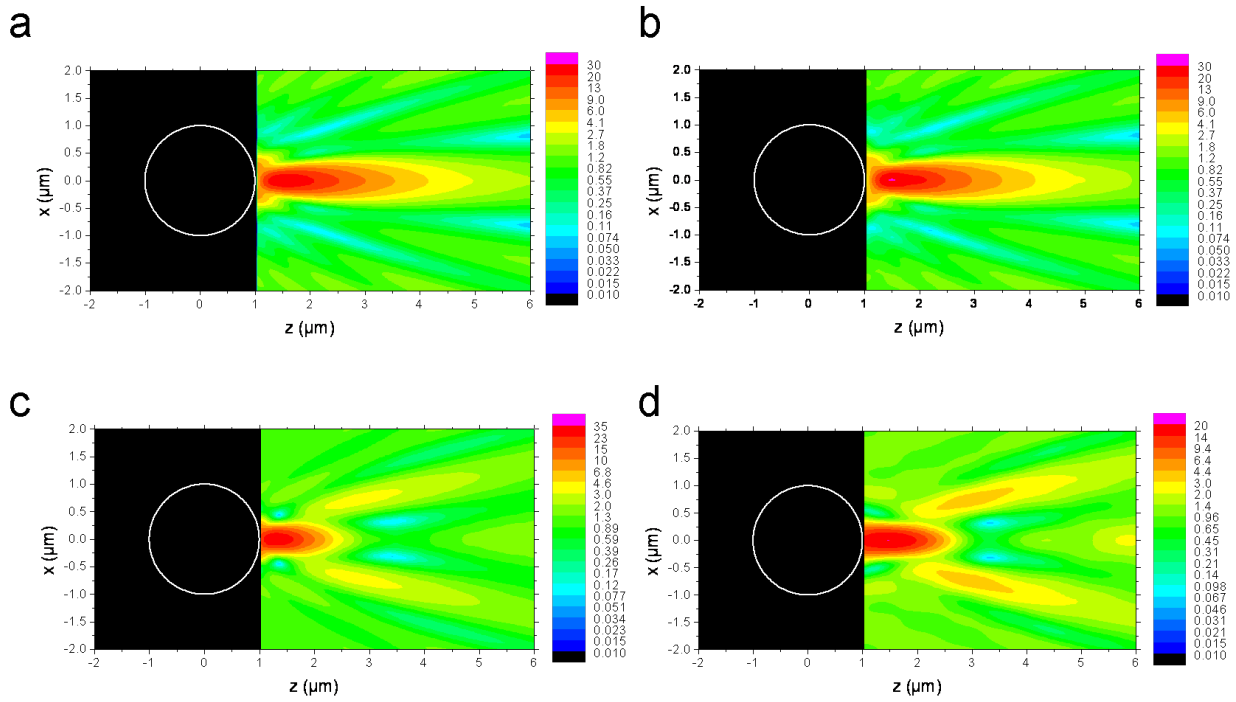

Figure 3.9: Reconstruction of the field intensity of a photonic jet in the same conditions as in Fig. 3.7 after filtering of the spectral components. (a) The entire spectrum is taken into account, (b) only the propagating modes $K/k_b \leq 1$ are kept, (c) the low spatial frequencies ($K/k_b \leq 0.25$) have been removed. (d) Both low ($K/k_b \leq 0.25$) and high spatial ($K/k_b \geq 0.75$) frequencies have been removed.

Fig. 3.9(d) shows the same intensity map as Fig. 3.9(c) but when both low transverse ($K/k_b \leq 0.25$) and high spatial transverse ($K/k_b \geq 0.75$) frequencies have been removed. The morphology of the beam remains similar to the previous case. One can notice the relative enhancement of secondary intense areas off-axis. The amplitude of the focal intensity has dropped significantly indicating that high transverse angular frequencies importantly contribute to the field intensity. Furthermore, the absence of high spatial frequencies slightly widens the transversal dimension while lengthening the longitudinal extent of the beam.

3.4 Axisymmetric system and Bessel beams

A theoretical cylindrical scalar wave solution of Maxwell equations was introduced by Durnin [48] in 1987 characterized by a single 0^{th} order Bessel function of the radial dependence for a beam propagating along the z-axis.

$$E(r_{//}, \phi, z) = e^{ik_z z} J_0(K r_{//}) \tag{3.11}$$

One can readily show using the definition of cylindrical Bessel functions that Eq. (3.11) is indeed a solution of the radial Helmholtz equation. One can easily verify that the radial distribution of the Bessel beam does not depend on the propagation distance z. Such beams theoretically propagate over an infinite distance without distortion and have attracted significant interest since their transverse sections possess a sharp central peak. In contrast to plane waves, which can also be considered as non-diffractive waves of infinite spatial extent, Bessel beams exhibit a maximum on the z-axis with several secondary maxima in the transverse direction. The effective width of the central peak can be extremely narrow (approximately $3\lambda/4$) over large distances which renders these beams excellent candidates for sensing small objects and accurate positioning of optical components [49] .

Nevertheless, it is important to notice that J_0 Bessel functions decrease as a $1/\sqrt{\rho}$ function [50] which implies infinite energy content (like plane waves). In other words, non-diffractive beams are of infinite extent and possess infinite energy. Consequently, Bessel beams, similarly to plane waves remain theoretical constructs in applications of the necessarily finite sized pupil apertures of real optical systems. Nevertheless, it remains possible to approximate such ideal beams. The first implementation of Bessel beams, was carried out by Durnin himself [51] with a simple annular pupil located in the focal plane of a convergent lens. According to Durning's predictions based on a scalar diffraction theory of electromagnetic waves, if such a beam is generated from a pupil aperture of several centimeters, it should propagate over several meters without significant distortion of its radial intensity distribution. A reduction of the aperture to several millimeters would nevertheless produce a beam with a longitudinal extent of several micrometers.

Bessel-like beams have since been produced employing hemispheric and cylindrical lenses [49]. It has also been demonstrated that geometrical aberrations, and spherical aberrations in particular, can induce Bessel-like beams [49]. The special properties of Bessel beams can be readily understood from a plane wave expansion. This procedure has been implicitely done in the spectral expansion in section 3.3 and will lead to further understanding of photonic jets.

3.4.1 Geometrical spherical aberrations and axicon

Axisymmetric systems have been investigated for their ability to concentrate light along a focal line. So called axicons were at first studied to spread an image point along a focal line and conical lenses were introduced as an efficient way to achieve this property. The geometrical ray tracing for a conical lens has been performed using the commercial software *ZEMAX* and displayed in Fig. 3.10(a). This plot nicely highlights how each ray crossing the surface at a given height is focused at different positions along the propagation axis. The superposition of these cones results in an intense field around the optical z-axis leading to a high longitudinal extent.

In the electromagnetic framework, an expansion on plane waves is convenient. The development of the Bessel beams in terms of plane waves can be obtained using an integral expression of Bessel functions [52]:

$$\int_0^{2\pi} \exp(ix\cos(\phi_k - \phi))\exp(in\phi_k)d\phi_k = 2\pi i^n J_n(x)\exp(in\phi) \tag{3.12}$$

where n is an integer. Taking $n = 0$, Eq. (3.12) enables the J_0 function to be written:

$$\int_0^{2\pi} \exp(ix\cos(\phi_k))d\phi_k = 2\pi J_0(x) \tag{3.13}$$

Inserting $x = Kr_{//} = k_b \sin\theta_k r_{//}$ into Eq. (3.13), one sees that J_0 beams are a superposition of plane waves all propagating at an angle θ_k defined as $K/k_b = \sin\theta_k$ (the angle θ_k is illustrated above in Fig. 3.7) but with azimuthal angles ϕ_k varying from 0 to 2π. Thus, it is easy to understand that axicons are efficient tools for producing Bessel beams.

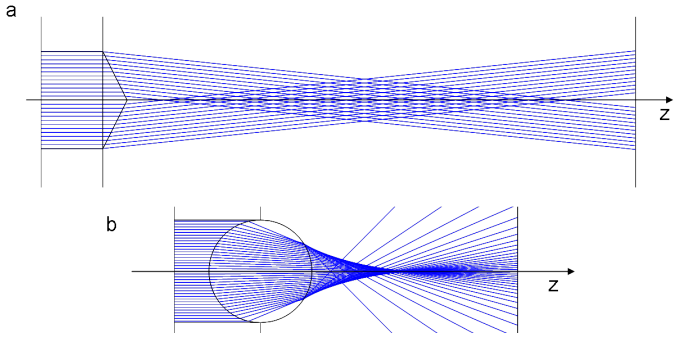

Figure 3.10: Geometrical ray tracing of a collimated light beam illuminating (a) a conical lens, (b) a spherical lens.

Fig. 3.10(b) shows a ray tracing of the spherical lens illuminated by a collimated beam. Although the focusing properties and consequently the intensity pattern are not as trivial as the conical lens, one can easily notice that the field is not focused in a single focal point but rather distributed along the propagation axis. This is a classical feature of light focusing by spherical lenses which involves spherical aberrations [31]. In the geometrical optics framework, an intense focal line is generated with a narrow transverse dimension. One should recall at this step that we have seen that J_0 functions are the principal components of photonic jets field and certain properties of Bessel beams may have applications to photonic jets.

3.4.2 Discussion

The expansion performed in the previous section has highlighted interesting similarities between Bessel beams and photonic jets provided by a common Bessel dependence of the radial parameter. These similarities may lead to a better physical understanding of photonic jets properties and can provide tools to shape the beam.

For instance, the non diffracting behavior of Bessel beams is said to lie in the non-paraxial contributions. It results that pure Bessel beams, due to the definition given in Eq. (3.12) should not be greatly disturbed by an object located on the optical axis. This self-reconstructing behavior can be easily understood from the ideal case since Bessel beams are created by non-null angular plane waves which contain energy passing aside the obstacle. In particular this property has been investigated to simultaneously trap and manipulate several microparticles with a single light beam [53]. To verify the role of the non-paraxial contributions, we simulate a photonic jet with a microsphere

containing an absorbing material preventing the "paraxial" contributions from crossing the microsphere. The electric field intensity map of a classical photonic jet and a photonic jet generated by a coated sphere containing an absorbing kernel are displayed in Fig. 3.11(a) and Fig. 3.11(b) respectively.

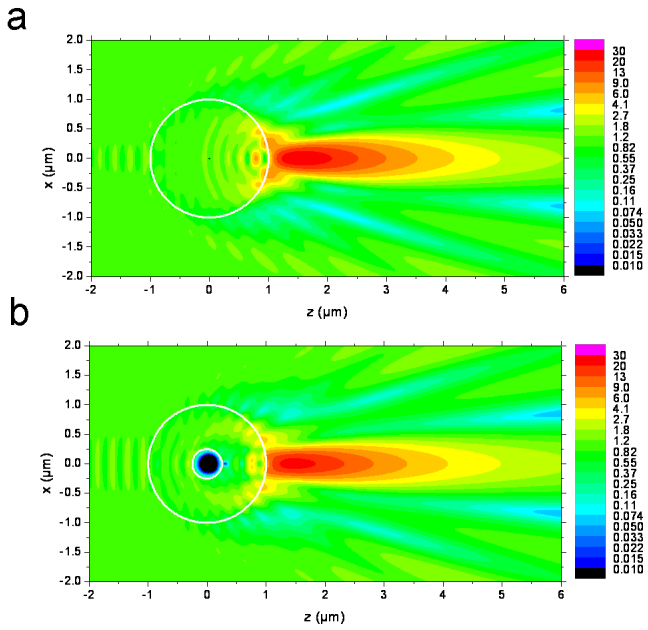

Figure 3.11: (a) Intensity colored map of a photonic jet in the same conditions as in Fig 3.7. (b) Same as (a) with an absorbing bulk of diameter 500 nm in the center of the 2 μm polystyrene sphere.

A straightforward comparison of Fig. 3.11(a) and Fig. 3.11(b) shows that the photonic jet is almost not disturbed by the presence of the absorbing kernel. The filtering of the paraxial rays leads to a focal volume closer to the surface, but preserves the elongated nature of the beam. More generally, it has been recently demonstrated by Kong et al. [54] that graded index microspheres can increase the longitudinal extent of photonic jets. This property can be readily understood from the previous study. A layered microsphere permits to address both paraxial and nonparaxial contributions with a specific optical path allowing non paraxial "rays" to be focused far from the sphere surface and increase the longitudinal extent of the beam.

The Bessel-like nature of photonic jets has been highlighted in this study. The axisymmetric focusing system combined with geometric spherical aberrations leads to a Bessel type beam producing an elongated focal volume exiting the sphere. The role of non paraxial contributions has been demonstrated to allow a better understanding of photonic jets properties and possible strategies for tailoring such beams.

3.5 Conclusion

It has been demonstrated in this chapter that a simple dielectric microsphere can efficiently focus an incident optical plane wave. The beam produced is highly confined in the transverse direction but may have a rather large longitudinal extent. An explanation was found in the rich angular spectrum of the beam invoking 0^{th} order Bessel functions and oscillating high spatial frequencies. Although photonic jets are highly interesting for laser dry cleaning, nanopatterning or data storage, the large longitudinal extent is generally undesirable for imaging or spectroscopy technics that require three dimensional confinement in water-based solutions. Nevertheless, one should recall that photonic jets result from a plane wave illumination, only consisting of a null transverse spatial frequency. One can wonder then what would happen if, instead of a plane wave illumination, the microsphere was illuminated by a focused beam. This possibility will be addressed in the next chapter.

CHAPTER 4

3D confinement of light with near-field operating microlens

Contents

4.1 Introduction

High numerical aperture microscopes are currently employed to concentrate light in volumes as small as possible. However, diffraction limits the dimension of the focal area to a volume on the order of the incident wavelength. It has been demonstrated in the previous chapter that photonic jets (illumination by a plane wave) can strongly 'focus' light despite the presence of diffraction effects. However, it has also been emphasized that photonic jets are non optimal for imaging techniques due to their large longitudinal dimensions. Thus, when illuminated by optical plane waves, dielectric microspheres do not beat the spatial resolution of high numerical aperture microscopes. However, instead of comparing these two optical systems, one may ask the question whether the combination of the high numerical aperture beams with microspheres could produce interesting focusing effects. Indeed, focused beams contain high transverse components which may contribute to reduce the dimension of the focal volume exiting the microsphere. The combination first interested the scientific community for the optical forces involved in such focused beams enabling the trapping and manipulation of dielectric beads with light. Optical tweezers have been then widely investigated, and McLeod et al. [46] have recently reported the dynamic nanopatterning of surfaces using optically

focused beams. The focused beam plays the role of both optical tweezers and focusing tool for patterning the surface.

Furthermore, we have recently demonstrated in collaboration with the MOSAIC team of the Fresnel Institute that microspheres illuminated by tightly focused beams can outperform fluorescence spectroscopy measurements obtained with the state of art classical microscope objectives [5–7]. These studies indicate interesting field distributions in the vicinity of the microsphere that require further investigations. In this chapter, we investigate the case of a microsphere illuminated by a highly focused beam. It will be demonstrated that the microsphere can confine light in a focal volume on the order of $(\lambda_0/n_b)^3$. We will consequently employ compound dielectric microsphere in order to focus light in volumes on the order of the wavelength.

4.2 Three-dimensional confinement of light: direct space investigation

4.2.1 Gaussian beam illumination

The microsphere is now illuminated by a highly focused Gaussian beam. During this study, the Davis formulation (c.f. chapter 2) has been employed to generate the multipolar expansion of a focused beam produced by a high N.A. microscope objective. Fig. 4.1(a) displays the intensity distribution of the incident focused beam. Several theoretical studies have investigated the accurate modeling of tightly focused beams in the multipole framework [22, 23]. Nevertheless, the Davis formulation [18] remains a simple approximation that enables fast and simple modeling of focused beams. Although the Davis formulation is said to be a poor approximation for experimental tightly focused beams, the good correlations between the experimental measurements and the numerical simulations will support this choice (c.f. section 4.5).

The focused beam is thus employed to illuminate the 2 μm polystyrene microsphere of refractive index $n_s = 1.6$ embedded in a water-based solution. Fig. 4.1(b) displays the subsequent intensity pattern where the incident beam is focused 560 nm beyond the sphere surface. It illustrates an intense field which is confined at the exit surface of the microsphere. A straightforward comparison with Fig. 4.1(a) indicates that the microsphere has clearly reduced the dimensions of the incident focal volume with respect to that of the free high N.A. beam.

This observation is even more apparent in Fig. 4.2 which plots the intensity sections of the incident (blue lines) and the resulting (red lines) beam along the Cartesian (a) propagation axis z and (b) transverse axis. The transverse section is plotted at $z = 1.56$ μm for the incident beam and $z = 1$ μm for the resulting beam. The incident field is further confined by the sphere both longitudinally and transversally. The longitudinal modification of the beam is more spectacular since the maximum intensity has been both enhanced and displaced towards the sphere surface. This is quite surprising since it was observed in the chapter 3 that under the same conditions, a plane wave illumination produces a quite elongated narrow beam. The incident focused beam has enabled a spectacular reduction of the longitudinal extent that requires further explaination.

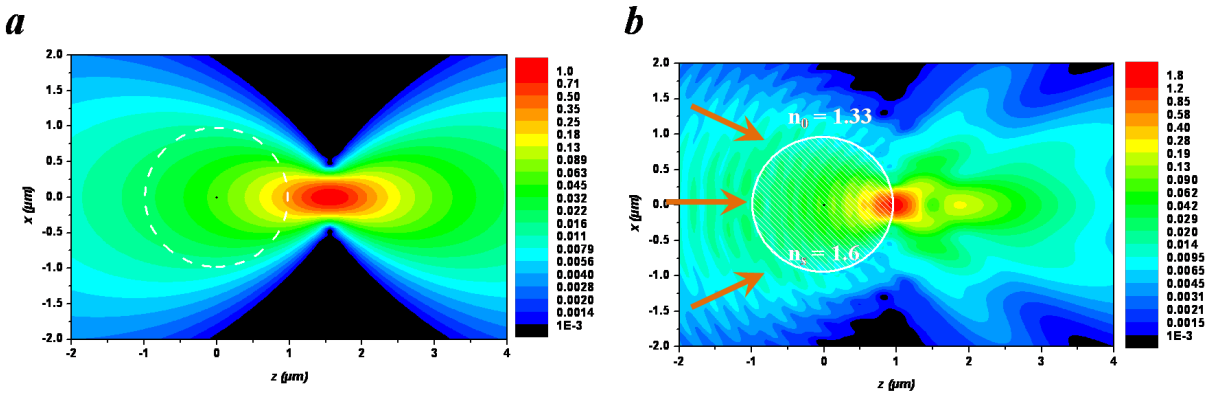

Figure 4.1: Intensity pattern produced by a polystyrene sphere ($n_s = 1.6$), 2 μm in diameter illuminated by a circularly polarized Gaussian beam of numerical aperture N.A. ≈ 1.2 at $\lambda_0 = 633$ nm. The Gaussian beam is focused 560 nm beyond the surface of the sphere.

4.2.2 Discussion

A rapid investigation of the effective volume has been undertaken quantifying its reduction. Table 4.1 compares the transverse and longitudinal waists defined at I_{max}/e^2, denoted respectively w_{xy} and w_z for the incident beam and the beam focused by the microsphere for $d = 1.56$ μm. Let us remark that with the addition of the microsphere, the longitudinal intensity distribution is no longer symmetric with respect to the I_{max} position and that the longitudinal waist is calculated outside the sphere, after the I_{max} position. The effective volume behind the sphere defined by $\pi^{3/2} w_{xy}^2 w_z/2$ (only the exiting volume is taken into account), is reduced by an order of magnitude, and is approximately $0.6\ (\lambda_0/n_b)^3$. It can be reduced down to $0.43\ (\lambda_0/n_b)^3$ for a melamine microsphere (refractive index of 1.68). Let us insist however that the ratio between the refractive index of the microsphere n_s and the surrounding medium n_b has to be lower than 1.4 because for higher contrasts ($n_s \geq 1.85$ in aqueous solution), the electromagnetic field is fully confined inside the dielectric sphere.

One can first wonder whether this phenomenon is due simply to straightforward focusing effects or if interference processes are responsible for the longitudinal reduction. One can readily observe that the intensity distribution observed in Fig.4.2(b) suggests interference effects since at the incident focal point ($z = 1.56$ μm), the total field exhibits a strongly reduced intensity with $I/I_0 \approx 0.075$.

4.2.3 Interferences and numerical aperture

In order to understand the physical mechanism of this confinement, we have employed a simulation method that allows the separation of the incident and the scattered field contributions from the total field. Fig. 4.3 presents the map of (a) the incident, (b) scattered and (c) total field intensity. The scattered field pattern plotted in Fig. 4.3(b) shows an elongated region with high intensity in the shadow side of the sphere. This scattered field is close to a classical "photonic nanojet" beam: it has both narrow lateral and large longitudinal extent. Only the coherent sum of the incident beam plus the scattered field is able to reach a strong confinement in all three directions (Fig. 4.3(c))

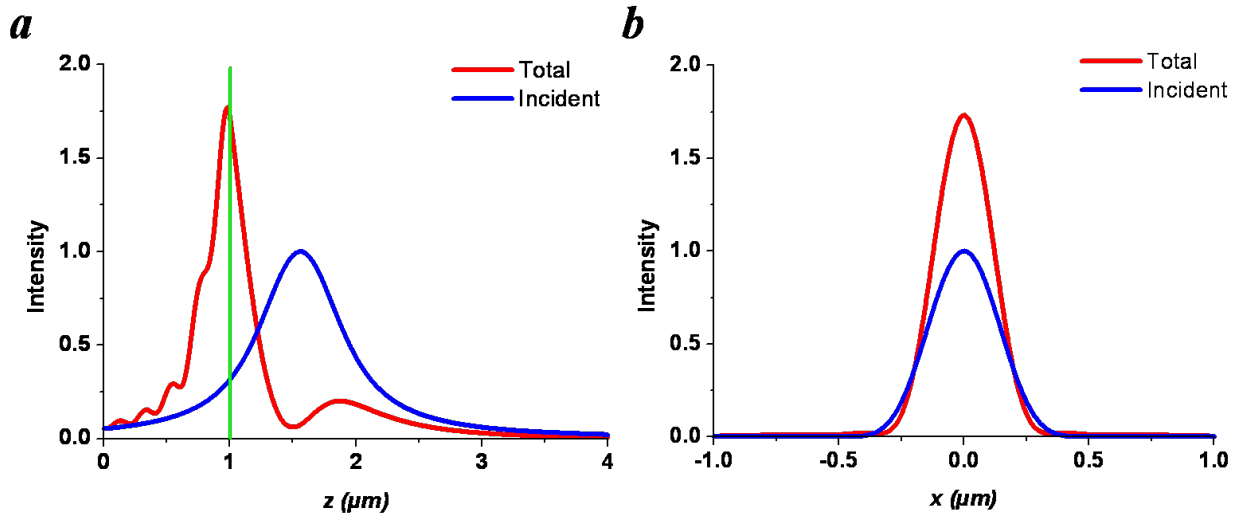

Figure 4.2: The polystyrene ($n_s = 1.6$) 2 μm in diameter illuminated by a Gaussian beam of numerical aperture N.A. $\approx$ 1.2 at $\lambda_0 = 633$ nm. The Gaussian beam is focused 560 nm beyond the surface of the sphere (N = 30). Intensity distribution (a) along the propagation axis z and (b) along the transverse axis x of the incident beam (blue lines) and the confined field (red lines) in the presence of the microsphere. The transverse section is plotted at $z = 1.56$ μm for the incident beam and $z = 1$ μm for the resulting beam.

which highlights the relation between interferences and the reduction of the effective volume.

The effective volume defined as $V_{\text{eff}} = \pi^{3/2} w_{xy}^2 w_z/2$ is displayed in Fig. 4.4 as a function of the numerical aperture. Let us note that, for each numerical aperture value, the distance d between the center of the sphere and the focus of the incident beam was tuned to optimize the maximum of intensity, I_{max}, behind the sphere. The effective volume decreases as a function of the numerical aperture and a numerical aperture above N.A. $\approx$ 0.8 is needed to obtain an effective volume below $(\lambda_0/n_b)^3$. We conclude that the three-dimensional confinement directly depends on the high angular contributions present in the incident highly focused Gaussian beam, and that a confinement below $(\lambda_0/n_b)^3$ can be achieved with a numerical aperture higher than 0.8. Let us emphasized that this confinement does not bit the diffraction limit since half of the energy is actually focused inside the particle and not taken into account in the effective volume.

A second numerical experiment is carried out by tuning the distance d between the center of the sphere and the waist of the incident beam for a numerical aperture equal to 1. Fig. 4.5 displays the electric field intensity map for decreasing distances (a) $d = 7$ μm, (b) $d = 4$ μm, (c) $d = 3$ μm, (d) $d = 1.6$ μm (e) $d = 1$ μm (f) $d = 0$ μm. A motion capture is available in Ref. [7]. For large separation distances, the incident beam is slightly affected by the presence of the sphere. When the distance is decreased, interferences between the incident beam and the beam emerging from the microsphere become more visible. One can notice that the apparent beams emerging from the microsphere in Fig. 4.5(b) and Fig. 4.5(c) are similar to the scattered beam observed in Fig. 4.3(b). At shorter distances as in Fig. 4.5(d), one can observe a dark spot due to destructive interferences between incident and scattered fields, which creates the longitudinal confinement. The near field

Table 4.1: Summary of the characteristic widths at I_{max}/e^2 corresponding to the intensity maps displayed in Fig. 4.1. The effective volume is defined for the incident beam as $V = \pi^{3/2} w_{xy}^2 w_z$, and for the focused beam by the microsphere $V = \pi^{3/2} w_{xy}^2 w_z/2$ (recalling that only the beam exiting the microsphere is considered here).

Beam type	Incident Gaussian beam	Beam + microsphere	Ratio to incident beam
Longitudinal waist w_z	1.250 μm	420 nm	33%
Transverse waist w_{xy}	300	230 nm	77%
Effective volume V	$0.6\,\mu m^3 \approx 6(\lambda_0/n_b)^3$	$0.06\,\mu m^3 \approx 0.6(\lambda_0/n_b)^3$	10%

behind the sphere is then highly enhanced. When the sphere is further approached to the focal area, there is essentially no incident field passing aside the sphere. Only one spot, arising from the focusing of the incident field by the sphere is then observed, but the maximum of intensity is located inside the particle and presents little interest for microscopy applications. This study shows that high angular incident components passing aside the sphere are needed to obtain a strong three-dimensional subwavelength confinement. It must be emphasized that the three dimensional confinement investigated here can be extended to other types of focused beams and in particular, we showed that it could be extended to incident photonic jet beams [8].

4.3 Focusing light with compound microlenses

In low index contrast medium, the longitudinal dimension of photonic jets can be considered as a disadvantage because it does not provide a better confinement of light than a classical microscope objective with high numerical aperture. A simple manner to modify the features of the beam that emerges from the microsphere is to change the illuminating beam. A numerical experiment has been undertaken to illuminate the microsphere with a highly focused Gaussian type beam and has evidenced that the microsphere can confine the field at its surface in an intense volume smaller than $0.6(\lambda_0/n_b)^3$. This phenomenon is due to the interplay of two contributions: the well-known focusing of the incident field by the microsphere provides the transverse confinement of the field. The longitudinal reduction is due to interferences between the scattered field and the high angular components of the excitation beam. In this section, we study a full micrometric microscope objective made of compound dielectric microlenses in order to confine a plane wave in a three dimensional intense region of dimension on the order of the wavelength. We assume that the longitudinal confinement observed with a Gaussian beam illumination can be achieved with a photonic jet as incident beam. Owing to the study performed in the chapter 3, which has demonstrated that photonic jets have high angular components, we propose to illuminate a second microsphere with a photonic jet. The aim is to reduce its longitudinal extent and make photonic jets suitable for applications requiring high transverse and longitudinal resolutions.

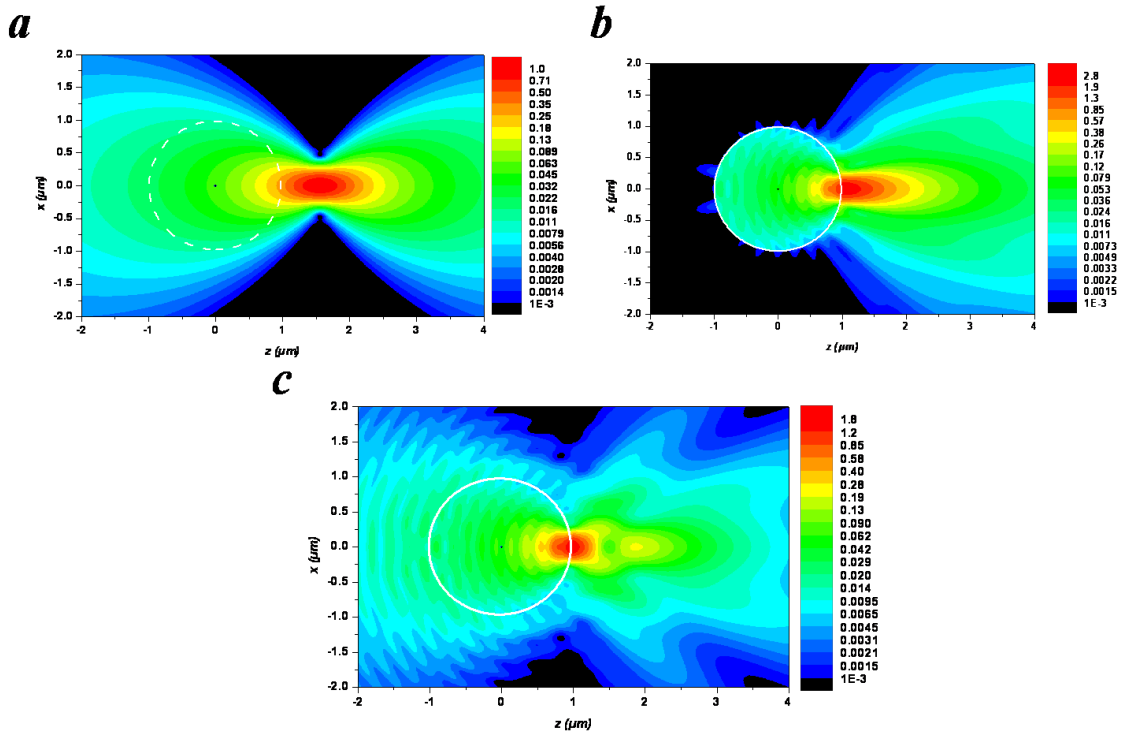

Figure 4.3: Intensity pattern of (a) the incident, (b) scattered and (c) total field.

4.3.1 Reduction of the longitudinal extent of photonic jets

We consider now a 6 μm-diameter polystyrene ($n_s = 1.6$) sphere illuminated by a plane wave at $\lambda_0 = 633$ nm. Fig. 4.6(a) presents the electric field intensity maps of the photonic jet propagating in a water-based solution illustrating, as discussed in the chapter 3, the main features of a typical photonic jets: a narrow lateral extent and a large longitudinal dimension. Fig. 4.6(b) shows the electric field intensity pattern when a 2 μm-diameter polystyrene sphere is added in the photonic jet beam. The two spheres are touching and have the same optical axis. To simplify the study, the

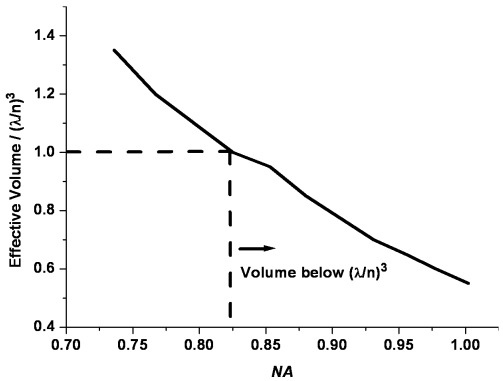

Figure 4.4: Effective volume $V_{\text{eff}} = \pi^{3/2} w_{xy}^2 w_z/2$ of the confined field as a function of the numerical aperture of the incident focused beam.

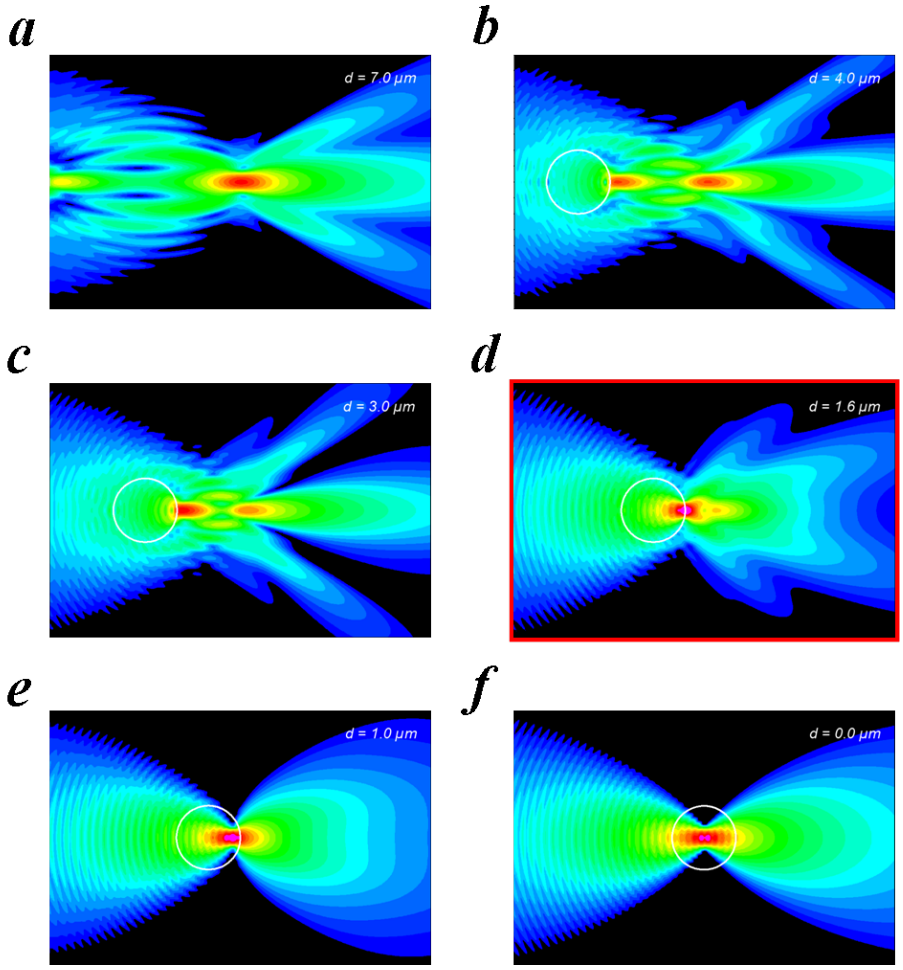

Figure 4.5: Electric field intensity map in logarithmic scale for d decreasing from $d = 7\ \mu$m to $d = 0\ \mu$m and $N.A. \approx 1$. The optimal confinement is obtained in (d) when $d \approx 1.6\mu$m

incident plane wave is circularly polarized to preserve the cylindrical symmetry. One can see from Fig. 4.6(b) that a single and bright spot of small dimensions in the three spatial directions is present at the surface of the smaller sphere. The photonic jet is further confined by the second sphere both longitudinally and transversally.

Table 4.2 compares the transverse and longitudinal waists (radii) of the two beams, defined at I_{max}/e^2 and denoted respectively w_{xy} and w_z. The longitudinal intensity distribution is not symmetric with respect to the I_{max} position and we define two longitudinal waists for the incident photonic jet beam, w_{z-} and w_{z+}, which are respectively the waists before and after the I_{max} position. The effective volume is then defined as $\pi^{3/2} w_{xy}^2 (w_{z-} + w_{z+})/2$. The effective volume behind the second sphere defined by $\pi^{3/2} w_{xy}^2 w_z/2$ is reduced by more than one order of magnitude, and is approximately $(\lambda_0/n_b)^3$. Let us remark that the longitudinal waist is calculated outside the sphere. It is apparent that the longitudinal modification of the beam is more spectacular since the maximum intensity has been both enhanced and moved toward the sphere surface. It must be stressed that this strong confinement of light is achieved with a simple non resonant dielectric structure.

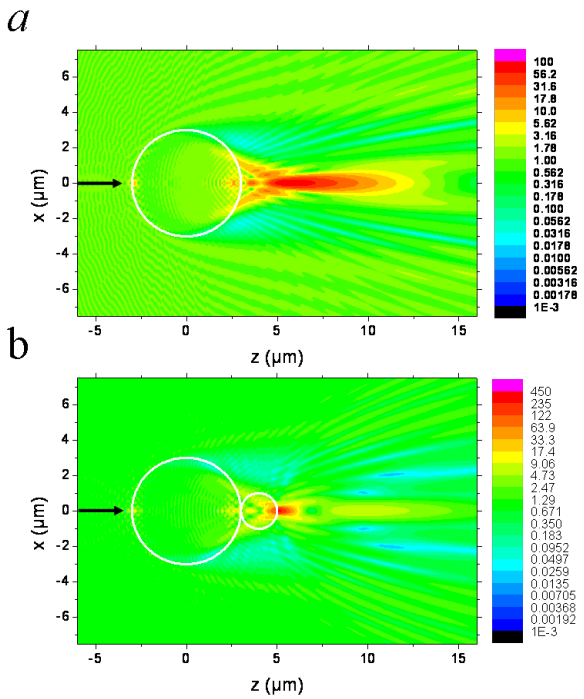

Figure 4.6: Total electric field intensity map in logarithmic scale of (a) a 6 μm-diameter polystyrene sphere illuminated by a plane wave at $\lambda_0 = 633$ nm and (b) a 2 μm-diameter polystyrene ($n_s = 1.6$) sphere is added in the photonic jet beam. The white circles represent the microsphere sections.

We employ the implemented generalized Mie theory to calculate the incident and scattered field separately. Fig. 4.7 presents the map of the intensity of the field scattered by the second sphere. It shows an elongated region with high intensity in the shadow side of the sphere. This scattered field is very close to a classical "photonic nanojet" beam. The coherent sum of the field scattered by the bigger sphere plus the scattered field by the second one is able to reach the strong confinement in the three directions (Fig. 4.6(b)).

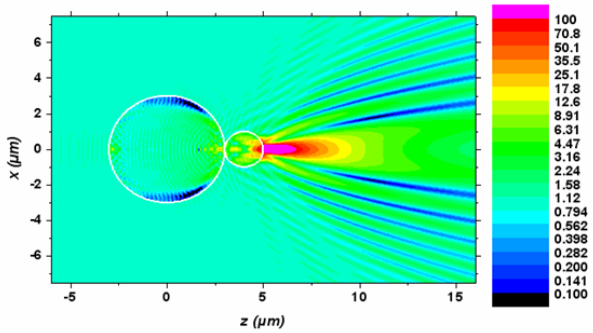

Figure 4.7: Intensity pattern of the scattered field for the compound microsphere in the same conditions as Fig. 4.6(b).

It can be convenient to pay attention to situations where the second microsphere has a slightly

Table 4.2: Summary of the characteristic widths at I_{max}/e^2 corresponding to the intensity maps displayed in Fig. 4.6. The volume is derived for the incident photonic jet as $\pi^{3/2}w_{xy}^2(w_{z-} + w_{z+})/2$, and for the field focused by the microsphere as $\pi^{3/2}w_{xy}^2 w_z/2$ (let us recall that only the beam exiting the microsphere is considered here).

Beam type	photonic jet	photonic jet + second microsphere
Longitudinal waist w_z	4.6 μm	795 nm
Transverse waist w_{xy}	370 nm	225 nm
Maximum intensity enhancement	87.5	420
Effective volume V	2.3 $\mu m^3 \approx 21(\lambda_0/n_b)^3$	0.11 $\mu m^3 \approx 1.05(\lambda_0/n_b)^3$

different size. The intensity map of two extreme configurations is displayed in Fig. 4.8 for a sphere of diameter (a) 1 μm and (b) 3 μm. When the sphere is too small (Fig. 4.8(a)), most of the energy is passing aside the sphere so that the photonic jet is almost not modified (see also Fig. 3.11 in section 3.4). When the sphere exceeds a critical size as illustrated in Fig. 4.8(b), the whole beam penetrates the second sphere and the maximum intensity occurs inside the sphere which is of minor interest. In addition, an intense field still exist at the exit surface of the sphere but it is no more confined. The distribution pattern shows a transversal confinement of the field but no destructive interferences that could have enabled the longitudinal reduction. The effective volume is ten times larger than in the optimal case.

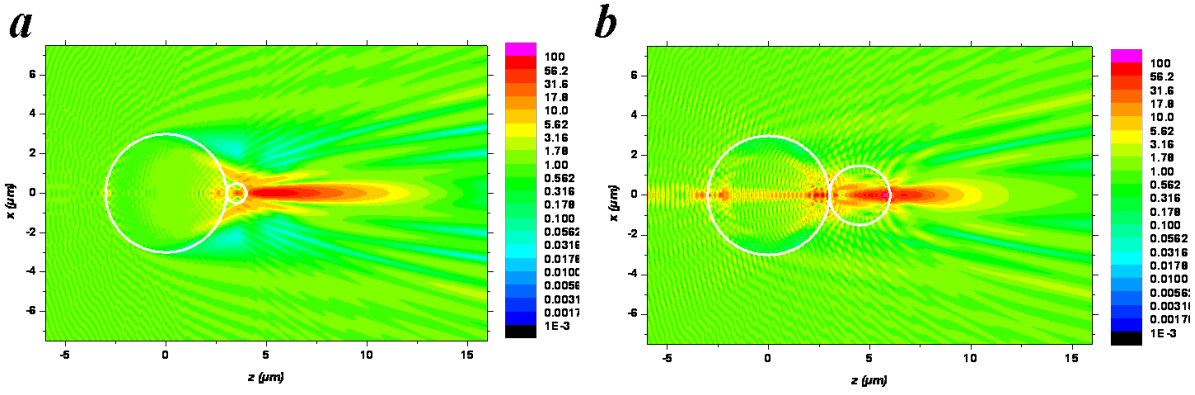

Figure 4.8: Electric field intensity map. (a) The second sphere $R_2 = 0.5$ μm and (b) $R_2 = 2$ μm. The incident photonic jet is generated by a polystyrene microsphere 3 μm in diameter.

It could be stressed that the fabrication of this compound set of two dielectric microspheres is not trivial and should require technically challenging processes. However, this numerical study permits to better understand the longitudinal confinement of light observed when the microsphere

is illuminated by a highly focused beam. Moreover, it highlights that microscope objectives of micrometric sizes can be designed in principle. For instance, the respective index contrasts of the two microlenses could be tailored to compensate chromatic aberrations analogously to the classical achromatic doublets.

It must be recalled that self-similar chains of metallic particles were proposed by Stockman *et al.* [55] to focus light in small volumes via the excitation of coupled localized plasmon resonances. These systems consisting of several metallic nanoparticles of different sizes has been engineered so that the biggest particle enables large electromagnetic cross-sections whereas a couple of smaller particles ensure highly localized fields. The investigated compound microlenses follow similar considerations. The biggest microsphere enables a large electromagnetic cross-section ensuring the collection of a large amount of energy. The addition of the small particle provides the three dimensional confinement. However, the non resonant nature of the phenomenon employed in our compound microlenses provide a broad frequency bandwith without any intrinsec loss.

The potential reduction of the longitudinal dimension of photonic nanojets in water-based solutions has been demonstrated based on the ability of microspheres to confine a focused beam along the three spatial directions. We evidenced that optical plane waves can be confined in a volume of order $(\lambda_0/n_b)^3$ by a compound set of dielectric microspheres. This could be particularly helpful in applications where high resolution is required with low index contrasts. The role of non-zero angular components has also been highlighted and the confined field has resulted in a trade-off between incident energy passing the particle and the components passing aside.

4.4 Reciprocal space investigation

Similarly to the study undertaken in the chapter 3, the investigation of the reciprocal space will hold to understand the physical mechanisms involved in the three dimensional confinement. In particular, the role of the high angular components composing the incident focused beam will be emphasized. The expansion of the scattered field has been summarized in chapter 3.3 and fully detailed in appendix B. The analytical plane waves expansion of the regular multipolar waves and irregular waves expansion are obtained in an analogous manner and enables an investigation of interference processes in terms of angular frequency contributions.

4.4.1 Spectral expansion

The layout of the field projection undertaken is superposed on the intensity pattern in Fig. 4.9(a). The resulting polarized spectral component |A| of the incident (blue line), scattered(green line) and total field (red line) are displayed in Fig. 4.9(b). All the plots are normalized by the amplitude at $K/k_b = 0$. As it can be expected, the incident spectrum is essentially a Gaussian distribution. The distribution is monotonously decreasing so that the main spectral contributions lie in the low spatial frequencies.

The spectral components of the total field (red line) show a quite different distribution. A straightforward comparison with the incident spectrum highlights a reduction of the lower spatial frequencies. A maximum appears in the spectral distribution at $K/k_b = 0.3$ revealing a weaker

influence of the low spatial frequency components. This relative reduction can be also observed in the scattered spectrum distribution (green line) and can be related to the slight decrease of the longitudinal dimensions with respect to the incident Gaussian beam (see Fig 4.3(a) and Fig 4.3(b)). The addition of the microsphere produces a redistribution of the angular spectrum. An interference between the scattered and incident fields has induced a relative increase of high spatial frequencies and a decrease of low spatial frequencies.

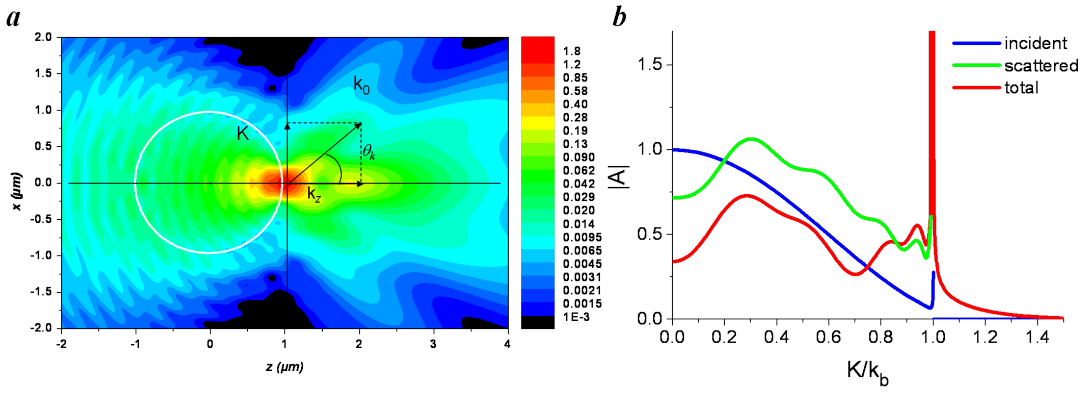

Figure 4.9: (a) Layout of the field projection undertaken. (b) Amplitude of the spectral component A as a function of the radial component of the wavevector K/k_b.

The reciprocal spectrum analysis is consistent with the observations made in direct space. The drop of low spatial frequencies is correlated with a higher confinement in the field distribution while a stronger influence of high spatial frequencies in the spectrum reflects the enhancement of the local intensity.

4.4.2 Discussion

As we assume that the field observed in Fig. 4.9(a) results from a trade-off between the energy focused by the particle and the incident energy passing aside, the angular spectrum in the optimal case can be difficult to analyse. It can be convenient to pay attention to not-optimized situations where different proccesses can be evidenced separately. Fig. 4.10(a) shows the total field map and Fig. 4.10(b) the associated spectra (incident, scattered and total) for the same incident beam as Fig. 4.9 but with a focal position for the incident beam of $d = 3$ μm. The intensity map highlights four intense regions in the plane of interest, two of them located along the optical axis z resulting from the microfocusing effect (i.e. scattered field) and from the residual incident beam. The origin of the other intense areas can be understood in term of a constructive interferences process.

Fig. 4.10(b) shows the associated spectrum. The incident Gaussian distribution remains identical to the one displayed in Fig. 4.9(b). Although the scattered spectrum follows a smooth decreasing distribution, highly contrasted minima and maxima appear in the total spectrum. The most striking feature of this spectrum is the cancellation of specific spatial frequencies. Let us recall that in direct space, the spatial frequencies (more precisely the A component), correspond to a superposition of plane waves with the same angular direction θ_k. The zeros occuring at $K/k_b = 0.4$ coincides

with conic fringes of destructive interferences that can be observed in direct space in Fig. 4.10(a). These destructive interferences follow a conical morphology in the three dimensional space, readily explaining the formation of the four intense field areas. This numerical experiment clearly demonstrates that destructive interferences occuring at specific spatial frequencies in the reciprocal space are consistent with destructive interferences pattern drawing a conical shape in direct space as it has been observed in Fig. 4.10(a).

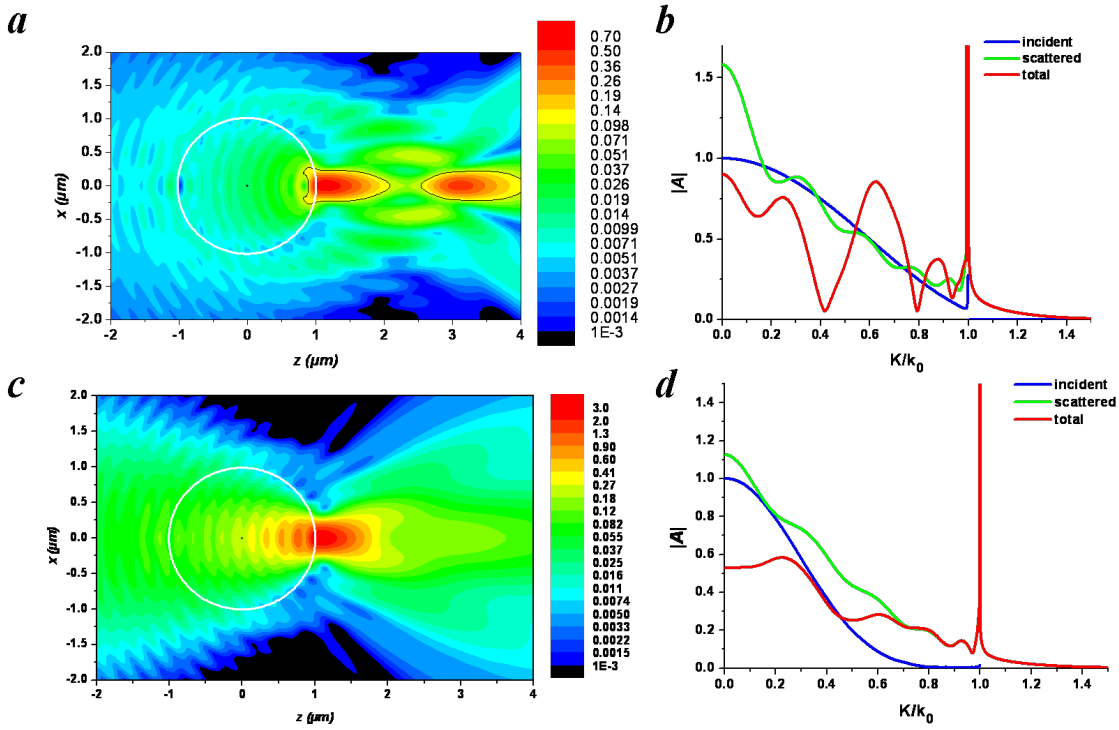

Figure 4.10: (a) Intensity pattern and (b) spectral component |A| as a function of the normalized radial component of the wavevector, K/k_b. The Gaussian beam produced with a N.A. $\approx$ 1.2 is focused 2 μm beyond the sphere surface. (c) Intensity pattern and (d) spectral component |A| as a function of the radial component of the wavevector K/k_b. In that case, the Gaussian beam is produced by a numerical aperture objective of N.A. $\approx$ 0.8.

Our second numerical experiment consists in reducing the numerical aperture of the incident beam from N.A. = 1.2 to N.A. = 0.8. It results in a larger incident focal volume corresponding to a narrower Gaussian distribution in the incident spectrum (blue line in Fig. 4.10(d)). The focusing distance from the particle has been optimized to minimize the intensity volume as illustrated with the colored map in Fig. 4.10(c). In that case, the total angular spectrum follows a smooth distribution. Similarly to Fig. 4.9(b), a more moderate reduction of the low spatial frequencies is observed. The high spatial frequencies of the total field are slightly enhanced but follow the scattered field high frequencies distribution. It can be observed that in Fig. 4.9(a) and Fig. 4.10(a) the high frequencies of the total field overcome the high spatial frequencies of the scattered and incident field.

In both not-optimal cases investigated above, the angular spectrum shows a balancing between

a drop of low spatial frequency contributions combined with an enhancement of the high angular frequencies with respect to the incident spectral distribution.

4.5 Application to Fluorescence Correlation Spectroscopy (FCS)

Signal detection of fluorescent molecules is a crucial issue in biophotonics. For instance, fluorescent markers are widely employed to explore biologic mechanisms occuring at the molecular scale. A close collaboration with the Mosaic team of the Fresnel Institute has enabled us to apply the numerical results of the three dimensional confinement to the enhancement of Fluorescent Correlation Spectroscopy signals. A common strategy in fluorescence microscopy consists in using a high numerical (N.A.) objective microscope to maximize the detected signal. Fig. 4.11 displays a layout of a state of the art confocal microscope setup. The excitation light source at $\lambda_0 = 633$ nm is first focused by the high numerical objective of N.A. = 1.2 illuminating a solution containing Alexa fluorescent molecules. The strong focusing of the incident light produces an enhancement of the excitation intensity that leads to an enhancement of the photon absorption rate per molecule as well as a reduction of the effective illuminating volume reducing by the way the number of molecules illuminated. In a second step, the excited fluorescent molecules can emit photons at $\lambda_0 = 670$ nm ($> \lambda_0 = 633$ nm) that can be efficiently collected by the same high angular aperture microscope objective. The fluorescence signal enhancement, γ_F, of a single-molecule (with respect to a free space dipolar radiation) can be expressed in the following equation [5]:

$$\gamma_F = \kappa\eta \frac{|\mathbf{E}(r_p).\mathbf{n}_p|^2}{|\mathbf{E}_0(r_p).\mathbf{n}_p|^2} \tag{4.1}$$

In this formula, κ is the collection efficiency enhancement. The excitation rate is defined as the ratio $|\mathbf{n}_p.\mathbf{E}(r_p)|^2/|\mathbf{n}_p.\mathbf{E}_0(r_p)|^2$ where $\mathbf{n}_p$ is the dipole direction and $\mathbf{E}(r_p)$ and $\mathbf{E}_0(r_p)$ are the local electric field at the dipole location r_p respectively with and without the microsphere. η is the quantum efficiency of the emission process defined as the ratio between the power radiated in the far field and the total emitted power $\eta = P_{\text{rad}}/P_{\text{tot}}$ when considering a perfect emitter. This parameter can be strongly influenced both by resonant and non radiative couplings in absorbing structures such as metals. As we are now considering only non-absorbing and non resonant structures, this quantity is assumed to stay close to 1. As a consequence, Eq. (4.1) can be reduced to:

$$\gamma_F = \kappa \frac{|\mathbf{E}.\mathbf{n}_p|^2}{|\mathbf{E}_0.\mathbf{n}_p|^2} \tag{4.2}$$

The above definition enables an experimental and theoretical distinction of the elementary process leading to the enhancement of the detected signal and has been successfully employed to quantify contributions to the fluorescence signal enhancement in metallic nanoholes and dielecrtic microsphere (see Fig. 4.11, the interested readers may also refer to Ref. [5, 6, 56] for a detailed description of the procedure). The presence of the microsphere affects the excitation field and the collection efficiency of fluorescent molecules. It must be stressed that in Fluorescent Correlation

Spectroscopy, molecules are diffused in a water-based solution so that a volume density of emitters has to be considered.

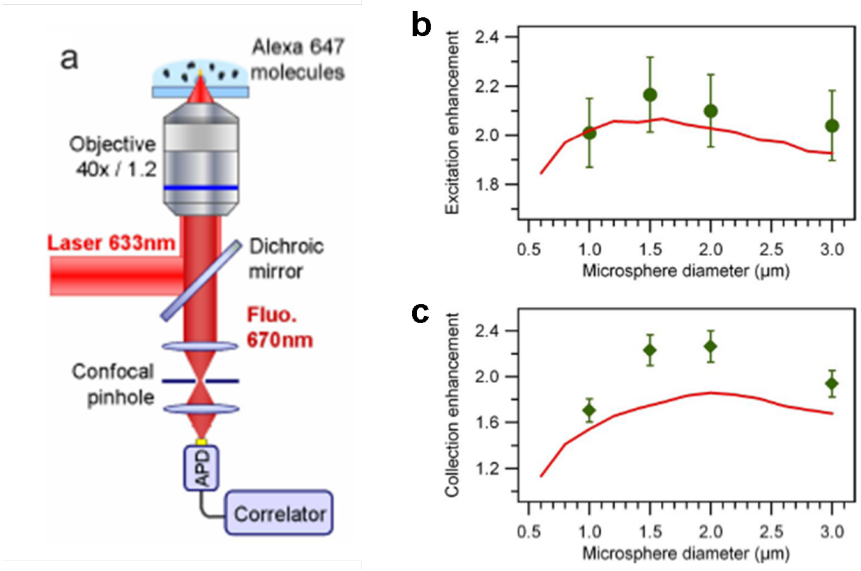

Figure 4.11: (a) Layout of the experimental FCS setup using a high N.A objective. (b) Measured (dots) and simulated (full line) excitation enhancements as a function of the microsphere diameter. (c) Measured (dots) and simulated (full line) collection efficiency enhancements as a function of the microsphere diameter.

To compute the excitation intensity enhancement, we introduce the intensity density ρ_e as the total excitation intensity I_v per unit of effective volume V_{eff} [56], where the excitation intensity is given by:

$$I_V = \int_V |E|^2 dV \tag{4.3}$$

and the effective volume is defined as:

$$V_{\text{eff}} = \frac{\left(\int_V |E|^2 dV\right)^2}{\int_V |E|^4 dV} \tag{4.4}$$

It results that the intensity density can be expressed as

$$\rho_e = \frac{I_V}{V_{\text{eff}}} = \frac{\int_V |E|^4 dV}{\int_V |E|^2 dV} \tag{4.5}$$

The numerical integrations of the field in Eq. (4.5) is made over the region outside the microsphere where the intensity is larger than $I_{max}/10$. Finally, we obtain the excitation intensity enhancement by normalizing the intensity density ρ_e in presence of the microsphere by the intensity density without the microsphere (full red lines in Fig 4.11(b) and (c)).

To numerically compute the gain in collection efficiency due to the microsphere, fluroescent molecules are considered as dipole point-like sources of light set close to the surface of the sphere, at the position corresponding to the maximum intensity found in the excitation field distribution. We compute the average Poynting vector flux over a spherical surface far from the microsphere, centered at the dipole location and a maximum half-angle of 60° corresponding to the numerical aperture of the objective. The collection efficiency is then obtained as the ratio of this Poynting vector flux to the one computed over all directions of space (4π sr). Finally, the collection efficiency enhancement is derived by normalizing the collection efficiency found with the microsphere to the reference efficiency without the sphere. To reproduce the random dipole orientation, we average the collection efficiencies obtained for each orientation x, y, and z of the dipole (dots in Fig 4.11(b) and (c)).

The calculations and the experimental measurements show that both excitation rates and collection efficiencies have been enhanced owing to the presence of the microsphere. The enhancement factor lies around 2 for both contributions, demonstrating that a microsphere acts both for increasing the local field intensity and for collecting radiations emitted by the fluorophores. The numerical simulations are in good agreement with the measured data. Interestingly, the plots indicate a maximum enhancement for sphere diameters of 1 μm. Nevertheless, this maximum is moderate and one can conclude that any diameter from 1 μm to 3 μm would result in significant enhancements of the fluorescence signal.

4.6 Conclusion

This study demonstrated that a three-dimensional volume reduction can be observed when illuminating a microsphere with focused beams. This reduction is due to the interplay of two different contributions: a collimation of the incident field by the microsphere, combined with interferences between the field scattered by the dielectric microsphere and the incident field. It has been shown that a confinement behind the sphere below $(\lambda_0/n_b)^3$ requires a tightly focused beam with a numerical aperture higher than 0.8 together with the appropriate focusing of the incident beam respectively to the sphere. A further increase of the numerical aperture permits a strong confinement of light behind the sphere down to $(\lambda_0/n_b)^3$. Its utility has already been demonstrated in enhancing the fluorescence signal of single-molecules [5, 6] and should prove of considerable interest in Raman spectroscopy, laser nano-patterning and microscopy. It is important to remark that this property was obtained using only dielectric materials and without invoking resonances phenomena. The next chapter will now investigate light confinement achieved with resonant metallic structures.

CHAPTER 5

Plasmon based nanolenses

Contents

5.1 Introduction

In the past few years, metallic nanostructured materials such as interfaces and nanoparticles inclusions have been extensively investigated for the electromagnetic resonances they exhibit when illuminated at optical frequencies. These resonances were first pointed out via anormaleous absorption spectral rays in metallic gratings [57]. Later, metallic surfaces were intensively employed for Surface Enhanced Raman Spectroscopy (SERS) in the visible frequencies in which the roughness of the metal surface induces highly confined fields promoting the non-linear processes required for Raman emission [58]. It has now been widely demonstrated that an illumination in the visible range induces resonant oscillations of the free electron gas of the metal, known as surface plasmon resonances. This leads to strong charge density oscillations at the surface of the metal which may propagate along interfaces and produce highly localized intense fields.

Certain metallic nanoparticles support Localized Surface Plasmon Resonances (LSPRs) at optical frequencies occurring in particles as small as several nanometers, i.e. two orders of magnitude smaller than optical wavelengths. Although the size of the particles is much smaller than the incident wavelength, the excitation of localized plasmons induces enhancements of the particle polarizability that strongly increase both scattering and absorption cross-sections. In addition to the electromagnetic cross-section enhancements, the localized plasmon oscillations generate intense fields in the vicinity of the nanoparticle. The small size of the plasmonic particles compared to optical wavelengths offers the opportunity to downscale classical optical components to the nanometer scale giving rise to the recent field of nano-optics.

LSPRs occurring in chains of nanoparticles have been intensively investigated. Particular attention has been paid to coupled nanoparticles illuminated with an incident electric field polarized along the chain axis. In that configuration, the coupled LSPRs can generate intense fields localized in the interparticle regions of nanometer dimensions [55, 59–64].

In this manuscript, particular attention has been devoted to plasmon modes occurring on spherical nanoparticles for precise reasons:

a) A modal solution can be employed to solve Maxwell equations. The analytical solutions described in chapter 2 limits numerical operations required thus enabling rapid calculations. The expansion on multipolar waves can bring physical insight about the field distribution and the hybridization of modes couplings. The small size of the nanoparticles with respect to the incident excitation field, tends to favor lowest orders in a multipole development.

b) Spherical nanoparticles are convenient shapes for nanoscale manufacturing. Several novel techniques such as DNA templates [65] have demonstrated the potential for structuring the near field environments using spherical nanoparticles. It must be emphasized that an extension to anisotropic shape of particles is possible within the multipole framework. Elongated particles have been widely investigated for the red shifting of the plasmon frequency resonance to domains where absorption is lower [66, 67].

In this chapter, we first recall some basic results about localized plasmon resonances on a single spherical nanoparticle. The modes of coupled systems can be understood in terms of hybridization of the individual nanoparticle plasmon resonances [62, 68]. It will be emphasized that quite simple components and configurations enable the production of giant field enhancement in nanometer volumes, and may therefore be considered as efficient and compact lenses [55, 65].

As the number of particles is increased, interactions between the individual plasmon resonances become more complex. In particular, the response of complex plasmonic systems depend not only on the incident frequency, but also on the incident electric polarization and the resulting relative phase of the polarization moments induced in the individual nanoparticles.

5.2 Localized plasmon resonance on a single particle

The Mie theory provides a rigorous solution of the electromagnetic response of spherical particles of arbitrary size and is supposed to remain valid provided that macroscopic optical constants can be defined to describe the particle material. For the particles under consideration (from 10 nm to 100 nm), the number of atoms composing the particle are supposed to be sufficient to justify employment of the dielectric permittivity of the bulk material referenced in literature [69]. We remark that the Mie expansion was first dedicated to determine the optical mechanisms responsible for the coloration obtained when adding metallic particles in silica glasses. This technique was secularly employed to produce stained glasses for windows in medieval cathedrals. Various colorations can be obtained depending on the metallic material (gold, silver, copper, zinc ...) and on the size, shape and density of nanoparticles [70, 71].

Fig. 5.1 shows a schematic of a typical process occurring when a metallic nanoparticle is illuminated in the optical range. Let us assume an incident natural white light containing a wide range of wavelengths. These colors are illustrated by the three red, green and blue horizontal arrows

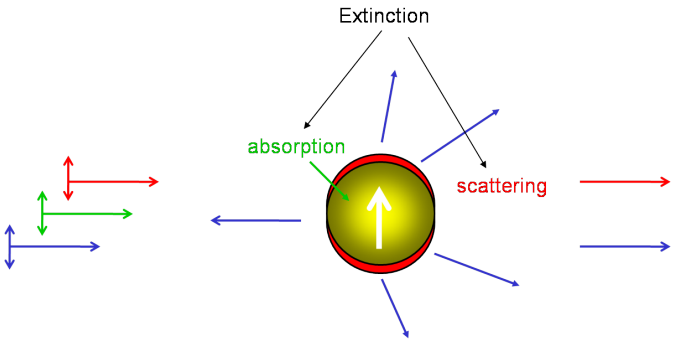

Figure 5.1: Schematic of light interacting with a plasmonic nanoparticle. Scattering and absorption processes produce coloration in the far field and intense fields in the vicinity of the nanoparticle.

indicating the direction of propagation of the excitation wave. The vertical arrows indicate the incident electric field polarization. Around a specific frequency, the incident optical wave can induce a strong resonance of the polarization field inside the particle (the white arrow indicates the direction of the dipolar moment which is collinear to the incident electric field). The resonant polarization produces an enhancement of the scattering process and may also lead to strong dissipations in the particle.

In a homogeneous medium containing a low density of metallic particles, it can be considered that each particle is sufficiently separated from its neighbors to radiate independently. Light reflected by a glass containing metallic nanoparticles will thus essentially contain the resonant frequency of a single nanoparticle, so that the color perceived in the backscattered region will correspond to the resonant wavelength (illustrated here as the blue color). The transmitted light will contain colors which have weakly interacted with the nanoparticle plus the contribution of the resonant frequency. When the particles are small, the plasmonic resonance induces an enhanced absorption in the metal. It results that the glass appears stained and the distribution of light wavelengths in the reflected and transmitted light differ.

In addition to these far field properties, intense fields are produced in the vicinity of the nanoparticle at the plasmon frequency. This latter property is of crucial importance for applications in nano-optics since it enables the production of highly confined electromagnetic fields. Nevertheless, the far field properties can reveal informations on the plasmon excitation and thus provide means for experimental analysis.

5.2.1 Electromagnetic cross-sections

When the incident field can be approximated by a plane wave, it is convenient to express physical quantities in terms of cross-sections. These cross-sections have the dimension of area and define an effective surface of interaction with the incident energy flux required to equalize the energy that is scattered (or absorbed) by the object. Due to energy conservation, the extinction cross-section is equal to:

$$\sigma_{\text{ext}} = \sigma_{\text{scat}} + \sigma_{\text{abs}} \tag{5.1}$$

where σ_{scat} and σ_{abs} are respectively the scattering and absorption cross-sections. Appealing to the far-field approximation of the field, the extinction and scattering cross-sections of a single particle in the Mie framework can be worked out analytically in terms of the field coefficients and respectively expressed [1]:

$$\sigma_{\text{ext}} = -\frac{1}{k_b^2}\,\text{Re}\left[\begin{bmatrix} f_p^{(h)} \\ f_p^{(e)} \end{bmatrix}^{\dagger}\begin{bmatrix} a_p^{(h)} \\ a_p^{(e)} \end{bmatrix}\right] \qquad \text{and} \qquad \sigma_{\text{scat}} = \frac{1}{k_b^2}\begin{bmatrix} f_p^{(h)} \\ f_p^{(e)} \end{bmatrix}^{\dagger}\begin{bmatrix} f_p^{(h)} \\ f_p^{(e)} \end{bmatrix} \tag{5.2}$$

where the $a_p^{(h,e)}$ and $f_p^{(h,e)}$ are respectively the coefficients of the incident field and the scattered fields. It is also possible to produce analytical expressions for local field quantities like individual absorption cross-sections. For lossy scatterers in a lossless host medium, one can obtain individual particle absorption cross-sections by integrating the Poynting vector on a circumscribing sphere surrounding the particle to obtain the formula:

$$\sigma_{\text{abs}} = \sigma_{\text{ext}} - \sigma_{\text{scat}} = -\frac{1}{k_b^2}\text{Re}\left\{f^{\dagger}\,a\right\} - \frac{1}{k_b^2}\,|f|^2 \tag{5.3}$$

The electromagnetic extinction (black line), scattering (red line) and absorption (green line) cross-sections of a nanoparticle have been calculated in the framework of Mie theory and displayed in Fig. 5.2(a) and Fig. 5.2(b) for (a) a 50 nm silver nanoparticle and (b) a 50 nm gold nanoparticle as functions of the incident vacuum wavelength. The nanoparticles are taken to be embedded in a polymeric material of refractive index $n_b = 1.5$. In each plot, a single peak appears illustrating the excitation of a localized plasmon resonance in the particles.

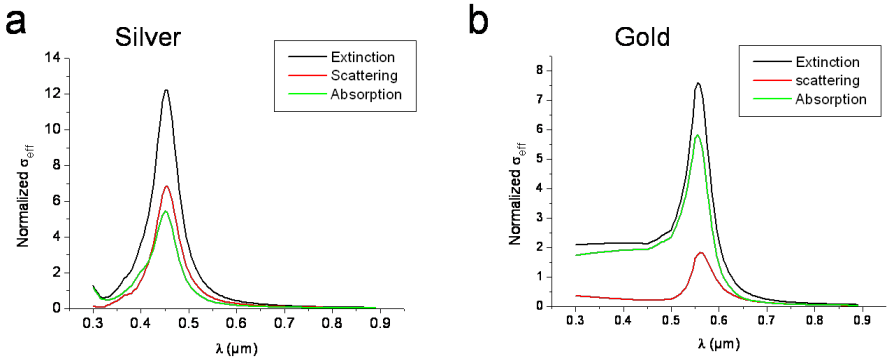

Figure 5.2: Extinction (black line), scattering (red line) and absorption (green line) cross-sections of (a) a 50 nm silver particle and (b) a 50 nm gold particle. The surrounding background has a refractive index $n_b = 1.5$.

In these plots, cross-sections are normalized by the geometrical cross-section of the nanoparticle πR^2. It highlights that interactions between the incident light and the metallic nanoparticle can become one order of magnitude larger than interactions with respect to its geometrical size. One can notice several important differences according to the material. Plasmon resonances occur at shorter wavelengths for silver nanoparticles than for gold nanoparticles. Silver nanoparticles at this size exhibit a narrow resonance and the extinction is roughly equally distributed between scattering

and absorption. In contrast, gold nanoparticles exhibit broader resonances which are dominated by absorption process.

It is important to recall that the incident field induces magnetic and electric multipoles in the particles of increasing orders with respect to their size parameter. Owing to the small size of the nanoparticle compared with the incident excitation field, only the lowest orders are important. In particular, for spheres of diameter below 50 nm, the field scattered by the particles can be approximated by the dipolar term in the Mie expansion tending towards the so-called quasi-static approach.

5.2.2 Quasistatic approach

5.2.2.1 Field generated by a dipolar source

For particles that are small with respect to the incident wavelength, it is convenient to express the scattered field as a dipolar field generated by an oscillating electric dipole moment $\mathbf{p}$ [72]:

$$\mathbf{E}(\mathbf{r}) = -\frac{e^{ik_b r}}{4\pi\varepsilon_0\varepsilon_b r^3}\left\{\left[1 - ik_b r - k_b^2 r^2\right]\mathbf{p} + \left[k_b^2 r^2 - 3(1 - k_b r)\right]\widehat{\mathbf{r}}(\widehat{\mathbf{r}}.\mathbf{p})\right\} \tag{5.4}$$

where $\mathbf{r} = r\widehat{\mathbf{r}}$ is the position in spherical coordinates where the field is calculated.

The asymptotic formulas when $k_b r \gg 1$ and $k_b r \ll 1$ are given respectively by Eq. (5.5) and Eq. (5.6). In the far field region (Eq. (5.5)), the electric field is transverse to $\widehat{\mathbf{r}}$ and behaves as a typical outgoing wave of wavenumber k_b. The electric field amplitude is maximum in the equatorial plane and falls off as $1/r$. The induced dipole at resonance frequency produces an enhanced scattered field that can be detected in the far field region even for small particles.

$$\mathbf{E}_{\text{scat,FF}}(r) \to \frac{k_b^2 e^{ik_b r}}{4\pi\varepsilon_0\varepsilon_b r}(\mathbf{p} - \widehat{\mathbf{r}}(\widehat{\mathbf{r}}.\mathbf{p})) \tag{5.5}$$

The electric field contribution in the vicinity of the nanoparticle given by Eq. (5.6) is essentially the quasi-static dipolar field that is analog to the electrostatic field when omitting the time dependence. The $1/r^3$ dependence implies that this field is negligible far from the dipole. However, this field, predominantly statique in nature, remains confined to the vicinity of the particle and its amplitude is maximum along the polarization vector $\mathbf{p}$.

$$\mathbf{E}_{\text{scat,NF}}(r) \to \frac{1}{4\pi\varepsilon_0\varepsilon_b}\frac{3\widehat{\mathbf{r}}(\widehat{\mathbf{r}}.\mathbf{p}) - \mathbf{p}}{r^3} \tag{5.6}$$

5.2.2.2 Dipolar polarizability

Provided that the excitation field is not too intense, the dipolar moment is related linearly to the excitation field via a complex scalar number α [73]:

$$\mathbf{p}(\omega) = \varepsilon_0\varepsilon_b\alpha(\omega)\mathbf{E}_{exc}(\omega) \tag{5.7}$$

where $\alpha(\omega)$ is the dipolar polarizability and $\mathbf{E}_{exc}$ is the local electric field. In the static limit:

$$\lim_{\omega\to 0}\alpha(\omega) \longrightarrow 4\pi a^3\frac{\varepsilon_s - \varepsilon_b}{\varepsilon_s + 2\varepsilon_b} \tag{5.8}$$

One remarks that the term in the denominator of the polarizability goes to zero when $\mathrm{Re}[\varepsilon_s(\omega)] \rightarrow -2\varepsilon_b$ leading to an enhancement of the dipolar moment induced in the particle. This condition can be approximately fulfilled by metallic materials in the visible range producing the dipolar LSPRs.

5.2.2.3 Large particles

One must remember that the electrostatic approach only provides a first approximation of the dipolar polarizability. To illustrate the defaults of this model, the electromagnetic cross-sections of a 100 nm silver nanoparticle sphere have been rigorously calculated in the Mie multipole framework and displayed in Fig. 5.3(a). Two peaks now appear in the spectrum. The broad peak in the large wavelength range ($\lambda_0 = 550$ nm) corresponds to the dipolar resonance of the particle. Fig 5.3(c) illustrates this resonance which exhibits two intense spots in the vicinity of the particle revealing the excitation of dipolar-type resonance in the particle. Although, electrostatic theory predicts the existence of this resonance, it describes neither the red shift (see Fig. 5.1(b) and Eq. (5.8)) of the resonance frequency nor the broadening of the resonance width when the size of the particle is increased. Nevertheless, all of these effects remain dipolar in nature. Higher order developments of the dipolar polarizability for spherical objects are required to introduce contributions such as depolarization effects [74] or radiation damping [75]. One technique which includes all these effects is to express the dipolar polarizability in terms of the first electric coefficient in the Mie expansion $T_1^{(e)}$ as [3]:

$$\alpha = \frac{6\pi}{ik_b^3} T_1^{(e)} \tag{5.9}$$

Furthermore, due to the large size of the particle, a second peak has appeared in the spectrum at higher frequencies. The electric field intensity map at $\lambda_0 = 430$ nm displayed in Fig 5.3(b) shows four high intense spots distributed at the surface of the particle. This distribution corresponds to a quadrupolar-type resonance that cannot be modeled with a dipolar approximation. It can be observed that absorption contributes to the quadrupolar resonance. This can be partly explained by an intrinsic strong absorption of metals in the blue range frequency due to a high imaginary part in the dielectric constant.

Couplings between closely spaced plasmonic nanoparticles have attracted considerable interest since in certain configurations, coupled plasmonic particles can induce much larger local field enhancements than those near isolated nanoparticles.

5.3 Localized plasmon resonances in coupled nanoparticles

We now consider two nanoparticles separated by a distance d of a few nanometers so that the individual localized plasmon modes strongly interact. The interaction creates new plasmonic modes in the coupled system. It has been demonstrated that these modes can be considered as a hybridization of the individual eigen-modes and must consequently respect the symmetries of the system.

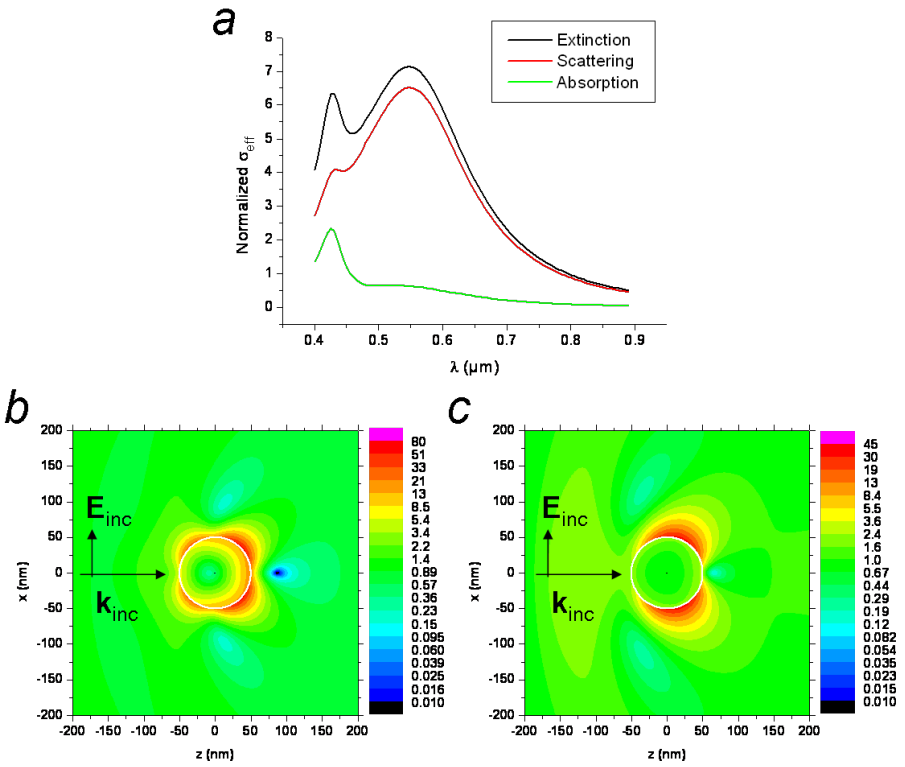

Figure 5.3: (a) Electromagnetic cross-sections of a 100 nm diameter silver particle. (b) Intensity colored map of plasmon resonances at λ_0 = 430 nm corresponding to the quadrupolar resonance and (c) λ_0 = 550 nm corresponding to the dipolar resonance. The surrounding background has a refractive index n_b = 1.5.

Table 5.1 shows the possible dipolar eigen modes of a dimer resulting from a hybridization of the individual eigenmodes. Assuming a dipolar behavior of the nanoparticle response, couplings between localized plasmons can occur for individual induced dipoles directed either both transversally (T1, T2) to the dimer axis or both longitudinally (L1, L2). Although, the dipolar approximation fails to describe strong plasmonic couplings, the distinction between longitudinal and transversal interactions can still be convenient. It will be shown below that this distinction can still be made in the multipole formalism.

Table 5.1: Possible dipolar eigen modes for two coupled plasmonic particles.

Transverse eigenmodes	T1	↑	↑	In-phase mode
	T2	↓	↑	Opposite-phase mode
Longitudinal eigenmodes	L1	→	→	In-phase mode
	L2	←	→	Opposite-phase

Longitudinal couplings have been intensively studied for the giant enhancements they produce in the nanogap formed by the coupled nanoparticles [55, 59–64, 68]. Longitudinal modes can be optimally coupled when illuminating the dimer at normal incidence with an incident electric

field polarized along the dimer axis. Conversely, transverse modes are optimally excited by waves propagating along the dimer axis or by evanescent couplings produced by total internal reflection. Transverse couplings have raised less attention than longitudinal ones since the field amplitudes in the nanogap between the particles are weak. Longitudinal couplings on the other hand have demonstrated field enhancements of several orders of magnitude. As we are interested in focusing light in nanometer scaled volumes, a particular attention will be devoted in this chapter to longitudinal plasmon couplings.

5.3.1 Longitudinal couplings

Fig. 5.4 displays a schematic of the numerical experiment undertaken in this section. Two identical gold nanoparticles 50 nm in diameter, embedded in a dielectric background of refractive index $n_b = 1.5$, are illuminated by a plane wave with the electric field oscillating along the symmetry axis of the dimer.

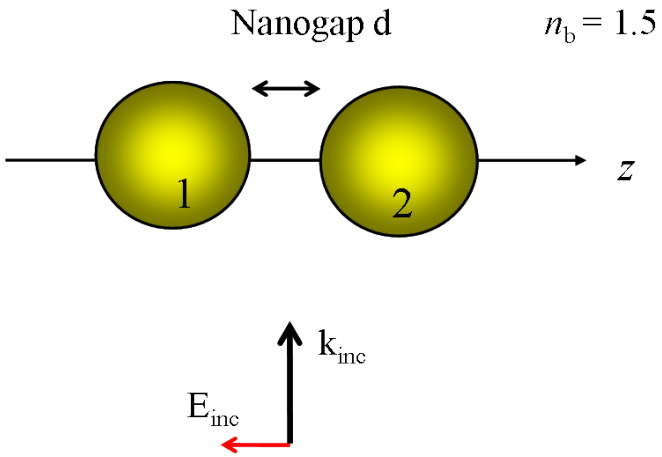

Figure 5.4: Schematic of the numerical experiment. Two identical gold nanospheres 50 nm in diameter, embedded in a dielectric background of refractive index $n_b = 1.5$, are placed along the z-axis defining a nanogap of dimension d. The system is illuminated by a plane wave with a electric polarization along the dimer axis z.

We first investigate the far field response of the coupled system in Fig. 5.5(a) by rigorously calculating the electromagnetic extinction (black line), scattering (red line) and absorption (green line) cross-sections when illuminating the system at normal incidence. A strong resonance occurs at wavelengths of 630 nm, corresponding to coupled resonances of longitudinal modes. Comparison of this peak with the extinction cross-section of the isolated particle (dashed line in Fig. 5.5(a)) shows that the coupled resonance is red-shifted. This red-shift can be explained using the hybridization model of the individual plasmons [62, 68]. Fig. 5.5(b) displays the energy diagram of the possible plasmonic longitudinal mode hybridization (the red arrow illustrates the induced dipolar moment in the individual nanoparticle). The longitudinal in-phase interactions is analog to a bonding atomic hybridization which occur for lower incident energy than the plasmon resonance

in the isolated particle. It results that the in-phase mode appears at larger wavelengths (i.e in the red region of the spectrum) [59].

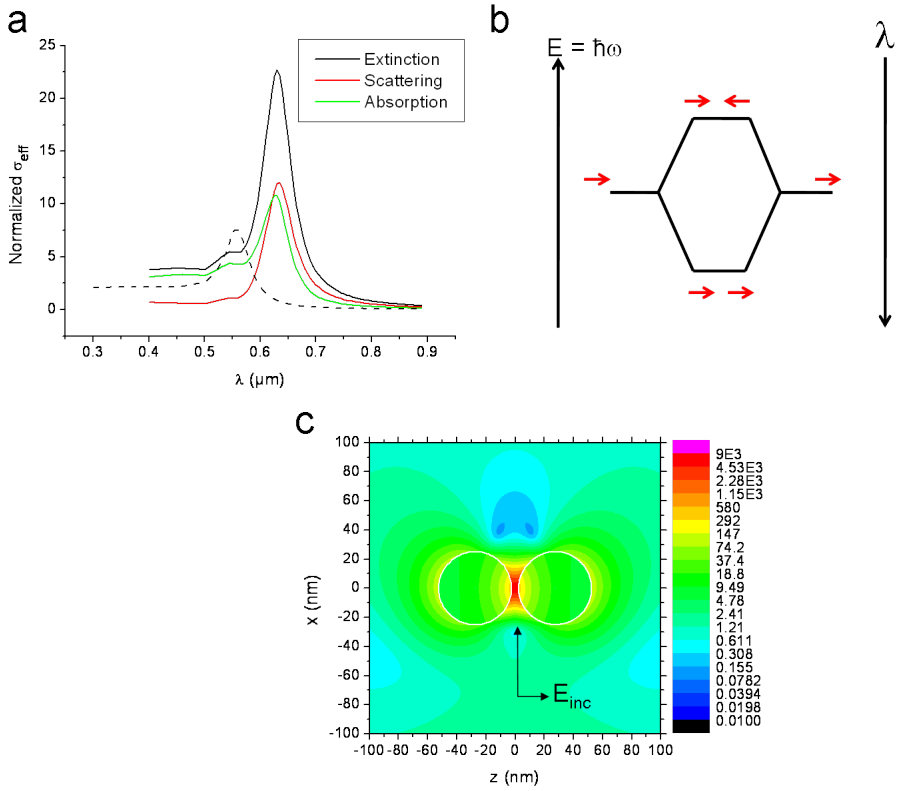

Figure 5.5: (a) Extinction (black line), scattering (red line) and absorption (green line) cross-sections for the coupled system, and extinction cross-section for the isolated particle (dashed line). (b) Qualitative energy diagram of the plasmon hybridization. (c) Electric field intensity map for the two coupled nanoparticles illuminated at normal incidence (c.f. the black arrow in (c)) at $\lambda_0 = 630$ nm. The 50 nm gold nanoparticles are separated by $d = 5$ nm and the surrounding background has a refractive index $n_b = 1.5$.

For this red-shifted coupled mode, the incident electric field parallel to the dimer axis induces in-phase longitudinal oscillations of the polarization moments of each particle. These oscillations induce surface charges of opposite sign which are responsible for the strong electric field enhancement in the dielectric inter-particle gap. Fig. 5.5(c) illustrates the strong near field enhancement between the spheres when the dimer is illuminated at $\lambda_0 = 630$ nm. We remark that there exists a weaker secondary peak at higher frequency which is made possible thanks to quadrupolar response contributions.

We introduce the local induced polarization moment $\mathbf{P}$ in the nanoparticle which can be defined in terms of the internal field:

$$\mathbf{P}(\mathbf{r},\omega) = \varepsilon_0(\varepsilon_s(\omega) - \varepsilon_b)\mathbf{E}_{\text{int}}(\mathbf{r},\omega) \tag{5.10}$$

where ε_0 is the permittivity of vacuum and ε_s and ε_b are the relative permittivities of the metal and the background media respectively.

We are then interested in extracting the longitudinal components of the polarization moment in the individual particle which are responsible for the creation of surface charges and consequently for intense fields in the nanogap. Thanks to the numerical approach employing Mie theory and expansions of the fields on the vector spherical harmonics, the longitudinal components of the induced polarization moment in the nanoparticle can be extracted in the multipolar framework. In this study, high multipolar orders are required to accurately reconstruct the field which will be taken into account by imposing $N = 20$ in Eq. (**??**). The dispersion of the dielectric constant of gold is interpolated from the Palik database [69]. The extraction of the longitudinal components of the field requires one to pay particular attention on the Scalar Spherical Harmonics that are defined in in chapter **??** in terms of the associated Legendre polynomials $P_n^m(\cos\theta)$.

$$Y_{nm}(\theta,\phi) \equiv c_{n,m} P_n^m(\cos\theta)\exp(im\phi) \tag{5.11}$$

where

$$c_{n,m} \equiv \left[\frac{2n+1}{4\pi}\frac{(n-m)!}{(n+m)!}\right]^{\frac{1}{2}} \tag{5.12}$$

The associated Legendre polynomials $P_n^m(\cos\theta)$ have the following property:

$$\forall m \neq 0 \quad P_n^m(\pm 1) = 0 \tag{5.13a}$$

$$P_n^0(\pm 1) = (\pm 1)^n \tag{5.13b}$$

It results that the electric field distribution close to the z-axis can be relatively well described by the $(n,m) = (n,0)$ contributions (c.f. the Scalar Spherical Harmonics in Fig. 2.2). This is clearly highlighted in Fig. 5.6(a) where the electric field intensity has been reconstructed under the same conditions as Fig. 5.5(c) but only taking into account the $(n,m) = (n,0)$ contributions. One can notice that the intensity maps are identical demonstrating that our approach enables to essentially describe the longitudinal interactions of the localized plasmon in the individual particle. By defining the longitudinal polarization moment as:

$$\mathbf{P}_{long}(\mathbf{r},\omega) = \varepsilon_0(\varepsilon_s(\omega) - \varepsilon_b)\mathbf{E}_{int,(n,0)}(\mathbf{r},\omega) \tag{5.14}$$

one gets access to the relative phase of the induced longitudinal polarization components responsible for the creation of surface charges along the axis of the dimer by projecting the field along the radial direction:

$$\mathbf{P}_{long}(\mathbf{r},\omega).\widehat{\mathbf{r}} = \varepsilon_0(\varepsilon_s(\omega) - \varepsilon_b)\mathbf{E}^{(Y)}_{int,(n,0)} Y_{n,0} \tag{5.15}$$

where the origin of $\widehat{\mathbf{r}}$ lies at the center of the particle. Fig. 5.6(b) displays the phase of the induced longitudinal polarization moment inside the particle. It is clear that the longitudinal moments oscillate in phase. It must be stressed that not only the dipolar term has been taken into account and that higher multipolar order ($n \geq 1$) contribute to the field. Nevertheless, the phase of the longitudinal induced moment $\mathbf{P}_{long}(\mathbf{r},\omega).\widehat{\mathbf{r}}$ highlights "bipolar" oscillations demonstrating that the distinction made in the dipolar approximation between transversal and longitudinal modes in linear chains of particles is still relevant in the vectorial multipolar framework.

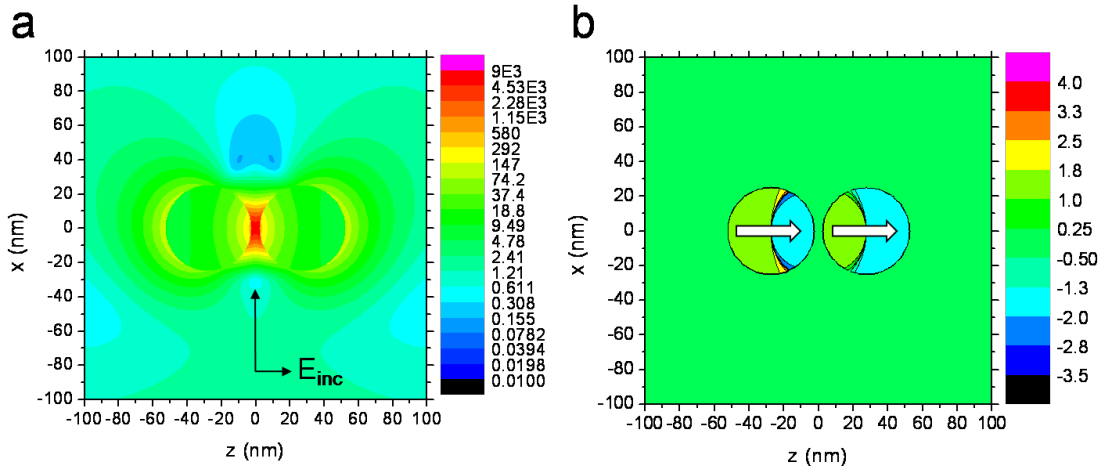

Figure 5.6: (a) Reconstructed electric field intensity map when taking only $(n, m) = (n, 0)$ contributions and (b) phase of the individual induced longitudinal moment. The 50 nm gold nanoparticles are separated by $d = 5$ nm and illuminated at normal incidence, at $\lambda_0 = 630$ nm. The surrounding background has a refractive index $n_b = 1.5$.

In the quasistatic approximation, the internal field is considered as constant over the complete volume of the particle. It results that the dipolar moment can be expressed as:

$$\mathbf{p}(\omega) = V_s \varepsilon_0 (\varepsilon_s(\omega) - \varepsilon_b) \mathbf{E}_{int,dip}(\omega) \tag{5.16}$$

where V_s is the volume of the sphere and $\mathbf{E}_{int,dip}$ is the dipolar contribution of the electric field.

Nanoparticles dimers have been essentially investigated for the in-phase mode producing intense and highly confined fields in the nanogap defined by the interdistance between the particles. Due to a weak total polarization moment, longitudinal opposite-phased modes cannot be excited by a straightforward plane wave illumination on strongly coupled dimer of nanoparticles (typical separation distance of 5-10 nm). However, It has been demonstrated that interactions of dimers with an additional particle [9, 76] or localized emitters enables the excitation of asymmetric modes.

5.4 Control of light localization

Metallic nanostructures offer the opportunity to strongly focus light and to enhance light-matter interactions at the nanometer scale via the excitation of localized surface plasmon resonances. In 2002, Stockman et al. demonstrated the dynamic control of the field enhancement at nanometer scale in arbitrary nanostructures [77] by adjusting the phase and the polarization of an excitation pulse. Active control of field localization has been experimentally demonstrated through the use of an iterative learning algorithm to shape the femtosecond excitation pulse [78]. Deterministic structures such as arrays of spherical nanoparticles have been investigated by Koenderink et al. [79] to serve as unique and reproducible lithographic masks for imprinting different near field patterns. They varied the angle of incidence and polarization of the continuous excitation beam in order to

produce a variety of patterns in a photosensitive substrate. Aperiodic arrays of coupled localized plasmonic resonances have also been investigated to provide reproducible nanostructures surfaces for enhanced Raman spectroscopy. These studies convincingly demonstrated that incident beam shaping can induce different field distributions in a single metallic nanostructure.

In 2006, Le Perchec et al. controlled the localization of light in coupled slits milled in a metallic substrate [80]. The slits had a thickness of 200 nm and were separated by a distance of 500 nm. When illuminated in oblique incidence in the infrared spectrum, they coupled incident propagating light to both symmetric and anti-symmetric modes. By the use of a second identical frequency propagating wave in opposite incidence, they could switch the near field enhancement from one slit to the other via phase adjustments. This simple system provided a means to conceive subwavelength optical switch components controlled from the far field region. Very recently, Volpe et al. [76] investigated spatial phase modulations of high order beams such as Laguerre-Gaussian beams in order to control the near field in plasmonic nanostructures. They considered two 50 nm gaps formed by three 500 nm aligned gold bars and demonstrated that spatial phase modulation of the incident beam enables switching light on and off in either of the two sites.

In this section, we theoretically study a linear trimer of identical spherical nanoparticles to tune the localization of light at the nanometer scale (~55 nm). In particular, we investigate the near field enhancement occuring between gold nanospheres 50 nm in diameter. The three spherical nanoparticles are arranged to form two identical nanogaps in which the near field can be strongly enhanced. This provides a simple system with two coupled nanogaps separated by a distance of about a tenth of the incident wavelength. It will be shown that this a priori symmetric system enables the concentration of light in a single cavity while employing a single illumination plane wave [9].

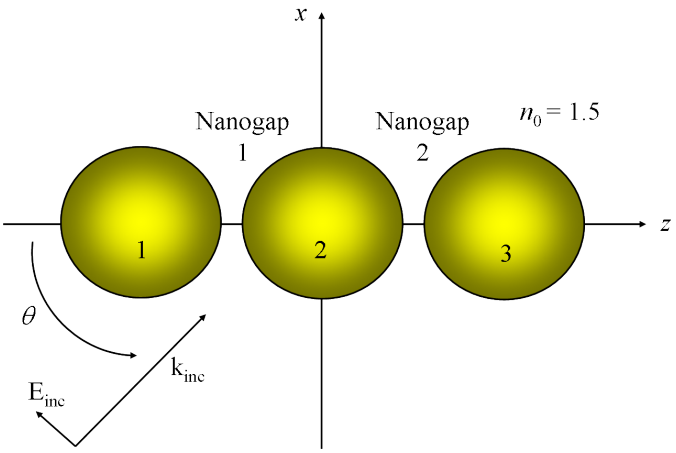

Figure 5.7: Schematic of the numerical experiment. Three identical gold nanospheres 50 nm in diameter, embedded in a dielectric background of refractive index $n_b = 1.5$, are placed along the z-axis. The system is illuminated by a plane wave with a TM polarization with an angle of incidence θ between the propagation direction and the z-axis. Calculations are performed using generalized Mie theory combined with an analytic multiple scattering formulation.

This model system is illuminated by a plane wave with TM polarization (the magnetic field is

perpendicular to the plane presented in Fig. 6.3) and an angle of incidence, θ, tunable between 0 (propagation along the z-axis) and 90 degrees. The strong contrasts of near field intensities at scales much smaller than the incident wavelength require a full electromagnetic study based on solving the Maxwell equations.

We investigate the far field response of the trimer by rigorously calculating the spectral response of the extinction cross-section for different angles of incidence (Fig. 5.8(a)). For an incident angle $\theta = 0°$ (blue line) corresponding to an illumination along the z-axis, only one maximum appears at the wavelength of 560 nm, which is almost the wavelength of resonance of the isolated sphere (red line). Assuming an incident electric field along the x-axis, it can be deduced that this resonance is due to plasmon oscillations occurring transversally to the chain axis resulting in weak couplings between the individual nanoparticles resonances. At normal incidence ($\theta = 90°$: black line), a stronger resonance occurs at the wavelength of 665 nm, corresponding to the well-known red-shifted coupled resonance of in-phase longitudinal modes [59]. Fig. 5.8(b) illustrates the strong near field enhancement between the spheres when the trimer is illuminated at $\lambda_0 = 665$ nm. When the chain is illuminated at normal incidence, only in-phase longitudinal oscillations of the polarization moments are excited. These oscillations induce surface charges of opposite sign in the dielectric inter-particle gap responsible for the strong electric field enhancement. Such modes have been studied extensively in the context of dimers of metallic spheres and nanoshells [55, 59–64]. We remark that for the case of normal incidence, there exists a weak second peak at higher frequency which is made possible thanks to quadrupolar response contributions. At intermediate angles of incidence (like the case $\theta = 45°$ displayed in Fig. 5.8(a)), we observe two peaks at frequencies close to those observed respectively at $\theta = 0°$ and $\theta = 90°$.

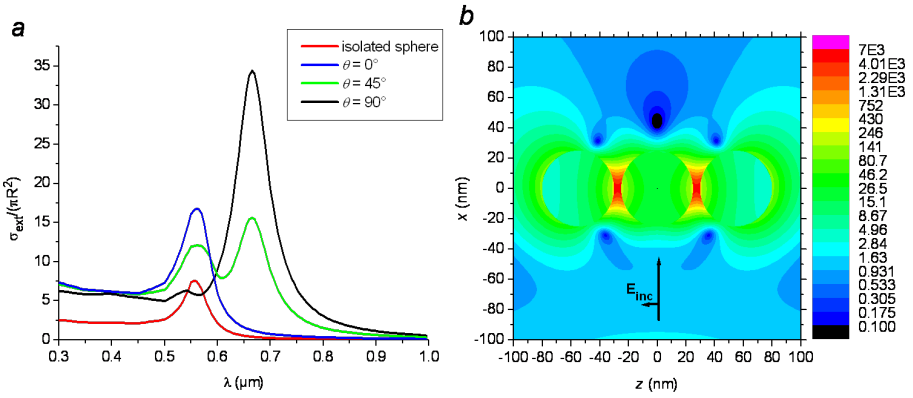

Figure 5.8: (a) Extinction cross-section of a chain of three gold particles of diameter $D = 50$ nm (red line) separated by $d = 5$ nm in the full electromagnetic approach. The refractive index of the surrounding is n_b=1.5. Different angles of incidence are displayed: $\theta = 0°$ (blue line), $\theta = 45°$ (green line) and $\theta = 90°$ (black line). The isolated sphere extinction cross-section is also displayed (red line). (b) Electric field intensity $\|E\|^2/\|E_{inc}\|^2$ map in log scale for a trimer illuminated at $\lambda_0 = 665$ nm under normal incidence.

Table 5.2 illustrates the dipolar longitudinal eigenmodes that may be excited in a linear trimer. Although the dipolar approximation fails to describe accurately the resonance when the particles are strongly coupled, it enables a clear distinction between modes that are perpendicular (transverse)

and parallel (longitudinal) to the chain axis [81]. From the extinction cross-section displayed in Fig. 5.8(a), one can observe that only the in-phase modes denoted L1 is clearly visible. This observation may seem surprising since except for illumination at $\theta = 0°$ where the symmetries of the configuration impose in-phase modes, coupling between the incident field and opposite-phase modes may be possible when illuminating the system at oblique incidence. Inspection of the opposite-phase modes in Table 5.2 shows however that the total dipolar moment involved in these modes is weaker than that occurring for in-phase modes. Consequently, the scattering process remain moderate and these modes may be difficult to observe in extinction cross-section plots.

Table 5.2: Possible longitudinal dipolar eigen modes for a linear chain of three plasmonic particles.

Longitudinal eigenmodes	L1	→	→	→	In-phase mode
	L2	←	→	→	Opposite-phase
	L3	←	→	←	modes

Let us emphasize that we are interested in the excitation of an opposite-phase mode that would lead to a vanishing of the field in one of the nanogaps. This purpose requires an excitation via the far field of modes that are associated with a weak dipolar moment. Fig. 5.9(a) displays the near field intensity enhancement calculated at the center of the nanogap as a function of the incident wavelength, when the incident angle θ is equal to 45 degrees. These plots show that the field intensities in the two nanogaps are quite different, but most interestingly they reveal the counterintuitive occurrence that at $\lambda_0 = 595$ nm (green line) a rather strong field intensity enhancement in gap 2 is concurrent with a near vanishing of the field in gap 1 (the ratio is larger than 500). This phenomenon is even more conspicuous in the near field intensity map displayed in Fig. 5.9(b) in logarithmic scale that clearly shows that at $\lambda_0 = 595$ nm, the light intensity is confined in only one site. This is the most striking result of this study: the sub-wavelength nanogap 1 is turned-off and the light intensity is almost entirely localized inside nanogap 2 while both nanogaps are separated by only 55 nm. It appears that this phenomenon cannot be observed from the far field response since the extinction cross section (green line in Fig. 5.8(a)) does not exhibit any notable feature. We next move towards the full understanding of the longitudinal eigen modes involved in this phenomenon, which will require the extraction of longitudinal terms in the multipole formalism.

We now apply the formalism described in the previous section to study the phenomenon observed in Fig. 5.9. Fig. 5.10(a) displays the longitudinal multipole contributions to the field at $\lambda_0 = 595$ nm and $\theta = 45°$ obtained by reconstructing the field intensity map with $(n, m) = (n, 0)$. It highlights that the vanishing of the near field in nanogap 1 associated with the high intensity enhancement in nanogap 2 are essentially obtained. It shows that the intensity contrast observed in Fig. 5.9 is due to the excitation of longitudinal modes in the structure. More precisely, the phase of the longitudinal electric field displayed in Fig. 5.10(b), obtained under the same conditions as Fig. 5.10(a), shows that the mode L2 depicted in Table 5.2 is predominantly excited. Let us emphasize that the electric field oscillations occurring on the particles are principally dipolar in nature. It means that the oblique incidence permits retardation between the responses of the individual particles allowing the excitation of an opposite-phase mode at a specific frequency.

Fig. 5.10(c) displays the extinction cross-section for the longitudinal modes obtained by imposing $m = 0$ when reconstructing the field, superposed with the total extinction cross-section as

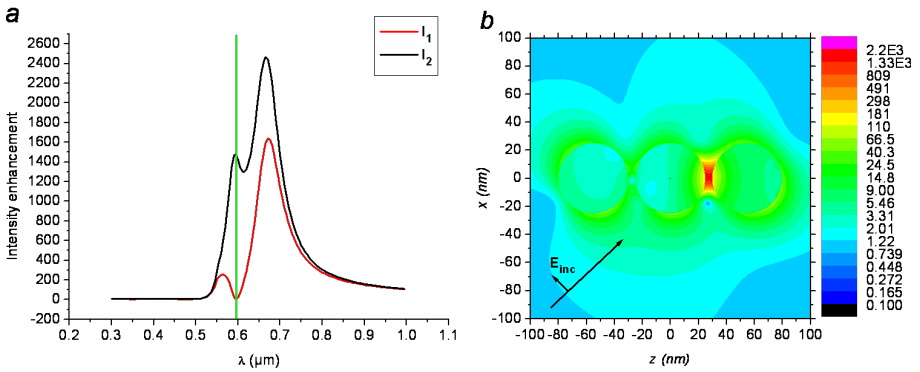

Figure 5.9: (a) Intensity enhancement in nanogap 1 (red line) and nanogap 2 (black line) for θ = 45°. The vertical line indicates the wavelength of 595 nm where the intensity contrast is maximum. (b) Electric field intensity, $\|E\|^2/\|E_{inc}\|^2$, map in log scale at λ_0 = 595 nm and θ = 45°.

calculated in Fig. 5.8(a) (green line). With this technique, the dominating transverse mode can be filtered and it appears that the excitation of the mode L2 is associated with a peak of the extinction crosssection. The oblique illumination has enabled the coupling of the incident propagating light to an opposite-phase mode that is responsible for a vanishing of the field in nanogap 1 while the field in nanogap 2 is strongly enhanced.

Furthermore, Fig. 5.10(a) evidences a weak longitudinal induced polarization inside sphere 1 indicating that L2 is not the only mode which is excited, but that a combination of the three longitudinal modes (Table 5.2) is involved. This result shows that it is possible to nearly extinguish the longitudinal moment of a metallic nanoparticle by simply coupling this particle with a dimer of identical particles.

A similar vanishing of the polarization moment of metallic nanoparticles has been observed in the asymmetric dolmen structure by Zhang et al. [82, 83]. They have demonstrated that the so-called Electromagnetic Induced Transparency (EIT)-like phenomenon was achievable thanks to couplings between a bright and a dark plasmonic element in a dolmen-like plasmonic molecule. The bright (radiative) element easily couples to the incident light while the dark element supports a resonance that cannot be directly excited from the far field area. But this dark resonance can be excited by near field couplings with the bright atom. A destructive interference between the direct excitation of the radiative element by the incident field and the indirect excitation via the scattering of the dark element leads to turn-off the bright atom and produces a transparency window in the far field. Certain similarities between this EIT-like phenomenon and the phenomenon investigated here in the symmetric trimer illuminated in oblique incidence can be observed. In particular, the destructive interference that occurs in the bright element of the dolmen-like structure is similar to the extinction of the longitudinal dipolar contribution in sphere 1.

Fig. 5.11 presents calculations of (a) the real and (b) imaginary parts of the electric field at the center of nanogap 1. The vanishing of the electric field inside nanogap 1 is associated with a dip of the imaginary part of the z-component of the electric field (indicated by the line in fig. 5.11) and with a strong dispersive behavior of the real part, similar to observations in EIT-like phenomenon (see for example the figure 2b of Ref. [82]). The investigation of the local electric field in nanogap

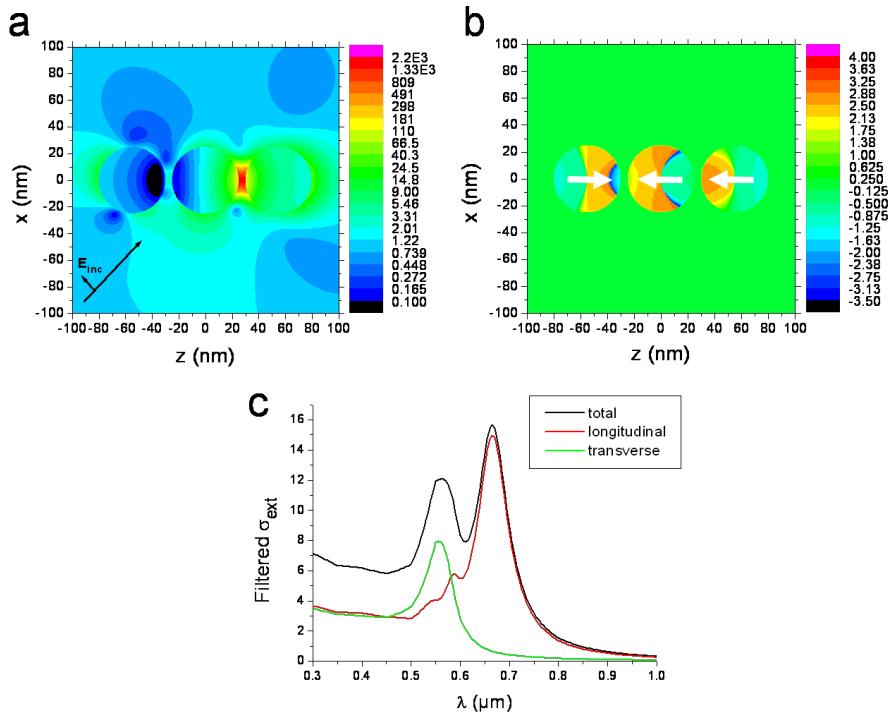

Figure 5.10: (a) Electric field intensity $||E||^2/||E_{inc}||^2$ map in log scale of the longitudinal contributions reconstructed imposing $(n, m) = (n, 0)$ in Eq. (**??**), (b) phase of the field reconstructed with the terms $E^{(Y)}_{n,0}(r)Y_{n,0}$ in Eq. (**??**) at $\lambda_0 = 595$ nm and $\theta = 45°$ and (c) extinction cross-section at $\theta = 45°$ for the total field (black line), the longitudinal (red line) and transversal contributions (green line).

1 can be related to an effective polarizability of spheres 1 and 2. However, unlike the investigation of Zhang et al., the susceptibility of the entire system cannot be deduced from the field occurring inside the cavity 1 because in our case, the field is not coupled to a dark mode: spheres 2 and 3 have in-phase longitudinal dipoles which are required for the observation of a high contrast of light intensity between the both nanogaps. More precisely, the global susceptibility of our system can not be canceled by the couplings to antisymmetric modes. This can be evidenced by the fact that these modes do not induce any dip in the extinction cross-section plotted in Fig. 5.8(a).

This study demonstrates that antisymmetric modes can be excited by a propagating plane wave in a linear trimer of identical particles. Furthermore, we show that in a narrow frequency range, symmetric and antisymmetric mode-balancing extinguishes the dipolar longitudinal moment of a metallic nanosphere coupled to a dimer composed of identical nanospheres. This nearly zero longitudinal moment of sphere 1 leads to a near vanishing light intensity in nanogap 1, and the high longitudinal moment of sphere 3 leads to strong enhancement of light intensity in nanogap 2. Finally, we wish to emphasize that this phenomenon occurs in a simple fully sub-wavelength system by employing straightforward far-field control in the harmonic regime. Specifically, it enables switching of light between two identical nanogaps separated by a $\lambda_0/10$ distance.

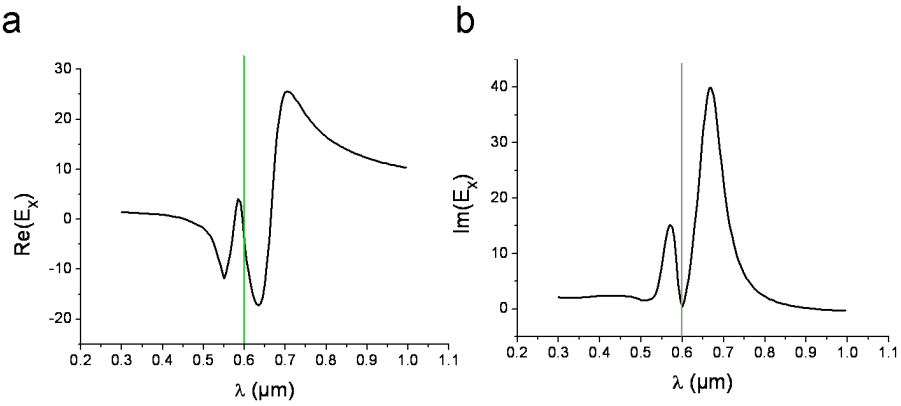

Figure 5.11: (a) Real and (b) imaginary part of the z-axis component of the electric field calculated at the center of cavity 1. The vertical line indicates the wavelength of 595 nm where the intensity contrast is maximum.

5.5 Conclusion

Nanoparticles have been studied in this chapter as efficient tool for increasing the local electric field and enhance interactions with the surrounding medium. The strong focusing of light obtained thanks to the excitation of localized plasmon resonances provide confinement unachievable with dielectric materials. In addition, strong interactions between individual localized plasmon resonance offer the opportunity to control the position of the field at $\lambda/10$ scale. The design of deterministic structures provides new types of optical lenses where both the dimension of the focal point and the control of its position reach the nanometer scale. Interestingly, the nanometer scaled confinement of light opens a way towards straightforward interactions of light with a single emitting molecule.

Chapter 6

Single emitter radiation close to metallic nanoparticles

6.1 Introduction

In the previous chapters, different optical systems such dielectric lenses or metallic nanoparticles have been investigated for their ability to focus light in small volumes. A reason invoked for using such systems was to increase the local EM field in the focal volume enhancing by the way potential interactions with the surrounding medium. As an example, the enhancement of the local electric field was discussed in chapter 4, in the context of FCS, as a mean to increase the fluorescence rate of nearby molecules. In that purpose, a microsphere was introduced in the path of a focused beam to increase the electric field density (defined as the average intensity per volume unit). The reduction of the focal volume has enabled a reduction of the number of fluorescent emitting molecules observed while preserving a sufficient signal/noise ratio for the detected signal. In addition, it must be recalled that a slight redirection of light has been induced by the microsphere contributing to increase the collected signal. An underlying aim of such investigations relies into the need for improving interactions of electromagnetic radiations with unique sources of light such as fluorescent molecules or quantum dots.

Metallic nanostructures are currently considered as key elements for the control of light interactions with quantum emitters (like quantum dots and fluorescent molecules) since plasmon resonances enable to concentrate light and increase the excitation rates in tiny volumes potentially containing a reduced numbers of quantum emitters. The increase of the excitation rate is indeed associated with an increase of the absorption probability for a two-level atomic system.

Reciprocally, it is well admitted, since the work of Purcell, that spontaneous emission of a single emitter can be strongly perturbated by resonant electromagnetic couplings with its external environment. Resonant fields such as those achieved in Fabry-Perot cavities can strongly enhance the spontaneous emission rates and amplify stimulated emission rates for lasing systems. In contrast, full photonic bandgaps in photonic crystals or disorders materials would enable an inhibition of the spontaneous emission since no relaxation channel is available.

Metallic nanostructures also permit to enhance the radiative decay rates of nearby emitters [55, 56, 59, 61, 65, 84–87]. New relaxation channels are provided by the metallic environement near the single emitter via the excitation of plasmon resonances reducing the lifetime in the excited state (inversely proportional to the decay rate). It results an increased number of photons emitted per unit of time and a potential enhancement of the radiated power. The latter property has been thoroughly investigated in the case of a single emitter coupled to a single nanoparticle [66, 67, 88–92]. It has been shown that the radiative decay rates strongly depend on the distance between the

emitter and the metallic nanoparticle. This distance has to be precisely controlled since at very short distances from the surfaces (a few nanometers), non radiative relaxation dominates and the quantum efficiency drops. The coupling efficiency between emitters and the metallic structures also depends on the orientation of the dipolar source with respect to the dipolar modes supported by the metallic particles. A longitudinal coupling geometry significantly enhances the emission decay rates while a transverse interaction leads to moderate enhancements [67, 92–94] as explained in the previous chapter.

In addition to radiative decay rate enhancements, localized plasmon resonances on metal nanoparticles enable a redirection of the radiated signal. Recently, the ability of nanoparticles to control the angular emission of single molecules has been investigated [95, 96]. This possibility is particularly important since a high directivity facilitates both the excitation of a quantum emitter by a collimated beam as well as the collection of the radiated light.

Nanoparticles act analogously to radiofrequency antennas which convert propagating radiations into electrical signal (receptor) and vice-versa. The recent concept of optical nanoantennas has been based on using plasmonic nano-structures to tailor the electromagnetic environment near a quantum emitter in order to enhance the photoluminescence signal by optimizing: (a) the local excitation rate, (b) the spontaneous emission rate, and (c) the collection efficiency [97–99]. In other words, nanoantennas are plasmon based optical transducers employed to increase couplings between optical radiations and atomic transitions of matter. Nanoantennas are promising tools for enhancing fluorescent spectroscopy, scaling down lasing systems, decouple quantum dots radiative emission and optimize single photon sources for quantum physics and integrated optics [100].

In this chapter, we focus our attention on the radiations properties of a single dipolar emitter located close to a single nanoparticle. It will be emphasized that the couplings between the polarization of the single emitter and the polarization moment induced in the nanoparticle is an essential parameter to predict radiation rates and directivity. In particular, longitudinal couplings enable enhancement of the spontaneous decay rates while transverse couplings spoil decay rates but permits a redistribution of dipolar emission. Consequently, it will result in a simple strategy to design compact optical nanoantennas employing nanoparticles.

6.2 Spontaneous emission of a single emitter close to a nanoparticle

Nanoparticles have been studied in the previous chapter as efficient tools for increasing the local electric field intensity. The question arising now is how a single emitting system is influenced by the presence of a nanoparticle in its near field? This question was partly investigated in Chapter 4, when a dielectric microsphere was employed for enhancing Fluorescent Correlations Spectroscopy signal. This enhancement has been attributed to an increase of the excitation density and of the collection efficiency (c.f. Eq. (4.1)). Let us remind that the quantum efficiency has been assumed to be close to unity since slightly affected by non-absorbing materials. Metallic materials however suffer from inherent losses in the visible range that may affect the quantum efficiency. It means that a part of the emitted light will be absorbed by the metallic material and consequently will not propagate to the far field domain. The fluorescence detected signal enhancement Γ_F/Γ_F^0 of a

single-molecule (with respect to a free-space dipolar radiation) can be expressed in the following equation:

$$\frac{\Gamma_F}{\Gamma_F^0} = \kappa_{col}\eta\frac{\Gamma_{exc}}{\Gamma_{exc}^0} \tag{6.1}$$

where κ_{col} is the collection efficiency enhancement that is defined as the power per solid angle integrated over the objective angular aperture normalized by the collection efficiency when the dipole radiate in the free space. The excitation rate enhancement $\Gamma_{exc}/\Gamma_{exc}^0$ is defined as $|\mathbf{n}_p.\mathbf{E}(r_p)|^2/|\mathbf{n}_p.\mathbf{E}_0(r_p)|^2$ where $\mathbf{n}_p$ is the dipole direction and $\mathbf{E}(r_p)$ and $\mathbf{E}_0(r_p)$ are the local electric field at the dipole location r_p respectively with and without the microsphere (in a general manner, the script 0 refers to the radiation properties in free space). η is the quantum yield of the relaxation process defined as:

$$\eta = \frac{\Gamma_{\text{rad}}/\Gamma_0}{(\Gamma_{\text{tot}}/\Gamma_0 + (1-\eta_i)/\eta_i)} \tag{6.2}$$

where η_i represents the intrinsic quantum efficiency of the emitter ($\eta_i = 1$ for a perfect emitter). The total and radiative decay rate enhancements are obtained with the respective emitted and radiated power in the presence of the antenna normalized by the power in the homogeneous background medium:

$$\frac{\Gamma_{\text{tot}}}{\Gamma_0} = \frac{P_{\text{tot}}}{P_0} \tag{6.3}$$

$$\frac{\Gamma_{\text{rad}}}{\Gamma_0} = \frac{P_{\text{rad}}}{P_0} \tag{6.4}$$

The quantum yield (or quantum efficiency) is of crucial importance for light emission since it represents the ratio between the power radiated by the emitter with respect to the total emitted power. The lost energy is dissipated in the structure and is associated to an increase of the temperature of the system and may spoil further the emission properties. From Eq. (6.2), one can notice that for a perfect emitting system, the quantum efficiency can only decrease. However, it is interesting to remark that the quantum efficiency of poor quantum emitters such as quantum dots can increase if the radiative decay rates are strongly increased. Metallic nanoantennas thus allow new radiative channels to poor emitters and increase their spontaneous emission rates.

It must also be stressed that the radiative decay rate enhancements are linearly related to the excitation rate via the reciprocity theorem [99]. It results that for an incident plane wave propagating along the direction (θ, φ) via:

$$\frac{\Gamma_{\text{rad}}}{\Gamma_0}\frac{D_{col}(\theta,\varphi)}{D_{col}(\theta,\varphi)^0} = \frac{\Gamma_{exc}}{\Gamma_{exc}^0} \tag{6.5}$$

$\frac{D_{col}(\theta,\varphi)}{D_{col}(\theta,\varphi)^0}$ is the partial directivity in the direction (θ, φ) defined as [99]:

$$\frac{D_{col}(\theta,\varphi)}{D_{col}(\theta,\varphi)^0} = 4\pi\frac{\left|\mathbf{n}_p.E(r,\theta,\varphi)\right|^2}{\int_\Omega \left|\mathbf{n}_p.E(r,\theta,\varphi)\right|^2 d\Omega} \tag{6.6}$$

In most experiments, the incident beam is not a plane wave but rather a focused beam which can be defined in term of a coherent superposition of incident plane waves with different incident angles that can be included in the reciprocity theorem. Refering to Eq. (5.6) in chapter 5, one can notice that the static electric field in the vicinity of a dipolar particle is more intense in the direction of the dipolar moment. In addition, the electric field polarization is essentially directed along the induced dipolar moment. Using Eq. (6.5) and the definition of the excitation rate enhancement, it can be deduced that longitudinal interactions between the driving dipole and the induced dipole in the nanoparticle lead to high enhancements of the radiative decay rate. In contrast, as it will be demonstrated later, transverse interactions enable an interesting redistribution of the light radiated by a dipolar emitter. In that configuration, the partial directivity will tend to unity combined with a moderate excitation rate leading to weak radiative decay rate enhancements.

6.2.1 Radiative decay rates and quantum efficiency

The single emitter is simulated as a point-like dipolar source modeled by taking the first electric term in a multipole (Mie) expansion. The generalized Lorentz-Mie calculations are performed with a truncation order of $N = 20$ for the individual scatterers. The total emitted power P_{tot} and the radiative emitted power P_{rad} can be numerically calculated by integrating the radial component of the Poynting vector over a spherical surface surrounding the source at respectively small and long distances. However, in our study, the emitter and total decay rate enhancements will be calculated in the multipolar framework using the expansion of the Green function on the VSWs (detailed in Appendix C).

We first consider a dipole oriented perpendicularly to the surface of particle as displayed in Fig. 6.1(a). The influence of the distance of the dipolar emitter with respect to the plasmonic nanoparticle on the spontaneous emission efficiency has been displayed in Fig. 6.1(b), (c) in the case of a so-called longitudinal interaction. Fig. 6.1 shows the spectral dependence of (b) the quantum yield and (c) the radiative decay rates for $d = 10$ nm (full line), $d = 5$ nm (dashed line) and (c) $d = 2$ nm (dotted line) for a 60 nm diameter silver nanoparticle embedded in a $n_b = 1.5$ surrounding medium.

Whatever the distance considered, the radiative decay rate enhancement plots show a peak at the same frequency. It can be deduced that a plasmon resonance has been excited in the nanoparticle that produces this peak. Similarly to chapter 5, one can consider in a first approximation that the dipolar moment induced in the nanoparticle occurs colinearly to the driving dipole orientation. It can be easily demonstrated (similarly to the phenomenon observed in chapter 5) that an in-phase mode has been excited leading to an increasing of the initial dipolar moment and enhancing the radiative emission. When gradually decreasing the separation distance, the radiative decay rate enhancements increase of several orders of magnitude. However, the radiative decay rates enhancement is useless if the quantum efficiency is weak. One can remark that the quantum efficiency plotted in Fig. 6.1 exhibits a maximum value approximatively at the plasmon resonance. However, for separation distances smaller than $d = 5$ nm, the quantum efficiency drops below 50 % reaching only 10 % for a distance of $d = 2$ nm. As the fluorescence emission rate is defined as the product between the quantum efficiency and the radiative decay rate, one can realize that when the dipole is too close from the sphere surface, the fluorescence emission rate tends to zero giving

rise to so-called quenching effect [89]: most of the emitted power by the dipolar active source is coupled to non-radiative channels and the far field signal vanishes.

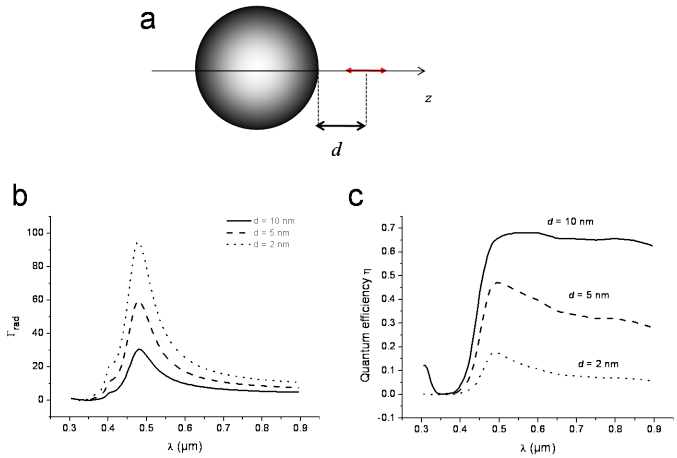

Figure 6.1: (a) Layout of the longitudinal interaction between the emitting dipole and the induced polarization moment inside the particle. The arrow designates the orientation of the driving dipole. (b) Radiative decay rate enhancement and (c) quantum efficiency of the spontaneous emission for different separation distances d: d = 10 nm (full line), d = 5 nm (dashed line), d = 2 nm (dotted line) as a function of the emission wavelength.

The transverse interactions (the layout is displayed in Fig. 6.2(a)) lead to different emitting properties of the dipolar spontaneous emission. The radiative decay rate enhancement also exhibits a peak at the plasmon frequency (equal to the frequency observed in Fig. 6.1(a)) but its amplitude is on the order of unity. The transverse interaction does not provide any enhancements of the radiative decay and the associated quantum efficiency displayed in Fig. 6.2(b) is extremelly weak (below 0.5 even for seperations d = 10 nm)

Both the quantum efficiency and the radiative decay rates are extremely different according to the dipole orientation. Transverse interactions induce weak quantum yields and radiative decay rates. In contrast, longitudinal interactions produce high enhancements of the radiative decay rates. It must also be noticed that the 2 configurations, quantum efficiency drops for wavelength between 300 nm and 400 nm. This was attributed to couplings to the interface plasmon mode of the antenna [92, 101] while radiative decay are associated with the excitation of a dipolar mode in the nanoparticle. Furthermore, the quantum yield remains limited over the entire frequency range when the distance is reduced to several nanometers. We pay now a particular attention on transverse interactions which will exhibit great abilities to modify the direction of propagation of the radiated field.

6.2.2 Emission patterns of single emitters interacting with metallic particles

The ability of nanoantennas to control the angular emission of single molecules has recently been investigated [96, 102, 103]. This possibility is particularly important since a high directivity facilitates both the excitation of a quantum emitter by a collimated beam as well as the collection of the

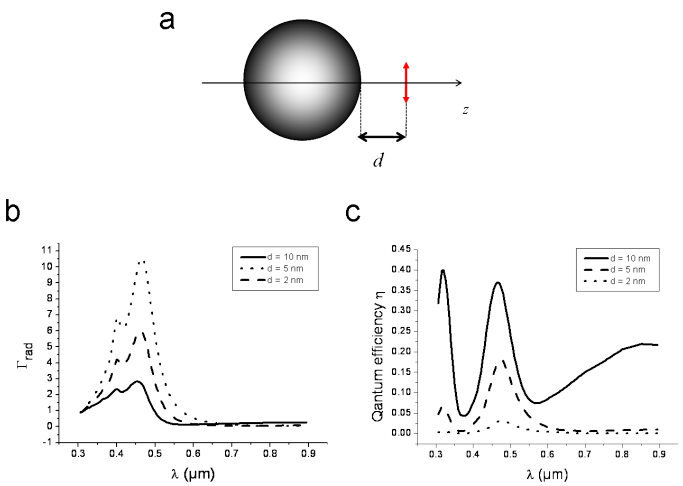

Figure 6.2: (a) Layout of the transverse interaction between the emitting dipole and the induced polarization moment inside the particle. The arrow refers to the orientation of the driving dipole. (b) Radiative decay rate enhancement and (c) quantum efficiency of the spontaneous emission for different separation distances d: $d = 10$ nm (full line), $d = 5$ nm (dashed line), $d = 2$ nm (dotted line) as a function of the emission wavelength.

radiated light [11].

It has been demonstrated that nanoparticles could either act as reflector or director elements **??**. This latter property has been related to the phase of the dipolar polarizability of the particle which is equal to $\pi/2$ at the plasmon resonance. By tailoring the polarizability of the particle and by the way the spectral position of the plasmon resonance, one can then control the reflective or a directive behavior of the particle at a given driving frequency. The particle polarizability is generally controlled by tuning the size of the nanoparticles or the thickness of nanoshells [104, 105].

A dipolar emitter can be coupled longitudinally to the antenna by utilizing a nanoparticle located near the reflector element [106]. In this configuration, the emitter is off-axis. For an on-axis emitter, the weak transverse coupling with the chain of particles can be reinforced by employing the so-called 'super emitter 'consisting of a dimer of nanoparticles perpendicular to chain axis [88, 100]. Pakizeh et al. have recently proposed an ultracompact antenna made of two identical metallic particles [106]. The dipolar emitter can be coupled to a dark mode characterized by opposite phase dipolar modes induced in the two neighboring particles. In that case, it has been shown that the emitter radiates predominantly in only one half space and can thus be characterized as unidirectional.

This section is dedicated to studying how nearby spherical nanoparticles modify the angular distribution of light emitted by an oscillating dipole. In particular, we provide a thorough study of the phase differences between the dipolar source and the dipolar mode induced in the particle. We emphasize that these phase differences must take into account the optical path between the emitter and the particle in addition to the polarizability of the particle. We show that by tuning the position of a single emitter from a single nanoparticle by a few tens of nanometers, we can sufficiently modify the dephasing to control the reflective or collective properties of the particle at a given

frequency. When the phase difference between the exciting and induced dipoles is strictly equal to π, an equal part of the energy is radiated into each of the half spaces surrounding the emitter (the separation plane being perpendicular to the axis containing the dipoles). We then apply these results to the design of highly unidirectional antennas composed of two nanospheres separated by a mere 50 or 60 nm. The basic concept is similar to the idea underlying the design of Yagi-Uda optical antennas, which associate the collective and reflective properties of nanoparticles [104, 105], but at much smaller interparticle distances and in simpler geometries. Taking into account the phase lag induced by the distance between the emitter and the nanoparticle, highly directional antennas can be designed with only two nanoparticles. We will first emphasize the role of the distance between the emitter and the nanoparticles by designing a directional antenna composed of identical particles, *i.e.* with strictly identical polarizabilities. Furthermore, by tuning the relative size of the two particles, it is possible to design an antenna smaller than $\lambda_0/2$ that channels light radiated by a single emitter in the angular aperture of commercial microscope objectives [10].

6.2.3 Radiation properties of a dipolar emitter coupled to a single nanoparticle

We first investigate the radiation pattern of a single emitter located near a single 90 nm silver particle. The dipolar emitter is polarized along the z-axis in order to provide a transverse coupling with the nanoparticle as sketched in Fig. 6.3. The emission properties of the dipolar emitter are calculated in the framework of rigorous Lorentz-Mie theory, and combined with multiple scattering theory in configurations where more than one silver particle is present [1, 107, 108]. This analytical method is particularly well suited to tackle light scattering by an ensemble of nanospheres. In order to insure an accurate modeling of the short range couplings, the calculations presented in this study are carried out with 30 multipole orders. Nevertheless, let us emphasize that the electromagnetic response of the metallic particles under consideration is predominately dipolar in nature, resulting in a rapid multipole convergence. Consequently, a dipole approximation (1st order) would qualitatively exhibit all the underlying physics observed in this work.

The radiation patterns are obtained from the radial component of the Poynting vector in the far field. In order to estimate how much light is collected or reflected by the metallic particle, we define the reflection coefficient R as the ratio of the power emitted in the $x \geq 0$ hemisphere with respect to the total radiated power.

In this section, we pay particular attention to the dephasing between the emitting and induced dipoles. When the dipole approximation dominates (as it does here), it is sufficient to calculate the (nearly constant) electric field anywhere inside the metallic particle. The induced dipole moment of the nanoparticle is then obtained by multiplying the total electric field by $V_s\varepsilon_0(\varepsilon_s - \varepsilon_b)$ where V_s is the volume of the sphere, ε_0 the permittivity of vacuum and ε_s and ε_b are the relative permittivities of the metal and the background media respectively. For small particles, the quasi-static approximation applies and we can express the resulting phase differences as the sum of the phase differences due to the optical path difference field from the emitter and the polarizability of the particle. It must be stressed that in previous works, attention was focused on the phase difference of a nanoparticle polarizability with respect to its local excitation fields, while we emphasize importance of taking

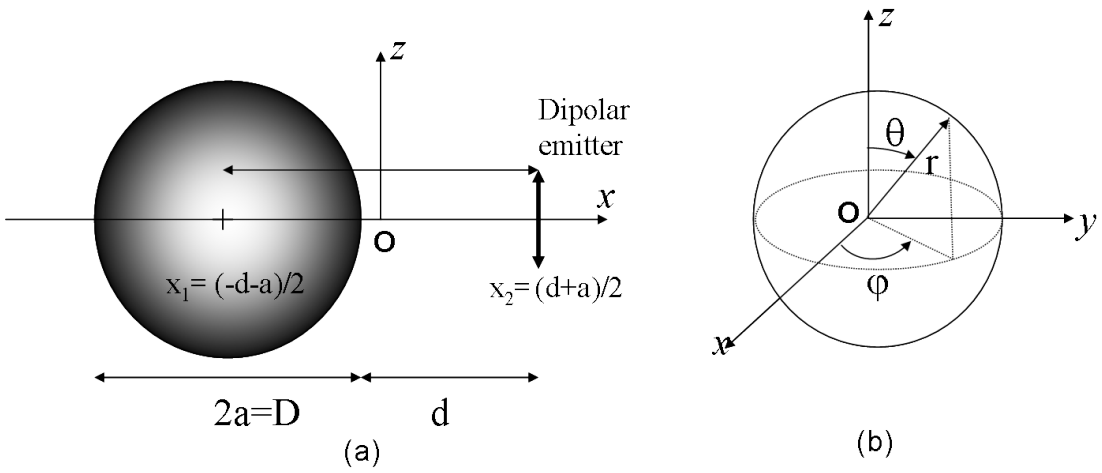

Figure 6.3: (a) Sketch of a dipolar emitter oriented along the z-axis and located at a distance d from the surface of a silver nanosphere. The refractive index of silver is taken from Ref. [69]. Silver nanospheres are embedded in a polymer of refractive index 1.5. (b) The spherical coordinates used in the analytical expressions.

into account the additional phase difference induced by the (small but non-negligible) optical path between the emitter and the nanoparticle. We point out that we chose the common convention of the phase differences defined to lie in the range from $-\pi$ to π.

The phase differences $\Delta\phi$ between the emitter and dipole moment of a (D = 90 nm) silver nanoparticle are displayed in Fig. 6.4 (circles) as a function of the emission wavelength. The emitting and induced dipoles are precisely in opposing phase at λ_r = 600 nm, $\Delta\phi = \pi$, and remain roughly in opposite phase for longer wavelengths. For wavelengths smaller than λ_r = 600 nm, $\Delta\phi$ varies as a function of λ_0, and the induced dipole is generally out-of-phase with respect to the emitter. The phase of the polarizability of the nanoparticle is also displayed (squares) and the phase value of $\pi/2$ at λ_0 = 500 nm indicates the plasmon resonance. Let us now investigate the radiation properties of the coupled system in terms of the reflection efficiency of the nanosphere. We present in Fig. 6.4 the reflection efficiency, R, of the nanoparticle (*i.e.* defined as the power emitted in the $x \geq 0$ half space over the total emitted power) as a function of the emission wavelength λ_0. When the reflection efficiency is lower than 0.5, the dipole preferentially radiates towards the $x \leq 0$ half space and the nanoparticle behaves as a collector (c.f. Fig. 6.3: the nanoparticle is located on the negative x-axis). The full line in Fig. 6.4 clearly indicates that depending on the phase differences between the emitting and induced dipoles, a metallic nanoparticle can either collect or reflect light radiated by a single emitter. Let us mention that the dipolar approximation (triangles) exhibits almost all the features of the radiation properties, meaning that the coupling between the single emitter and the metallic particle is almost perfectly dipolar for $\lambda_0 > 450$ nm. For wavelengths $\lambda_0 > \lambda_r$, the emitting and induced dipoles are nearly opposite in phase and the emitter radiates preferentially towards the metallic nanoparticle with R dropping down to 0.4 at λ_0 = 665 nm. For $\lambda_0 < \lambda_r$, the emitting and induced dipoles are out-of-phase and the nanoparticle reflects with a

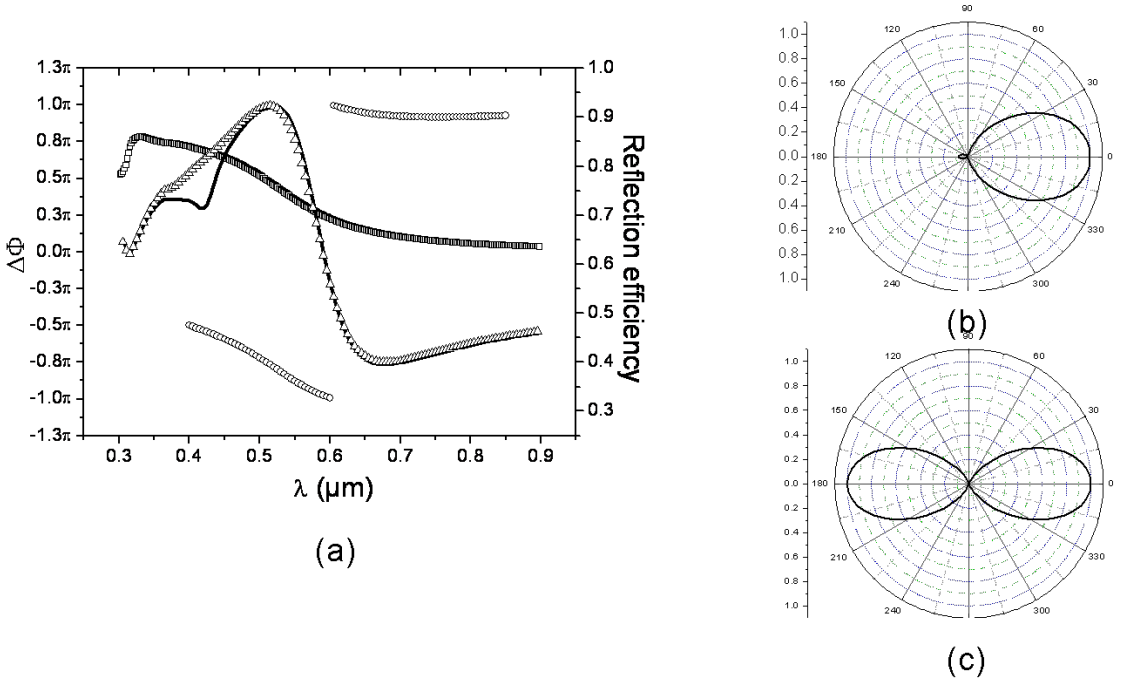

Figure 6.4: (a) A dipolar emitter oriented along the z-axis is located at a distance $d = 30$ nm from a silver sphere of diameter 90 nm. The phase difference between the emitting and induced dipoles (circles, left scale) and reflection efficiency (right scale. Full line: complete calculation, triangles: dipolar approximation) as a function of the emission wavelength. Emission patterns of the oscillating dipole at (b) $\lambda_0 = 510$ nm and (c) $\lambda_0 = 600$ nm in the xOz plane, ($d = 30$ nm) calculated by plotting the radial component of the Poynting vector normalized by the forward emitted value as a function of the polar angle.

rather high efficiency the radiated light since R reaches 90% at $\lambda_0 = 510$ nm.

The emission pattern of the light radiated by the exciting dipole at $\lambda_0 = 510$ nm is reconstructed in Fig. 6.4(b) by plotting the radial component of the Poynting vector normalized by the forward emission value as a function of the polar angle (in the plane xOz). This result demonstrates the good unidirectionality offered by a single nanoparticle. The angular width of the emission pattern defined as the angle between the on-axis maximum value and the direction of half maximum value is of the order of ±40 degrees. Finally, it is interesting to note that for $\lambda_0 = \lambda_r$, the ratio of the radiated energy in both half spaces is precisely equal to 1. It may seem surprising that a highly asymmetric environment (a single particle at the left of the emitter) results in perfectly symmetric radiation (see the radiation pattern in Fig. 6.4(c)). To fully understand this counter-intuitive result, let us consider the analytic expression of the emission of two dipoles with moments denoted $\mathbf{p}_1$ and $\mathbf{p}_2$. They are placed along the x-axis with separation $d + a$, and oriented along the z-axis (see Fig. 6.3(a)). Let us note $x_1 = -(d + a)/2$ and $x_2 = (d + a)/2$ the positions of the dipoles along the x-axis. We consider that in the far-field limit ($r \gg \lambda_0$), $|\mathbf{r} - \mathbf{x}_j| - r = \sqrt{(x - x_j)^2 + y^2 + z^2} - r \approx -x_j \sin(\theta)\cos(\varphi)$. The

electric and magnetic fields produced in the far field by $\mathbf{p}_1$ and $\mathbf{p}_2$ then write :

$$\mathbf{E}_j(r,\theta,\varphi) = \left(\frac{\omega}{c}\right)^2 \frac{1}{4\pi r\varepsilon_0} e^{ik|\mathbf{r}-\mathbf{x}_j|}[(\widehat{\mathbf{r}}\times\mathbf{p}_j)\times\widehat{\mathbf{r}}] \tag{6.7}$$

$$= \left(\frac{\omega}{c}\right)^2 \frac{1}{4\pi r\varepsilon_0} e^{ikr}e^{-ikx_j\sin(\theta)\cos(\varphi)} p_j \ \sin(\theta)(-\widehat{\boldsymbol{\theta}}) \tag{6.8}$$

$$\mathbf{H}_j(r,\theta,\varphi) = \frac{k\omega}{4\pi r} e^{ikr}e^{-ikx_j\sin(\theta)\cos(\varphi)} p_j \ \sin(\theta)(-\widehat{\boldsymbol{\varphi}}) \tag{6.9}$$

with $\widehat{\mathbf{r}}$, $\widehat{\boldsymbol{\theta}}$, and $\widehat{\boldsymbol{\varphi}}$ the unit vectors of the spherical basis (Fig. 6.3(b)). The resulting far-field, time-averaged Poynting vector of the sum of these fields writes :

$$\mathbf{P}(r,\theta,\varphi) = \frac{1}{2}\,\mathrm{Re}[(\mathbf{E}_1+\mathbf{E}_2)^*\times(\mathbf{H}_1+\mathbf{H}_2)] \tag{6.10}$$

$$= \frac{\omega^3 k}{32\pi^2\varepsilon_0 c^2 r^2}(p_1^* e^{-ikr}e^{ikx_1\sin(\theta)\cos(\varphi)} + p_2^* e^{-ikr}e^{ikx_2\sin(\theta)\cos(\varphi)}) \tag{6.11}$$

$$(p_1 e^{ikr}e^{-ikx_1\sin(\theta)\cos(\varphi)} + p_2 e^{ikr}e^{-ikx_2\sin(\theta)\cos(\varphi)})\sin^2(\theta)\,\widehat{\mathbf{r}}$$

$$= \frac{\omega^3 k}{32\pi^2\varepsilon_0 c^2 r^2}\left[|p_1|^2+|p_2|^2+2\,\mathrm{Re}(p_1 p_2^* e^{ik(d+a)\sin(\theta)\cos(\varphi)})\right]\sin^2(\theta)\,\widehat{\mathbf{r}} \tag{6.12}$$

To study the symmetry of the radiation pattern, we compute the sum of the Poynting vectors in one direction and in the opposite direction :

$$\Delta\mathbf{P}(r,\theta,\varphi) = \mathbf{P}(r,\theta,\varphi)+\mathbf{P}(r,\pi-\theta,\varphi+\pi) \tag{6.13}$$

$$= \frac{\omega^3 k}{16\pi^2\varepsilon_0 c^2 r^2}\,\mathrm{Re}\{2ip_1 p_2^*\sin[k(d+a)\sin(\theta)\cos(\varphi)]\}\sin^2(\theta)\,\widehat{\mathbf{r}} \tag{6.14}$$

In our case, we are interested by the evolution of $\Delta\mathbf{P}$ with respect to the relative phase $\phi = \phi_1 - \phi_2$ between $p_1 = |p_1|e^{i\phi_1}$ and $p_2 = |p_2|e^{i\phi_2}$:

$$\Delta\mathbf{P}(r,\theta,\varphi) = \frac{\omega^3 k}{16\pi^2\varepsilon_0 c^2 r^2}\{-2|p_1||p_2|\sin(\phi)\sin[k(d+a)\sin(\theta)\cos(\varphi)]\}\sin^2(\theta)\,\widehat{\mathbf{r}} \tag{6.15}$$

Hence when $\phi = k\pi$ with k $\in \mathbf{N}$, $\Delta\mathbf{P} = 0$ for any value of the dipolar amplitudes $|p_1|$ and $|p_2|$. This calculation demonstrates that when the emitted and induced dipoles are in phase or in opposite phase, the emission from the two dipoles is perfectly symmetric with respect to the origin, while the electromagnetic environment of the emitter can be highly asymmetric. This confirms that the wavelength of the plasmonic resonance ($\lambda_0 = 500$ nm) taken alone cannot predict the directionality of the emission and that the distance between the emitter and the nanoparticle plays a crucial role. Moreover, this model exhibits a very interesting property: in a given direction defined by θ and ϕ, the change of the sign of $\sin(\phi)$ will change the sign of $\Delta\mathbf{P}$, for every distance d. In order to confirm this assumption, phase differences (Fig. 6.5(a)) and reflection efficiencies (Fig. 6.5(b)) are now displayed as a function of distance d and λ_0.

These graphs confirm the clear correlation between reflection efficiency and the phase differences of the emitting and induced dipoles. The isoefficiency line is plotted in Fig. 6.5(b) when

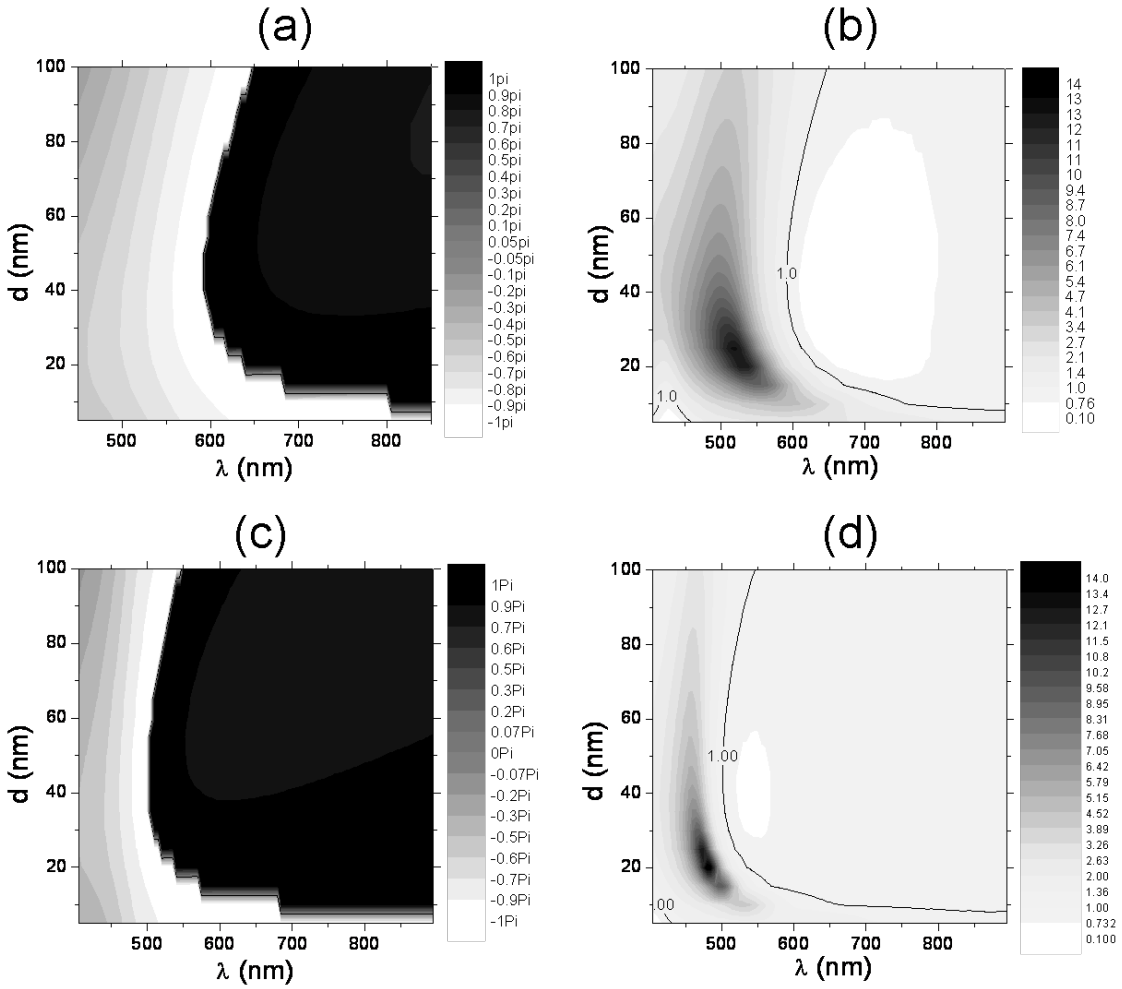

Figure 6.5: Phase differences between the dipolar emitter and the induced dipolar moment of the nanoparticle (a) and reflection efficiency (b) as a function of the wavelength of emission and the distance d between the emitter and the metallic surface of a 90 nm silver sphere. Figs. (c) and (d) show similar results as (a) and (b) respectively but for a 60 nm sphere.

the directionality is null and it matches the isodephasing line (see Fig. 6.5(a)) plotted for $\Delta\phi = \pi$. Calculations performed for a 60 nm silver particle (Fig. 6.5(c)-(d)) show that a similar behavior is obtained, but that the opposite-phase wavelength, λ_r, is shifted towards shorter wavelengths. These graphs evidence that in the 500 nm - 600 nm range (with d = 30nm), the smaller particles (60 nm) mostly collect electromagnetic radiation while larger particles (90 nm) act as reflectors. This property allows the design of Yagi Uda antennas with a reflector made of slightly larger particles and a collector made of an array of identical smaller particles [100, 104, 105, 109, 110]. More importantly, these calculations show that at a given frequency, a single sphere can act as a reflector or a collector depending on its distance from the emitter, and that this behavior can be controlled inside a very small range of distances (a few tens of nm). For example, we can observe in Fig. 6.5(d) that at λ_0 = 550 nm, the nanoparticle behaves as a collector when it is at a distance of 40 nm from the emitter while it behaves as a reflector when this distance is reduced to 10 nm. Consequently, it is

possible to design unidirectional antennas by assembling two identical particles, *i.e.* with identical polarizabilities and by tuning the distances between the emitter and both particles. However, Fig. 6.5 suggests that a stronger directionality can be achieved by assembling two particles of different diameters with minimum and maximum reflection efficiencies at the emission wavelength, property that cannot be achieved with equal diameters. We can thus design an ultracompact antenna made of 90 nm and 60 nm particles at an equal 30 nm distance from the emitter, geometry chosen to optimize the dephasing between the dipolar moments of the nanospheres and the emitter.

6.3 Ultracompact and unidirectional nanoantenna

Before discussing antennas with non equal diameters, let us begin this section by designing an ultracompact antenna composed of two identical nanoparticles of diameters 60 nm closely separated by a distance of only 50 nm. The emitter is located at 10 nm from the first particle (which thus acts as the reflector) and 40 nm from the second particle (the collector) (see Fig. 6.6a). Fig. 6.6b shows the reflection efficiency as a function of the wavelength of emission. A good directivity can thus be achieved with strictly identical particles since 70% of the emitted energy is radiated in the positive x half space. Let us note that both distances, respectively 10 nm and 40 nm are much smaller than the emitting wavelength and achievable with biological linkers [65, 111].

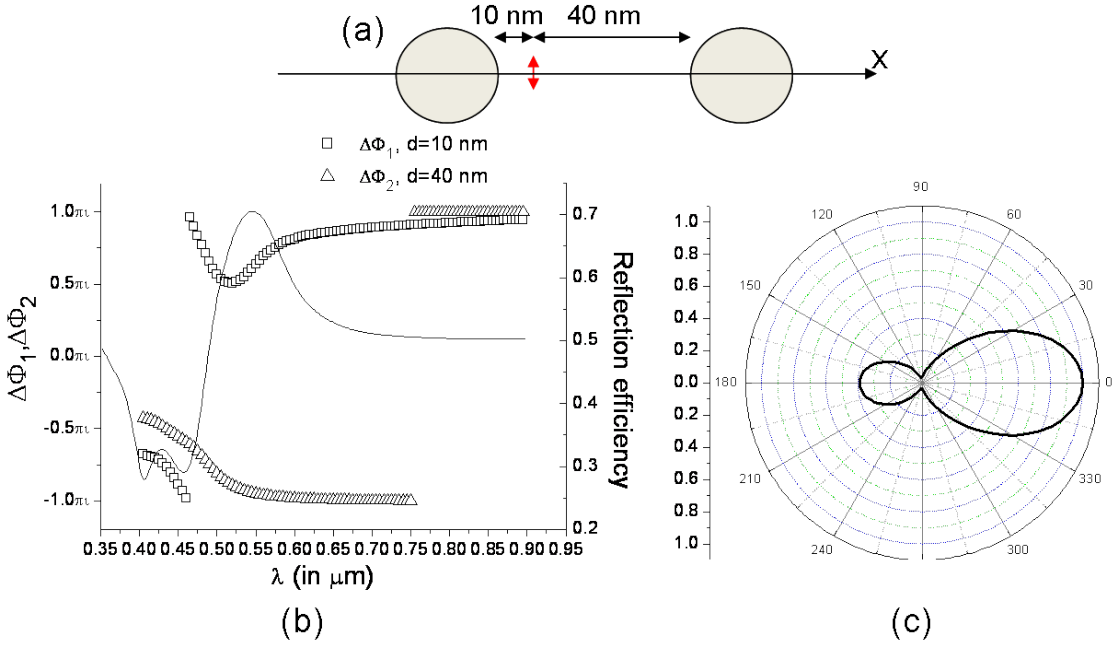

Figure 6.6: (a) The nanoantenna is composed of two identical silver nanoparticles of diameter 60 nm. The emitter is located at 10 nm from the left particle, and at 40 nm from the right particle. (b) Reflection efficiency as a function of the emitted wavelength. (c) Emission pattern of the oscillating dipole at $\lambda_0 = 550$ nm in the xOz plane.

Let us now design an asymmetric antenna made of two silver particles with different diameters to optimize their reflective and collective properties. The antenna, consisting of 60 nm and 90 nm

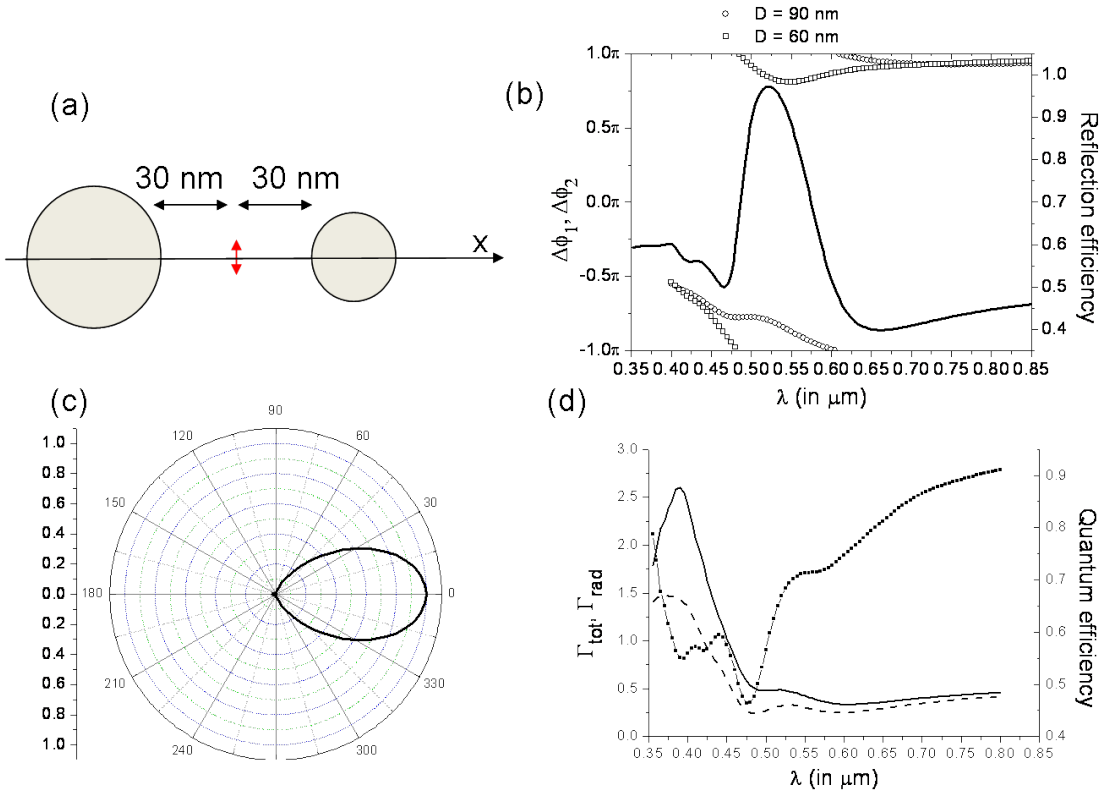

Figure 6.7: (a) The nanoantenna is composed of silver particles of diameter 60 nm and 90 nm. The emitter is located at 30 nm from both particles. (b) Full line, right scale: Reflection efficiency as a function of the emitted wavelength; Dotted and dashed lines, left scale: dephasing of the emitting and induced dipoles supported by spheres of diameter 90 nm (dashed line) and 60 nm (dotted line). (c) Emission pattern of the oscillating dipole at λ_0 =550 nm in the xOz plane. (d) Full and dashed lines, left scale: radiative (dashed line) and total (full line) decay rates enhancements as a function of the wavelength emission. Full line+squares, right scale: quantum efficiency (the intrinsic quantum efficiency is equal to 1)

diameter silver spheres, was optimized with respect to the particle sizes while keeping d equal to 30 nm (see Fig. 6.7(a)). In a first step, we compute the phase differences between the emitter and the two induced dipolar modes supported by the particles. The wavelength range in which one particle acts as a collector while the other reflects radiation exceeds 100 nm, which is larger than the width of a typical fluorescent emitter. Fig. 6.7(b) shows that this antenna geometry fulfills these conditions for wavelengths ranging from 475 nm to 600 nm. As expected, the ratio of the radiated power towards the $x \geq 0$ half space is maximum when the phases are of opposite sign, and it can reach more than 97% at λ_0 = 520 nm. The emission pattern is reconstructed in Fig. 6.7(c) at λ_0 = 520 nm as a function of the polar angle (in the plane xOz). It confirms the high unidirectionality of this antenna since the emitted power towards the left half plane is unobservable at this scale. Moreover, this antenna narrows the angular redistribution of emitted light compared to a single nanoparticle since the angular width of the emission cone is less than ±30 degrees. Such angular openings are easily achievable with commercial microscope objectives [112]. In practice, this

asymmetric nanoantenna, although much smaller than the vacuum emission wavelength of the oscillating dipole, is almost perfectly unidirectional.

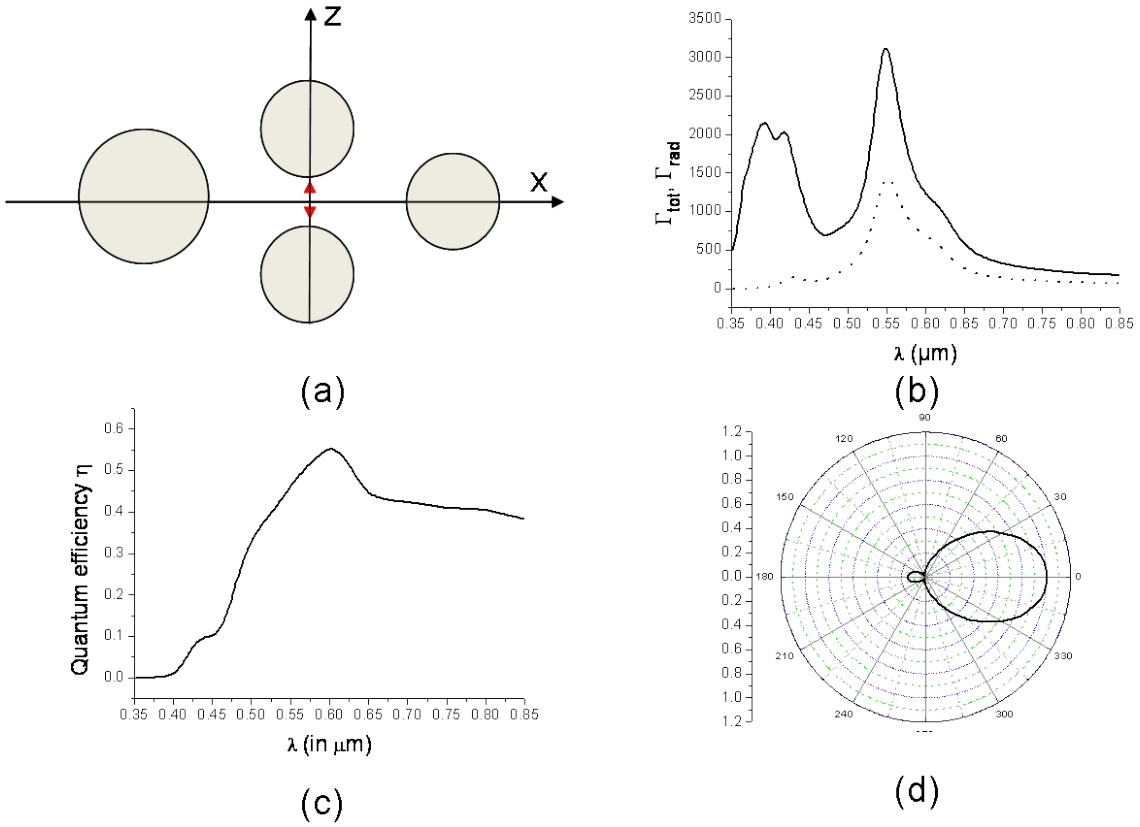

Figure 6.8: (a) Sketch of the ultracompact nanoantenna + super emitter: the dipolar source is longitudinally coupled with two 60 nm silver particles on the z axis, with an emitter-particle distance of 8 nm. The emitter-particle distances on the x axis are equal to Fig. 6.7(a) at 30 nm. (b) Radiative and total decay rate enhancements as a function of the emission wavelength. (c) Quantum efficiency as a function of the emission wavelength. (d) Emission pattern of the oscillating dipole at λ_0 =610 nm in the xOz plane.

For the sake of completeness, the evolution of the radiative and total decay rates and the quantum efficiency of the emitter in the vicinity of the optical antenna are displayed in Fig. 6.7(d). For that purpose, the total emitted power, P_{tot}, and the radiated power, P, are calculated by integrating the radial component of the Poynting vector over a spherical surface surrounding the source, at respective distances of 1 nm and 50 μm. The total (Γ_{tot}) and radiative (Γ_{rad}) decay rate enhancements are then obtained by normalizing the emitted power in the presence of the antenna by the emitted power (P_0) in the homogeneous background medium: $\Gamma_{\text{tot}} = P_{\text{tot}}/P_0$ and $\Gamma_{\text{rad}} = P_{\text{rad}}/P_0$. The quantum efficiency is then defined as $\eta = \Gamma_{\text{rad}}/(\Gamma_{\text{tot}} + (1-\eta_i)/\eta_i)$ where η_i is the intrinsic quantum efficiency. We consider a perfect emitter ($\eta_i = 1$). Fig. 6.7(d) shows that the high directionality achieved at $\lambda_0 = 520$ nm is not associated with a drop of the radiative decay rates which confirms that it relies on the association of the reflective and collective features of nanoparticles rather than on opposing phases between the induced dipoles of the nanoparticles [10, 106]. The

radiative decay rates obtained are comparable with those observed when dealing with Yagi-Uda antennas [100, 109] and they are significantly enhanced by coupling the source dipole to a "super-emitter" as shown in Fig. 6.8(a). In this last case, we consider a more complex antenna geometry to combine unidirectionality and strong radiative rate enhancements by introducing two dipolar particles coupled longitudinally to the emitter. Fig. 6.8(b) shows that a super emitter can strongly enhance the radiative decay rates by up to 3 orders of magnitude. In particular, at λ_0 = 610 nm, the quantum yield is maximum, the radiative decay rate is enhanced by more than 500 and the unidirectionality is preserved as shown on Fig. 6.8(d).

6.4 Conclusion

The reflection or collection behavior of the nanoparticle depends on the total phase difference between the emitting and induced dipoles which includes both the polarizability of the metallic particle and the optical path between the emitter and the nanoparticle. We showed the importance of the role of the optical path between the emitter and a metallic particle on the redistribution of light for distances smaller than $\lambda_0/30$. One consequence of this observation was to remark that when the emitting and induced dipoles are exactly in opposing phase, the ratio between the radiated powers in the backward and forward directions is precisely equal to unity. We unveiled the importance of the optical path by designing a directional antenna composed of two identical nanoparticles [10]. The reflective and collective properties were tuned by controlling the distance between the emitter and the nanoparticles at a scale of $\lambda_0/10$. We also presented a means to design highly directive and ultracompact nanoantenna by tuning the relative sizes of the silver particles (while still keeping the overall size much smaller than the vacuum emission wavelength). While angular openings obtained with single plarticles are around 40 degrees, the dimer nanoantennas narrow the angular opening of emitted radiation to around 30 degrees, rendering the radiation readily collectible by commercial microscope objectives. Finally, we showed that the radiative decay rate of an emitter can be increased by three orders of magnitude by introducing a dimer antenna longitudinally coupled to the emitter while preserving a high directivity.

CHAPTER 7

Metallo dielectric nanoantennas

Contents

7.1 Introduction

Recent papers have addressed the important issue of the angular redistribution of radiated power induced by the structured local environment. A single nanoparticle can be considered as the most simple optical antenna enabling a redirection of the dipolar emission into a single half space and the addition of a second nanoparticle can further improve the directionality.

Recently, linear arrays of particles analog of the radiofrequency Yagi-Uda antenna have been successfully downscaled to the optical range to obtain high directionality of light radiation [100, 104, 109, 110, 113]. A large number of nanoparticles is employed in these structures enabling high directionality of the radiated signals but at the price of more complex structures. The design of an optical antenna based on a fully plasmonic approach remains challenging since high directionality can suffer from ohmic losses inherent to metallic structures and requires precise manufacturing techniques to align several particles. Dielectric materials have usually been disregarded in this context because their extinction cross-sections are comparable in size to their geometrical cross-sections, thus producing weak excitation rates. However, it has been demonstrated that high refractive index dielectric materials can induce a redirection of the dipolar emission [5, 114, 115]. Arrays of dielectric nanoparticles have also shown their ability to redirect light [116]. The considerable advantage of transparent (lossless) dielectric materials is that they preserve the quantum efficiency.

This work demonstrates that a judicious combination of dielectric and metallic materials can produce highly directional compact optical antennas which strongly enhance both local field excitation and radiation rate of a dipolar emitter. We will see that desirable properties occur in conjunction with a large quantum efficiency thereby ensuring a high fluorescence emission rate.

7.2 Scaling down Yagi-Uda antennas

In the radiofrequency regime, phased arrays are well known as an efficient means for inducing high directionality of emissions. The key idea consists in producing coherent oscillations of the resonant induced dipole moment of each element of the antenna producing a constructive interference pattern in the direction of interest. The scale of the elements in the radiofrequency domain allows each element to be actively driven leading to various potential antennas design.

Yagi-Uda antennas have been successfully introduced at optical frequencies [104, 105] and their high angular directivity has been confirmed experimentally [110, 113]. As illustrated in Fig. 7.1(a), Yagi-Uda antennas are typically made of three elements: (i) a feed element which can be the emitting dipole itself or a plasmonic element to couple the source to the antenna, (ii) a director element that orientates radiations in the direction of interest, and (iii) a reflector element that prevents radiations from propagating in the opposing half space.

The director elements of optical Yagi-Uda antennas consist of several aligned nanoparticles. The ability for a single metallic nanoparticle to act as a director element has been discussed in the previous chapter in the design of ultracompact plasmon-based antennas. This behavior was explained by invoking the relative phase of the induced dipolar moment in the nanoparticle with respect to the driving excitation dipole, resulting in an asymmetric radiation pattern in the far field region. It was also demonstrated however that a single nanoparticle could reflect rather than collect the dipolar radiations.

Fig. 7.1(b) displays the collection angle (defined as the half angle at half maximum) when a dipolar emitter is located at an extremity of a finite linear chain of 8 silver nanoparticles of 100 nm in diameter (dashed lines) as a function of the excitation wavelength. The plots also show the same calculations with the addition of a reflector element (full line) consisting in a single slightly larger particle (D = 120 nm). Both plots show an abrupt drop in the collection angle around λ_0 = 600 nm signifying a strong directive regime of the antenna. Since the plots with and without a reflector element are nearly identical, it can be deduced that the directivity is almost entirely provided by the linear array of particles. These plots do not reveal the total emitted power in the direction of interest. The radiation pattern of a dipolar emitter oscillating at λ_0 = 650 nm, enclosed in the Yagi-Uda antenna is displayed in Fig. 7.1(c) demonstrating that the power emitted is mostly radiated in the direction of the interest with almost no light propagating in the opposite direction. It must be stressed that the radiation pattern with and without the reflector element are both displayed in Fig. 7.1(c) and are almost identical. One can thus wonder what are the subsequent benefits of using an additional particle as a reflector element, particularly considering that this particle can further spoil the spontaneous emission rate.

Fig. 7.2(a), (b) and (c) display respectively the radiative decay rate enhancements, (b) quantum efficiency and (c) angular openings for a Yagi-Uda antenna consisting of eight spherical nanoparticles as the director element. The radiative decay rates (Fig. 7.2(a)) remains below unity over the whole optical frequency range. In addition, a drop in the quantum efficiency is clearly observed in Fig. 7.2(b) when the directivity (Fig. 7.2(c)) is maximal. These plots show that the addition of the reflector element (full line) reduces both the radiative decay rates and the quantum efficiency without providing any benefits on the directionality. It can be concluded that the linear chain of nanoparticles is sufficient to collect light emission and the additional reflector element is not nec-

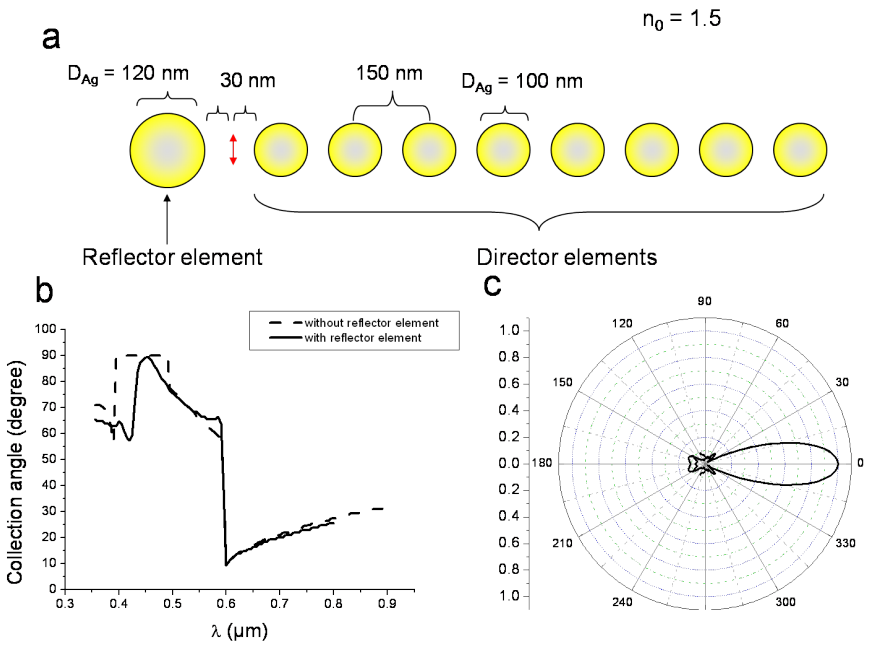

Figure 7.1: (a) Schematic of the Yagi-Uda antenna. An oscillating dipole is located in a linear chain of eight gold nanoparticles. (b) Collection angle of the antenna as the function of the oscillating wavelength. The collection angle is defined as the half angular width at half maximum. (c) Radiation pattern of the antenna at λ_0 = 650 nm.

essary in the optical domain. Nevertheless, it is rather unfortunate that decay rates and quantum efficiency are weak in all basic Yagi-Uda configurations.

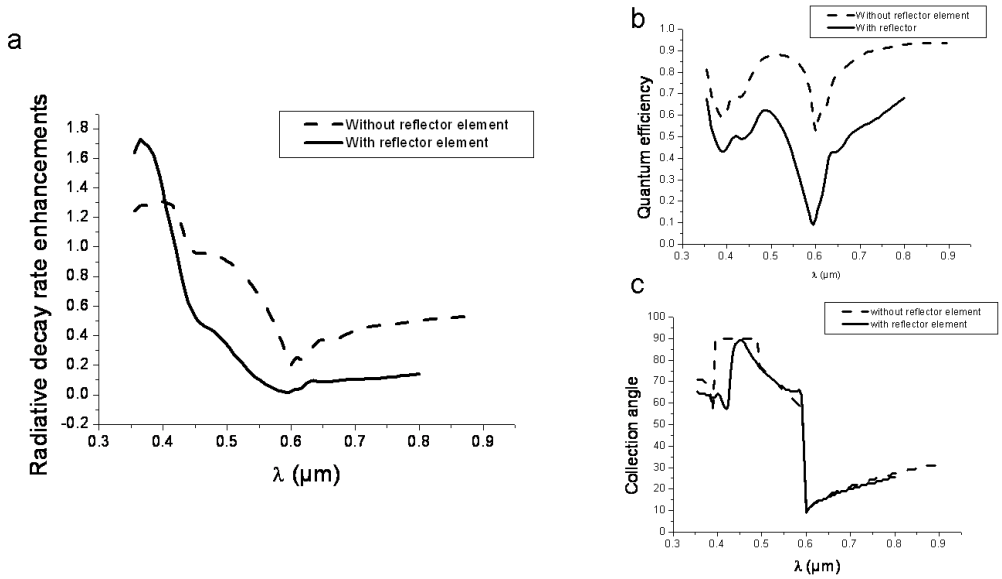

Figure 7.2: (a) Radiative decay rate enhancement, (b) quantum efficiency and (c) angular openings of the Yagi-Uda antenna with (solid lines) and without (dashed lines) the reflector element.

The dipolar moments of each particle displayed in Fig. 7.3, show that successive dipole induced moments oscillate transversally with respect to the chain axis with opposing phase between successive particles. This configuration reduces significantly the spontaneous decay rates, but enables the propagation of a guided mode in the linear chain. Linear chains of nanoparticles were previously investigated as waveguiding arrays to transport optical electromagnetic signals over large distances [117, 118]. For specific illumination wavevectors, one-dimensional arrays can support guided plasmon modes mediated by coherent dipole couplings between the resonant particles. Elements of plasmonic linear chains are passive so that the dipolar moment is induced in each particle by the couplings between the resonant elements. Consequently, the operating wavelength of the antenna (i.e. the spectral position of the guided mode) depends directly on the resonant propagative modes of the array and in this manner on the dispersion relation of this optical waveguide [75, 100, 119]. The guided mode hinders light couplings to the far field domain and has been proposed as a single plasmon source [100]. To efficiently radiate to the far field domain, the linear arrays must operate at slightly lower frequencies where a trade-off can be found between high directivity and acceptable quantum efficiency.

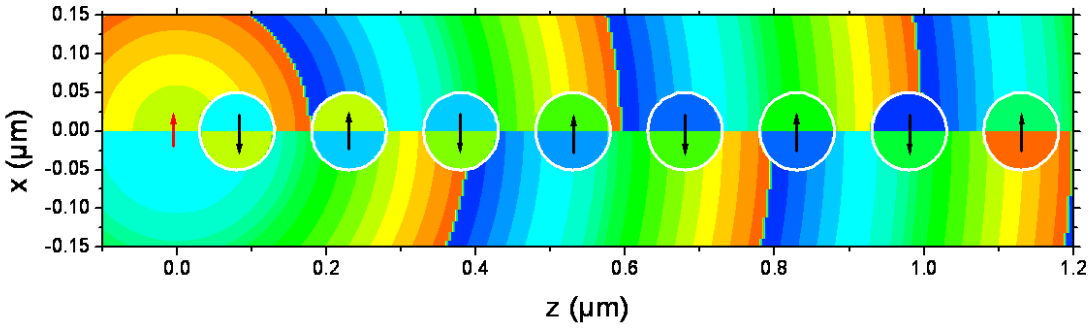

Figure 7.3: (a) phase of the dipolar induced moment in the antenna at $\lambda_0 = 600nm$.

To provide high radiative enhancements, a solution could consist in adding a feeder particle. It can be judicious to employ an elongated particle such as a plasmonic rod or a pair of coupled particles [88, 100] that have may exhibit larger resonances and fulfill this role.

It must be stressed that to obtain high directivity, the typical length of Yagi-Uda optical antenna have to be on the order of the wavelength. Thus, plasmonic antennas do not provide as much scale reduction as hoped for when employing metallic nanoparticles. Furthermore, the design of Yagi-Uda antenna requires challenging nanofabrication techniques since several nanoparticles have to be accurately aligned and the fabrication of such as antenna has only been recently performed with a reduced number of nanoparticles [110, 113]. In addition to a complex structure, the antenna operate in the substrate plane so that the radiated field may be useful for integrated optics or energy transport but may be difficult to observe from the far field.

For these reasons, dielectric materials may be more appropriate in the design of highly directive antennas with acceptable decay rates. We have recently proposed the use of a high refractive index dielectric microsphere to replace the multiple particle director. Due to the high refractive index of TiO_2, a high directivity can be achieved with a 500 nm diameter sphere.

7.3 Metallo dielectric nanoantennas

The schematic of the antenna being considered is displayed in Fig. 7.4(a). The optical antenna consists of a TiO_2 dielectric microsphere [115, 120] (D = 500 nm) and two silver nanospheres (D = 60 nm separated by 8 nm) embedded in a dielectric background of refractive index n_b = 1.3. A dipolar-like source oriented along the x-axis is placed 30 nm from the dielectric microsphere and centered equidistantly along the axis joining the silver spheres.

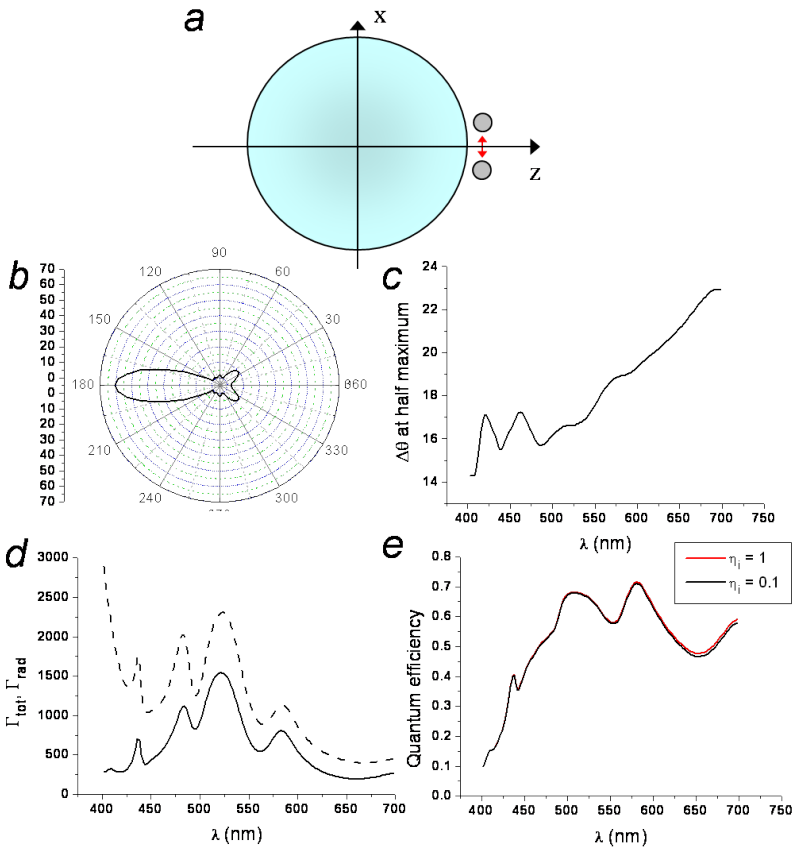

Figure 7.4: a) Antenna schematic: a dielectric microsphere (D = 500 nm, $n_{\mathrm{Tio_2}}$ taken from Ref. [120]) and two silver nanoparticles separated by 8 nm (D = 60 nm and n_{Ag} taken from Palik [69]) are embedded in a dielectric background of refractive index n_b = 1.3. A dipolar emitter is placed equidistantly from the silver spheres along their axis of separation. b) Radiation diagram at λ_0 = 525 nm, c) collection angle (3db half width), d) total (dashed line) and radiative (full line) decay rate enhancements and e) quantum efficiency for a perfect emitter (red line) and a poor emitter, η_i = 0.1 (black line).

Fig. 7.4(b) displays the radiation pattern of the antenna (polar plot of the radiated power per angle unit) for a dipole oscillating at λ_0 = 525 nm (λ_0 is the wavelength in vacuum). Contrary to free space radiation, Fig. 7.4(b) exhibits a highly directional emission with an angular aperture (3dB half-width) $\simeq$ 15°. Calculations displayed in Fig. 7.4(c) show that the collection angle remains below 25° for a wavelength range from 400 nm to 700 nm. More interestingly, this highly

directive radiation is concurrent with a strong enhancement of the radiative decay rate. The radiative decay rate enhancement (full line) displayed in Fig. 7.4(d) surpasses two orders of magnitude over the entire optical frequency range. Moreover, the spectral feature of Γ_{rad} shows several peaks higher than 10^3 revealing electromagnetic structural resonances that will be attributed later to the excitation of cavity resonances occuring in the high refractive index microsphere. In other words, this optical antenna does not require an optimization of the electromagnetic resonances in order to be efficient, but an optimization of the electromagnetic couplings between the dipolar emitter and electromagnetic resonances permits radiative decay factors Γ_{rad} as high as 10^3. The high quality of the antenna is confirmed in Fig. 7.4(e) which shows a quantum efficiency greater than 0.5 for $\lambda_0 > 450$ nm. Even more spectacularly, we remark that the quantum efficiency of a poor emitter (black line in Fig. 7.4(e)) is essentially the same as the quantum efficiency of a perfect emitter (red line). Further calculations show that this property is fulfilled for any intrinsic quantum efficiency higher than 10^{-3}. This behavior is mainly due to the giant decay rates enhancements which render the term $(1-\eta_i)/\eta_i$ in 6.2 negligible compared to Γ_{tot}.

In summary, this simple and compact system turns out to be a highly performant antenna over the entire optical spectrum and is characterized by a high directionality, strong decay rate enhancements, and a high quantum efficiency. In the remainder of this work, we investigate the properties of the dielectric and metallic components separately in order to better understand the unique performance of this optical antenna.

7.3.1 High refractive index dielectric microsphere

We first investigate the properties of a single high refractive index dielectric microsphere. Recent studies have demonstrated that dielectric microspheres operate as efficient near field "lenses" with performances comparable to the state of art of high numerical aperture microscopes such as immersion lenses [5–7, 115, 121]. Fig. 7.5(b) displays the angular 3dB half width of the emerging propagative beam produced by a dipole located at 30 nm from the sphere surface (the dipole is oriented along the x-axis). It clearly demonstrates that a single TiO_2 microsphere 500 nm in diameter can redirect dipolar radiated power into a narrow beam of 3dB half width below 25° over a large frequency bandwidth covering almost all the optical range. Furthermore, the radiative decay rate enhancement displayed in Fig. 7.5(c) shows several peaks in the spectrum with moderated amplitudes. This behavior feature might seem surprising at first since dielectric materials generally exhibit low enhancement of the radiative decay rates. However, let us recall that the high refractive index of TiO_2 enables the well-known electromagnetic resonances in the dielectric microsphere called Whispering Gallery Modes (WGMs) [24, 30]. This assertion is clearly demonstrated in Fig. 7.5(d) which displays the electric field intensity in the vicinity of a dielectric microsphere dipole illuminated at $\lambda_0 = 440$ nm corresponding to the narrowest peak in Fig. 7.5(c). Furthermore, the far-field radiation pattern of emitted light at $\lambda_0 = 440$ nm (displayed in 7.5(e)) demonstrates that the excitation of WGMs does not significantly deteriorate the strong directional properties of the TiO_2 microsphere illuminated by a dipole. The WGM resonances do however have the ability to slightly enhance the radiative decay rates of a dipolar emitter. In summary, high refractive dielectric spheres can serve as simple and compact optical antennas in a very wide range of frequencies. Nevertheless, the huge decay rates enhancements observed in Fig. 7.4(d) cannot be

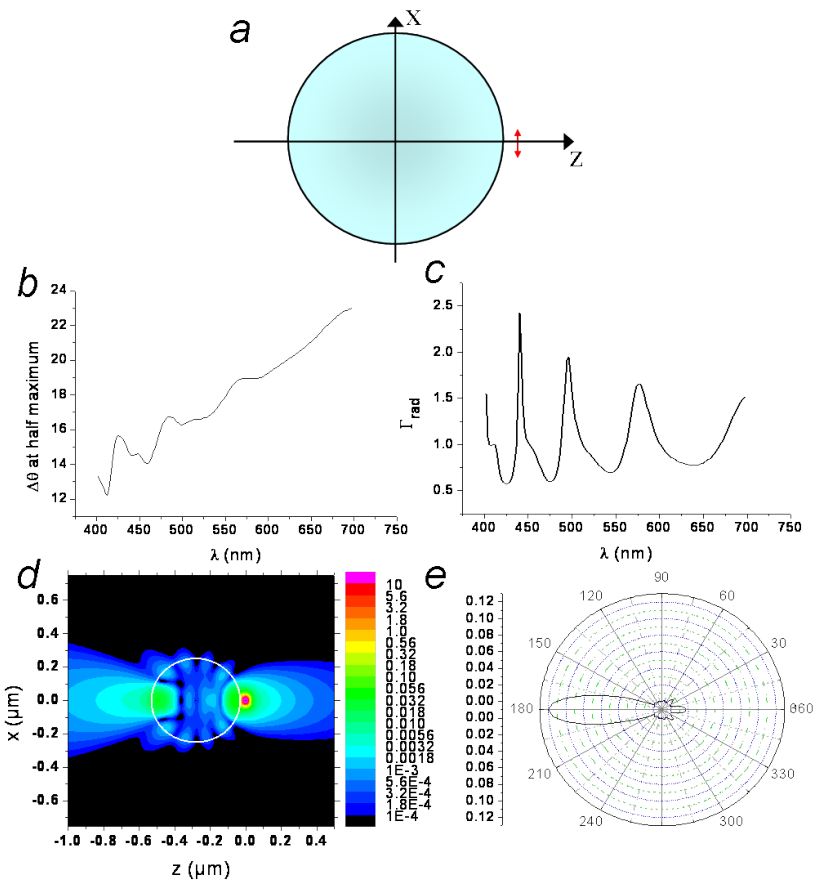

Figure 7.5: Characterization of a TiO_2 microsphere as an optical antenna. a) The microsphere is embedded in a background medium of refractive index index $n_b = 1.3$. The refractive index of TiO_2 is taken from Ref. [120]. b) collection angle (3db half width), c) radiative decay rate, d) quantum efficiency as a function of the wavelength and e) radiation diagram at $\lambda_0 = 440\ nm$.

explained by the coupling of a dipolar emitter with WGMs resonances. One concludes therefore that the bulk of the decay rate enhancements of the metallo-dielectric antenna is due to the metallic materials in the near field of the emitting dipole.

7.3.2 Enhancing spontaneous emission

Coupled nanoparticles have been widely studied in the context of nanodimers [87, 94] and bowtie nanoantennas [66, 86] to enhance the radiative decay rate of a single emitter. Fig. 7.6(b) displays the total (dashed line) and radiative (full line) decay rate enhancements when a dipole oriented along the x-axis is set in the center of the cavity formed by two silver nanoparticles 60 nm in diameter separated by 8 nm. A broad peak appears corresponding to the well-known red-shifted plasmon resonance of two coupled metallic particles [59]. Comparison between Fig. 7.4(c) and Fig. 7.5(b) shows that the so-called superemitter [88] does not significantly modify the radiation directionality when it is combined with a microsphere. As illustrated in Fig. 7.6(c), the presence of

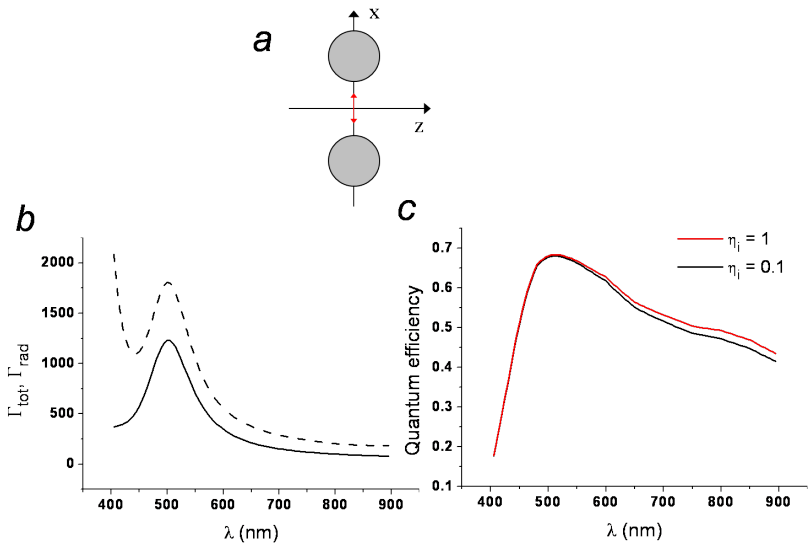

Figure 7.6: Characterization of the two silver nanoparticles (D = 60 nm) embedded in a dielectric background of refractive index n_b = 1.3. The dipolar light source is set midway between the two metallic elements separated by 8 nm and is assumed to be oriented along the separation axis. Refractive index of silver is taken from Ref. [69]. b) Total (dashed line) and radiative (full line) decay rate enhancements, c) quantum efficiency for a perfect emitter (red line) and a poor emitter, η_i = 0.1 (black line) as a function of the wavelength.

metallic losses induces a drop of the quantum efficiency of a perfect emitter (red line), particularly strong near ultraviolet frequencies. Consequently, although the efficiency of a perfect emitter is decreased due to relaxation via non radiative channels, the quantum efficiency of a poor emitter is increased several-fold (c.f. Fig. 7.6(c) with η_i = 0.1).

The design of optical antennas has been widely inspired by their analogs in the radiofrequency range, the Yagi-Uda antenna in particular [100, 104, 109, 110]. This antenna is typically made of three elements: the feed, the collector and the reflector. The feed element role is to improve couplings between the emitter and the antenna. The optical analogue of the collector generally consists of several coupled metal particles acting as a guide for plasmon waves, while the reflector can be made from a slightly larger single metallic particle. In our proposed metallo-dielectric antenna, the two coupled metallic particles act as the feed element, and the chain of guiding metallic particles and reflector are simply replaced by a single dielectric sphere. The lack of a reflector in the proposed metallo-dielectric antenna seem surprising, but it should be mentioned that optical reflector elements so far have not provided clear benefits either in the decay rate enhancements nor in the emission directionality. Moreover, as illustrated in Fig. 7.5, the dielectric collector element is sufficiently performant to channel most of the emitted power without the need for an additional element contributing to the compactness of the antenna. Let us also emphasize that the several nanofabrication techniques can potentially perform the challenging manufacturing of the proposed hybrid antenna [65, 110, 122].

For the sake of completeness, we investigate the fluorescence enhancement of a molecule located in the vicinity of the nanoantenna. The enhancement of the electric field intensity is displayed

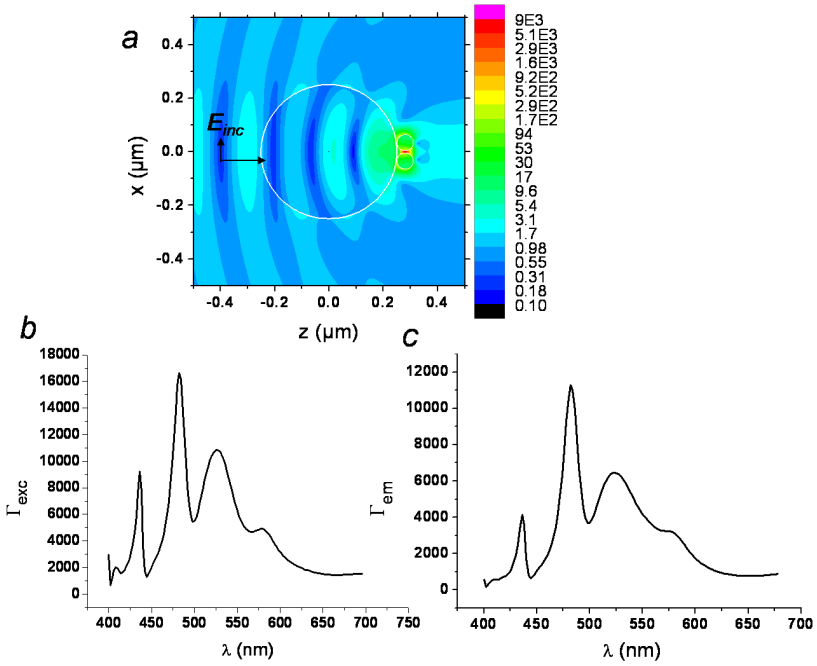

Figure 7.7: a) Colored map of the electric field intensity enhancement at $\lambda_0 = 500$ nm, b) excitation rate enhancement, c) emission rate enhancement as a function of the wavelength.

in Fig. 7.7(a) when the antenna is illuminated at $\lambda_0 = 500$ nm by a plane wave propagating along the z-axis. One observes a huge enhancement of light intensity in a nanometer sized volume delimited by the metallic spheres due to the combination of light focusing by the dielectric spheres with the excitation of coupled plasmons in the metallic dimer. This result was expected from Fig. 7.4(d) and reciprocity [101, 123] between the excitation and the radiative decay rates. Fig. 7.7(b) displays very high excitation rates that can be strengthened by the excitation of WGM. This result stems from the high extinction cross section of the dielectric sphere, 10 times greater than the extinction cross section of the dimmer of metallic nanoparticles at the plasmon resonance frequency. Consequently, this antenna presents all the required properties for single molecular detection since both Γ_{exc}, and η are highly enhanced and concurrent with a high directivity. This supposition is confirmed by a calculation of the fluorescence rate enhancement displayed in Fig. 7.7(c) as a function of the excitation wavelength λ_0, where the excitation rates and quantum efficiencies are calculated with a wavelength shift of 20 nm, representative of common fluorophores, and Alexa dye in particular. One observes that fluorescence enhancements as high as 10^4 are achieved.

This study demonstrates that appropriately designed metallo-dielectric systems can serve as compact, highly directive and ultra radiative antennas. Let us emphasize that contrary to fully metallic antennas, the high directivity of this antenna does not result from a plasmonic effect, and that it is efficient over a wide range of frequencies. In consequence, the high directivity does compromise the high radiative decay rate enhancement offered by two coupled metallic particles and it is possible to exploit whispering gallery modes to further enhance the radiative decay rates. This work paves the way towards the design of compact, simple and highly efficient optical antennas.

7.4 Conclusion

Highly directive optical antennas have been investigated in this chapter. The design of these antennas has resulted from two differents strategies. Linear chains of nanoparticles have been recently proposed as optical analogue of antennas operating in radiofrequency domain. These fully plasmonic antennas are highly directive but suffer from an intrinsec drop of the quantum efficiency at the directional regime. Furthermore, a large number of nanoparticles is required to perform high directionality which render its implementation a challenging task. Nevertheless, the Yagi-Uda antenna is optimal for integrated optics requiring planar components since their transversal dimensions are imposed by the diameter of the particles.

Another strategy constists in using high refractive index material to channel the emitted signal in the appropriate direction and exploit whispering gallery modes to further enhance the spontaneous emission. In both antennas, a plasmonic element has been employed to strongly enhance the radiative decay rates highlighting the major role of metallic nanoparticles for designing compact and efficient optical antennas.

Chapter 8

Conclusions and perspectives

A major goal of nanosciences is to transpose macroscopic engineered systems to the nanometer scale. Advances in nanofabrication techniques have encouraged investigations of the optical properties of structures with dimensions on the order of the optical wavelength and smaller. In particular, small particles have attracted a growing interest as cost-effective optical components.

In this manuscript, particles have been mainly investigated for their ability to concentrate light in their vicinity in order to enhance and localize light/matter interactions. An important distinction was made concerning the particle materials. Focusing of light with dielectric particles requires large geometrical cross-sections to achieve field enhancements. The simple dielectric components studied here manifest a variety of properties according to the illumination beam employed. When illuminated by plane waves, elongated intense volumes can be produced near the particle surface. In contrast, 3D confinements are achieved when illuminating the same particles with highly focused beams containing highly non-paraxial components. Dielectric particles offer the advantage of being lossless and can be readily manipulated by optical tweezers. Nevertheless, light focusing is limited by diffraction effects since the propagative nature of the electromagnetic radiation remains unchanged.

Metallic particles of dimensions far smaller than the optical wavelength have, on the other hand, demonstrated their ability to focus light into sub-wavelength volumes due to the large electromagnetic cross-sections provided by the couplings of light with localized surface plasmon resonances. In particular, the coherent couplings between the individual plasmonic particles allow the excitation of in-phase modes producing enormous field enhancements in nanometers scaled volumes.

More interestingly, interactions between localized plasmon resonances have shown that mode hybridizations can occur as soon as the separation distance reaches $\lambda/10$ opening the way towards a futher downscaling of classical optical elements. Control of light localization has been evidenced in the harmonic regime at $\lambda/10$ scale with a simple plane wave illumination propagating at oblique incidence with respect to the main axis of the linear antenna. By extension, arrays of particles are promising tools for high spatial resolution imaging systems, reproducible nanopatterning templates and Raman scattering enhancements.

Furthermore, the small dimensions of the focal volumes enable interactions with unique emitters such as single fluorescent molecules or quantum dots. From reciprocity considerations, it can be understood that the strong confinement of light is readily related to large enhancements of the spontaneous emission rates. These couplings between propagating light and localized states of matter are strongly similar to macroscopic radio frequency antennas and metallic nanoparticles are consequently currently considered as optical nanoantennas.

Analogously to their radiofrequency counterparts, optical nanoantennas can be designed to redirect light radiations towards a direction of interest. It results that the enhancement of spontaneous emission rates together with high directionality of the radiated field require a judicious design of

the antenna since these two properties are associated with different types dipoleinteractions. We have proposed the design of an antenna employing not only metallic structures, but instead a judicious combination of dielectric and metallic materials. This antenna, due to its large decay rates and high directivity should be appropriate for signal propagation towards the far field domain, but could also enable strong couplings between unique emitters.

Appendix A

Multiple scattering in the multipolar framework

A.1 Multipolar representation of the multiple scattering problem

A.1.1 Excitation field applied on a scatterer

The excitation field applied on a scatterer can be expressed as the superposition of the incident field with all the fields scattered by the neighboored objects composing the system:

$$\overrightarrow{\mathbf{E}}^{(j)}_{exc}(\overrightarrow{\mathbf{r}}) \equiv \overrightarrow{\mathbf{E}}^{(j)}_{inc}(\overrightarrow{\mathbf{r}}) + \sum_{l=1,l\neq j}^{N} \overrightarrow{\mathbf{E}}^{(l)}_{diff}(\overrightarrow{\mathbf{r}}) \tag{A.1}$$

$$\overrightarrow{\mathbf{E}}^{(j)}_{exc}(\overrightarrow{\mathbf{r}}) \equiv ERg\{\mathbf{\Psi}^t(\overrightarrow{\mathbf{r}})\}a + \sum_{l=1,l\neq j}^{N} E\mathbf{\Psi}^t(\overrightarrow{\mathbf{r}}_l)f^{(l)} \tag{A.2}$$

A.1.2 Translation theorem

Translation operators can be employed to expand a single field refering to different origins.

Let M be a point of a spherical coordinate system. Let a 2^{nd} spherical coordinate system be centrered in : $\overrightarrow{\mathbf{r}}' = \overrightarrow{\mathbf{r}} - \overrightarrow{\mathbf{r}}_0$.

The translation theorem expresses the multipolar waves in the original referenciel in terms of multipolar waves centered in $\overrightarrow{\mathbf{r}}_0$:

$$\mathbf{\Psi}^t(k\overrightarrow{\mathbf{r}}) = \mathbf{\Psi}^t(k\overrightarrow{\mathbf{r}}')\mathbf{J}(k\overrightarrow{\mathbf{r}}_0) \qquad \text{si } r'>r_0 \tag{A.3}$$

$$\mathbf{\Psi}^t(k\overrightarrow{\mathbf{r}}) = Rg\{\mathbf{\Psi}^t(k\overrightarrow{\mathbf{r}}')\}\mathbf{H}(k\overrightarrow{\mathbf{r}}_0) \qquad \text{si } r'<r_0 \tag{A.4}$$

$$Rg\{\mathbf{\Psi}^t(k\overrightarrow{\mathbf{r}})\} = Rg\{\mathbf{\Psi}^t(k\overrightarrow{\mathbf{r}}')\}\mathbf{J}(k\overrightarrow{\mathbf{r}}_0) \qquad \forall|r_0| \tag{A.5}$$

with

$$\mathbf{J}(k\overrightarrow{\mathbf{r}}) \equiv Rg\{\mathbf{H}(k\overrightarrow{\mathbf{r}})\} \tag{A.6}$$

Thanks to the Translation theorem, one can write:

$$\overrightarrow{\mathbf{E}}^{(j)}_{exc}(\overrightarrow{\mathbf{r}}_j) = ERg\{\mathbf{\Psi}^t(\overrightarrow{\mathbf{r}}_j)\}\mathbf{J}^{(j,0)}a + \sum_{l=1,l\neq j}^{N} ERg\{\mathbf{\Psi}^t(\overrightarrow{\mathbf{r}}_j)\}\mathbf{H}^{(j,l)}f^{(l)} \tag{A.7}$$

A.1.3 Foldy-Lax equations of the multiple scattering

Utilizing (2.20), we obtain

$$e^{(j)} = \mathbf{J}^{(j,0)}a + \sum_{l=1,l\neq j}^{N} \mathbf{H}^{(j,l)} f^{(l)} \tag{A.8}$$

or

$$e^{(j)} = \mathbf{J}^{(j,0)}a + \sum_{l=1,l\neq j}^{N} \mathbf{H}^{(j,l)} t^{(l)} e^{(l)} \tag{A.9}$$

This Foldy-Lax type equation is a fundamental equation of the multiple scattering. This equation expresses the excitation field perceived by an object j as a function of the field scattered by the other objects or via the use of the T-matrix, as a function of the excitation fields percieved by each object of the system. If the incident field is known, one can numerically obtain the field scattered by the entire system by iteration technic.

However as soon as the incident field is modified, the solution has to be entierly recalculated. We are looking for a T-matrix of the entire sytem in order to avoid this problem.

A.1.4 T-matrix of the entire system

A.1.4.1 Foldy-Lax equation of the system

We multiply equation Eq. A.8 by $t^{(j)}$ by the left and we define the equation $\mathbf{T}^{(j)}$ so that:

$$f^{(j)} \equiv \mathbf{T}^{(j)}\mathbf{J}^{(j,0)}a \tag{A.10}$$

We get :

$$\mathbf{T}^{(j)}\mathbf{J}^{(j,0)}a = t^{(j)}\mathbf{J}^{(j,0)}a + t^{(j)} \sum_{l=1,l\neq j}^{N} \mathbf{H}^{(j,l)}\mathbf{T}^{(l)}\mathbf{J}^{(l,0)}a \tag{A.11}$$

On can notice that thanks to the presence of the translation matrix $J^{(j,0)}$ in Eq. A.10, $T^{(j)}$ is independent from the choice of the system origin. Furthermore, the equation Eq. A.11 is valid for any incident field. One can thus write Eq. A.11 by removing the a and by multiplying on the right by $J^{(0,j)}$. The properties of the $J^{(0,j)}$ give us:

$$\mathbf{T}^{(j)} = t^{(j)} + t^{(j)} \sum_{l=1,l\neq j}^{N} \mathbf{H}^{(j,l)}\mathbf{T}^{(l)}\mathbf{J}^{(l,j)} \tag{A.12}$$

A.1.4.2 Solution of multiple scattering problem by direct inversion

We solve the equation Eq. **??** with the matricial form:

$$\begin{bmatrix} e^{(1)} \\ e^{(2)} \\ \vdots \\ e^{(N)} \end{bmatrix} = \begin{bmatrix} \mathbb{I} & -\mathbf{H}^{(1,2)}t^{(2)} & \cdots & -\mathbf{H}^{(1,N)}t^{(N)} \\ -\mathbf{H}^{(2,1)}t^{(1)} & \mathbb{I} & \cdots & -\mathbf{H}^{(2,N)}t^{(N)} \\ \vdots & \vdots & \ddots & \vdots \\ -\mathbf{H}^{(N,1)}t^{(1)} & -\mathbf{H}^{(N,2)}t^{(2)} & \cdots & \mathbb{I} \end{bmatrix}^{-1} \begin{bmatrix} \mathbf{J}^{(1,0)}a \\ \mathbf{J}^{(2,0)}a \\ \vdots \\ \mathbf{J}^{(N,0)}a \end{bmatrix} \tag{A.13}$$

We multiply on the right by the $t^{(j)}$ bloc matrix. $\begin{bmatrix} t^{(1)} & 0 & \cdots & 0 \\ 0 & t^{(2)} & \cdots & 0 \\ \vdots & \vdots & \ddots & \vdots \\ 0 & 0 & \cdots & t^{(N)} \end{bmatrix}$ We then get the scattered field as a function of the incident field.

$$\begin{bmatrix} f^{(1)} \\ f^{(2)} \\ \vdots \\ f^{(N)} \end{bmatrix} \equiv \begin{bmatrix} T^{(1,1)} & T^{(1,2)} & \cdots & T^{(1,N)} \\ T^{(2,1)} & T^{(2,2)} & \cdots & T^{(2,N)} \\ \vdots & \vdots & \ddots & \vdots \\ T^{(N,1)} & T^{(N,2)} & \cdots & T^{(N,N)} \end{bmatrix} \begin{bmatrix} \mathbf{J}^{(1,0)}a \\ \mathbf{J}^{(2,0)}a \\ \vdots \\ \mathbf{J}^{(N,0)}a \end{bmatrix} \tag{A.14}$$

Or also

$$f^{(j)} = \sum_{k=1}^{N} T^{(j,k)} J^{(k,0)} a$$

Appendix B

Spectral expansion of multipolar waves

B.1 Plane wave expansion of Hankel and Bessel functions

Hankel et 0^{th} order Bessel functions

$$h_0^{(+)}(z) = -\frac{i}{z}e^{iz} \tag{B.1}$$

The Weyl identity can then be expressed :

$$h_0^{(+)}(k_b r) = \frac{1}{2\pi k_b}\iint_{-\infty}^{\infty} dk_x dk_y \frac{e^{ik_x x + ik_y y + ik_z|z|}}{k_z} \tag{B.2}$$

$$h_0^{(-)}(z) = \frac{\sin z}{z} + i\frac{\cos z}{z} = \frac{i}{z}(\cos z - i\sin z) = \frac{i}{z}e^{-iz} = h_0^{(+)}(-z)$$

For any $z \in \mathbb{C}$,

$$h_0^{(-)}(z) = \left[h_0^{(+)}(z^*)\right]^*$$

We assume in a first time that $z \in \mathbb{R}$

$$h_n^{(-)}(z) = \left[h_n^{(+)}(z)\right]^*$$

$$h_0^{(-)}(k_b r) = \left[h_0^{(+)}(z)\right]^* = \frac{1}{2\pi k_b}\iint_{-\infty}^{\infty} dk_x dk_y \frac{e^{-ik_x x - ik_y y - ik_z^*|z|}}{k_z^*}$$

$$j_0(k_b r) = \frac{1}{2}[h_0^+(k_b r) + h_0^{(-)}(k_b r)]$$

$$j_0(k_b r) = \frac{1}{2\pi k_b}\int_0^1 KdK\frac{\cos(\mathbf{K}.\mathbf{r} + k_z|z|)}{k_z} + \frac{1}{2\pi k_b}\int_1^\infty KdK\frac{e^{-k_z'|z|}\sin\mathbf{K}.\mathbf{r}}{k_z'}$$

n^{th} order Hankel et Bessel functions

$$h_n^{(+)}(x) = i^{-n}\int_0^\infty \frac{K}{k_b}\, P_n(k_z/k_b)\,\frac{\exp\left[i\,(k_z/k_b)\,x\right]}{k_z/k_b} d\left(\frac{K}{k_b}\right) \tag{B.3}$$

$$h_n^{(-)}(x) = (-i)^{-n}\int_0^\infty \frac{K}{k_b}\, P_n^*(k_z/k_b)\,\frac{\exp\left[-i\left(k_z^*/k_b\right)x\right]}{k_z^*/k_b} d\left(\frac{K}{k_b}\right) \tag{B.4}$$

$$j_n(x) = i^{-n}\int_0^1 \left[\frac{K}{k_b}\, P_n(k_z/k_b)\,(\frac{\exp\left[i\,(k_z/k_b)\,x\right]}{k_z/k_b} + (-1)^n\frac{\exp\left[-i\,(k_z/k_b)\,x\right]}{k_z/k_b})\right] d\left(\frac{K}{k_b}\right)$$

B.2 Regular and irregular vectorial multipolar waves

B.2.1 Irregular outgoing waves

$$\begin{aligned}\mathbf{M}^{(+)}_{nm}(k_b\mathbf{r}) &\equiv h^{(+)}_n(k_br)\,\mathbf{X}_{nm}(\theta,\phi)\\ \mathbf{N}^{(+)}_{nm}(k_b\mathbf{r}) &\equiv \frac{1}{k_br}\left\{\sqrt{n(n+1)}h^{(+)}_n(k_br)\,\mathbf{Y}_{nm}(\theta,\phi)+\left[k_brh^{(+)}_n(k_br)\right]'\mathbf{Z}_{nm}(\theta,\phi)\right\}\end{aligned} \tag{B.5}$$

B.2.1.1 Direct expansion via Clebsch Gordon coefficients:

In order to derive two relations between vector spherical harmonics, it is useful to invoke another set of vector spherical harmonics, denoted $\mathbf{Y}^m_{n,n+1}$, $\mathbf{Y}^m_{n,n}$ and $\mathbf{Y}^m_{n,n-1}$ as introduced by quantum mechanic theoreticians who worked on the angular momentum coupling formalism[[**?**]]. We first recall the definition of the Cartesian spherical unit vectors :

$$\chi_1=-\frac{1}{\sqrt{2}}(\widehat{\mathbf{x}}+i\widehat{\mathbf{y}}),\qquad \chi_0=\widehat{\mathbf{z}},\qquad \chi_{-1}=\frac{1}{\sqrt{2}}(\widehat{\mathbf{x}}-i\widehat{\mathbf{y}}) \tag{B.6}$$

where $\widehat{\mathbf{x}}$, $\widehat{\mathbf{y}}$, $\widehat{\mathbf{z}}$ are the unit vectors of the Cartesian coordinate system. Making use of the Clebsch-Gordan coefficients[[**?**]], the new set of vector spherical harmonics is then defined as :

$$\mathbf{Y}^m_{n,l}=\sum_{\mu=-1}^{1}(l,m-\mu;1,\mu\mid n,m)Y_{l,m-\mu}\chi_\mu \tag{B.7}$$

with $l=n-1,n,n+1$.

Using the conversion from spherical to Cartesian coordinates, and the expressions of our $\mathbf{Y}_{nm},\mathbf{X}_{nm},\mathbf{Z}_{nm}$ vector spherical harmonics in a spherical coordinate system, we can painstakingly verify that our $\mathbf{Y}_{nm}$, $\mathbf{X}_{nm}$ and $\mathbf{Z}_{nm}$ VSHs can be expressed in terms of the $\mathbf{Y}^m_{n,n+1}$, $\mathbf{Y}^m_{n,n}$, $\mathbf{Y}^m_{n,n-1}$ spherical harmonics via the relations :

$$\mathbf{X}_{nm}=\frac{\mathbf{Y}^m_{n,n}}{i} \tag{B.8}$$

$$\mathbf{Z}_{nm}=\left(\frac{n+1}{2n+1}\right)^{1/2}\mathbf{Y}^m_{n,n-1}-\left(\frac{n}{2n+1}\right)^{1/2}\mathbf{Y}^m_{n,n+1} \tag{B.9}$$

$$\mathbf{Y}_{nm}=\left(\frac{n}{2n+1}\right)^{1/2}\mathbf{Y}^m_{n,n-1}+\left(\frac{n+1}{2n+1}\right)^{1/2}\mathbf{Y}^m_{n,n+1} \tag{B.10}$$

Combining with

$$h^{(+)}_n(k_br)\,Y_{nm}(\widehat{\mathbf{r}})=\frac{1}{2\pi i^nk_b}\int d\mathbf{K}\,Y_{nm}\left(\widehat{\mathbf{k}}\right)\frac{\exp(\pm i\mathbf{k}\cdot\mathbf{r})}{k_z}\qquad z\gtrless 0$$

One could conclude that:

$$\mathbf{M}^{(+)}_{nm}(k_b\mathbf{r})=\frac{i^{-n}}{2\pi k}\int d\mathbf{K}\;\mathbf{X}_{nm}\left(\widehat{\mathbf{k}}\right)\frac{\exp(\pm i\mathbf{k}\cdot\mathbf{r})}{k_z}\qquad z\gtrless 0 \tag{B.11}$$

$$\mathbf{N}_{nm}^{(+)}(k_b\mathbf{r}) = \frac{1}{k_b}\boldsymbol{\nabla}_{\mathbf{r}} \times \mathbf{M}_{nm}(k\mathbf{r}) = \frac{i^{-n+1}}{2\pi k_b}\int d\mathbf{K}\, \mathbf{Z}_{nm}\left(\widehat{\mathbf{k}}\right)\frac{\exp\left(\pm i\mathbf{k}\cdot\mathbf{r}\right)}{k_z} \qquad z \gtrless 0$$

However, we employ the Cartesian base of spherical harmonics to expand the field. We start form the following equation without simplifying as above.

$$\mathbf{M}_{nm}^{(+)}(k_b\mathbf{r}) = \frac{1}{2\pi(i)^n k_b}\int d\mathbf{K}\sum_{\mu=-1}^{1}(n, m-\mu; 1, \mu \mid n, m)\frac{Y_{nm-\mu}\left(\widehat{\mathbf{k}}\right)}{i}\boldsymbol{\chi}_\mu\frac{\exp\left(\pm i\mathbf{k}\cdot\mathbf{r}\right)}{k_z}$$

$$\begin{aligned}\mathbf{N}_{nm}^{(+)}(k_b\mathbf{r}) = \frac{i^{-n+1}}{2\pi k_b}\int d\mathbf{K}\sum_{\mu=-1}^{1}\Bigg[&\left(\frac{n+1}{2n+1}\right)^{1/2}(n-1, m-\mu; 1, \mu \mid n, m)Y_{n-1,m-\mu}\\ &-\left(\frac{n}{2n+1}\right)^{1/2}(n+1, m-\mu; 1, \mu \mid n, m)Y_{n+1,m-\mu}\Bigg]\boldsymbol{\chi}_\mu\frac{\exp\left(\pm i\mathbf{k}\cdot\mathbf{r}\right)}{k_z} \qquad z \gtrless 0\end{aligned}$$

Irregular ougoing magnetic waves

$$\mathbf{M}_{nm}^{(+)}(k_b\mathbf{r}) = \frac{1}{2\pi(i)^n k_b}\int d\mathbf{K}\sum_{\mu=-1}^{1}(n, m-\mu; 1, \mu \mid n, m)\frac{Y_{nm-\mu}\left(\widehat{\mathbf{k}}\right)}{i}\boldsymbol{\chi}_\mu\frac{\exp\left(\pm i\mathbf{k}\cdot\mathbf{r}\right)}{k_z}$$

We assume $m = 1$

$$\begin{aligned}\mathbf{M}_{n1}^{(+)}(k_b\mathbf{r}) = \frac{1}{2\pi(i)^n k_b}\int_0^\infty\int_0^{2\pi} KdKd\phi_k\frac{\exp\left(\pm i\mathbf{k}\cdot\mathbf{r}\right)}{k_z}\\ \times\begin{bmatrix}(n, 2; 1, -1 \mid n, 1)\frac{Y_{n2}\left(\widehat{\mathbf{k}}\right)}{i}\boldsymbol{\chi}_{-1}\\ (n, 1; 1, 0 \mid n, 1)\frac{Y_{n1}\left(\widehat{\mathbf{k}}\right)}{i}\boldsymbol{\chi}_0\\ (n, 0; 1, 1 \mid n, 1)\frac{Y_{n0}\left(\widehat{\mathbf{k}}\right)}{i}\boldsymbol{\chi}_1\end{bmatrix}\end{aligned}$$

$$Y_{n,m}(\theta, \phi) \equiv c_{n,m}P_n^m(\cos\theta)e^{im\phi}$$

$$c_{n,m} = \left[\frac{2n+1}{4\pi}\frac{(n-m)!}{(n+m)!}\right]^{\frac{1}{2}}$$

$$\begin{aligned}\mathbf{M}_{n1}^{(+)}(k_b\mathbf{r}) = \frac{1}{2\pi(i)^n k_b}\int_0^\infty\int_0^{2\pi} KdKd\phi_k\,\frac{\exp\left(iK.r_{//}\cos(\phi_k-\phi)+ik_z|z|\right)}{k_z}\\ \times\begin{bmatrix}(n, 2; 1, -1 \mid n, 1)\frac{c_{n,2}P_n^2(\cos\theta_k)e^{i2\phi_k}}{i}\boldsymbol{\chi}_{-1}\\ (n, 1; 1, 0 \mid n, 1)\frac{c_{n,1}P_n^1(\cos\theta_k)e^{i\phi_k}}{i}\boldsymbol{\chi}_0\\ (n, 0; 1, 1 \mid n, 1)\frac{c_{n,0}P_n^0(\cos\theta_k)}{i}\boldsymbol{\chi}_1\end{bmatrix}\end{aligned}$$

We know that [52] (p. 395)

$$\int_0^{2\pi}\exp(ix\cos(\phi_k-\phi))\exp(in\phi_k)d\phi_k = 2\pi i^n J_n(x)\exp(in\phi) \tag{B.12}$$

$$\mathbf{M}_{n1}^{(+)}(k_b\mathbf{r}) = \frac{1}{(i)^n k_b}\int_0^\infty KdK\frac{\exp(ik_z|z|)}{k_z} \times \begin{bmatrix} -J_2(K.r_{//})(n,2;1,-1\mid n,1)\frac{c_{n,2}P_n^2(\cos\theta_k)e^{i2\phi}}{i\sqrt{2}}\{\widehat{\mathbf{x}}-\widehat{\mathbf{iy}}\} \\ iJ_1(K.r_{//})(n,1;1,0\mid n,1)\frac{c_{n,1}P_n^1(\cos\theta_k)e^{i\phi}}{i}\widehat{\mathbf{z}} \\ -J_0(K.r_{//})(n,0;1,1\mid n,1)\frac{c_{n,0}P_n^0(\cos\theta_k)}{i\sqrt{2}}\{\widehat{\mathbf{x}}+\widehat{\mathbf{iy}}\} \end{bmatrix}$$

assuming $m=-1$

$$\mathbf{M}_{n,-1}^{(+)}(k_b\mathbf{r}) = \frac{1}{2\pi(i)^n k_b}\int d\mathbf{K}\sum_{\mu=-1}^{1}(n,m-\mu;1,\mu\mid n,m)\frac{Y_{nm-\mu}\left(\widehat{\mathbf{k}}\right)}{i}\boldsymbol{\chi}_\mu\frac{\exp(\pm i\mathbf{k}\cdot\mathbf{r})}{k_z}$$

$$\mathbf{M}_{n-1}^{(+)}(k_b\mathbf{r}) = \frac{1}{2\pi(i)^n k_b}\int_0^\infty\int_0^{2\pi}KdKd\phi_k\frac{\exp(\pm i\mathbf{k}\cdot\mathbf{r})}{k_z} \times \begin{bmatrix} (n,0;1,-1\mid n,-1)\frac{Y_{n0}\left(\widehat{\mathbf{k}}\right)}{i}\boldsymbol{\chi}_{-1} \\ (n,-1;1,0\mid n,-1)\frac{Y_{n-1}\left(\widehat{\mathbf{k}}\right)}{i}\boldsymbol{\chi}_0 \\ (n,-2;1,1\mid n,-1)\frac{Y_{n-2}\left(\widehat{\mathbf{k}}\right)}{i}\boldsymbol{\chi}_1 \end{bmatrix}$$

$$Y_{n,m}(\theta,\phi) \equiv c_{n,m}P_n^m(\cos\theta)e^{im\phi}$$

$$c_{n,m} = \left[\frac{2n+1}{4\pi}\frac{(n-m)!}{(n+m)!}\right]^{\frac{1}{2}}$$

$$\mathbf{M}_{n-1}^{(+)}(k_b\mathbf{r}) = \frac{1}{2\pi(i)^n k_b}\int_0^\infty\int_0^{2\pi}KdKd\phi_k\frac{\exp(iK.r_{//}\cos(\phi_k-\phi)+ik_z|z|)}{k_z} \times \begin{bmatrix} (n,0;1,-1\mid n,-1)\frac{c_{n,0}P_n^0(\cos\theta_k)}{i}\boldsymbol{\chi}_{-1} \\ (n,-1;1,0\mid n,-1)\frac{c_{n,-1}P_n^{-1}(\cos\theta_k)e^{-i\phi_k}}{i}\boldsymbol{\chi}_0 \\ (n,-2;1,1\mid n,-1)\frac{c_{n,-2}P_n^{-2}(\cos\theta_k)e^{-i2\phi_k}}{i}\boldsymbol{\chi}_1 \end{bmatrix}$$

We know that (Ref. 52, p395)

$$\int_0^{2\pi}\exp(ix\cos(\phi_k-\phi))\exp(in\phi_k)d\phi_k = 2\pi i^n J_n(x)\exp(in\phi) \tag{B.13}$$

$$\mathbf{M}_{n-1}^{(+)}(k_b\mathbf{r}) = \frac{1}{(i)^n k_b}\int_0^\infty KdK\frac{\exp(ik_z|z|)}{k_z} \times \begin{bmatrix} -J_0(K.r_{//})(n,0;1,-1\mid n,-1)\frac{c_{n,0}P_n^0(\cos\theta_k)}{i\sqrt{2}}\{\widehat{\mathbf{x}}-\widehat{\mathbf{iy}}\} \\ -iJ_1(K.r_{//})(n,1;-1,0\mid n,-1)\frac{c_{n,-1}P_n^{-1}(\cos\theta_k)e^{-i\phi}}{i}\widehat{\mathbf{z}} \\ -J_2(K.r_{//})(n,-2;1,1\mid n,-1)\frac{c_{n,2}P_n^{-2}(\cos\theta_k)e^{-i2\phi}}{i\sqrt{2}}\{\widehat{\mathbf{x}}+\widehat{\mathbf{iy}}\} \end{bmatrix}$$

Irregular outgoing electric waves

$$\mathbf{N}_{nm}^{(+)}(k_b\mathbf{r}) \equiv \frac{1}{k_b r}\left\{\sqrt{n\,(n+1)}h_n^{(+)}(k_b r)\,\mathbf{Y}_{nm}(\theta,\phi) + \left[k_b r h_n^{(+)}(k_b r)\right]'\mathbf{Z}_{nm}(\theta,\phi)\right\}$$

$$\left[x h_n^{(+)}(x)\right]' = h_n^{(+)}(x) + x h_n^{(+)\prime}(x) = (n+1)h_n^{(+)}(x) - x h_{n+1}^{(+)}(x)$$

$$\mathbf{N}_{nm}^{(+)}(k_b\mathbf{r}) \equiv \frac{1}{k_b r}\left\{\sqrt{n\,(n+1)}h_n^{(+)}(k_b r)\,\mathbf{Y}_{nm}(\theta,\phi) + \left[(n+1)h_n^{(+)}(k_b r) - k_b r h_{n+1}^{(+)}(k_b r)\right]\mathbf{Z}_{nm}(\theta,\phi)\right\}$$

We get

$$\mathbf{Z}_{nm} = \left(\frac{n+1}{2n+1}\right)^{1/2}\mathbf{Y}_{n,n-1}^{m} - \left(\frac{n}{2n+1}\right)^{1/2}\mathbf{Y}_{n,n+1}^{m} \tag{B.14}$$

$$\mathbf{Y}_{nm} = \left(\frac{n}{2n+1}\right)^{1/2}\mathbf{Y}_{n,n-1}^{m} + \left(\frac{n+1}{2n+1}\right)^{1/2}\mathbf{Y}_{n,n+1}^{m} \tag{B.15}$$

$$\mathbf{N}_{nm}^{(+)}(k_b\mathbf{r}) = \frac{1}{k_b r}\left\{\sqrt{n\,(n+1)}h_n^{(+)}(k_b r)\left[\left(\frac{n}{2n+1}\right)^{1/2}\mathbf{Y}_{n,n-1}^{m} + \left(\frac{n+1}{2n+1}\right)^{1/2}\mathbf{Y}_{n,n+1}^{m}\right]\right. \tag{B.16}$$

$$\left. + \left[(n+1)h_n^{(+)}(k_b r) - k_b r h_{n+1}^{(+)}(k_b r)\right]\left[\left(\frac{n+1}{2n+1}\right)^{1/2}\mathbf{Y}_{n,n-1}^{m} - \left(\frac{n}{2n+1}\right)^{1/2}\mathbf{Y}_{n,n+1}^{m}\right]\right\} \tag{B.17}$$

$$\mathbf{N}_{nm}^{(+)}(k_b\mathbf{r}) = \frac{1}{k_b r}\{\mathbf{N}_{nm}^{(+),1}(k_b\mathbf{r}) + \mathbf{N}_{nm}^{(+),2}(k_b\mathbf{r})\}$$

$$\mathbf{N}_{nm}^{(+),1}(k_b\mathbf{r}) = \sqrt{n\,(n+1)}h_n^{(+)}(k_b r)\left[\left(\frac{n}{2n+1}\right)^{1/2}\mathbf{Y}_{n,n-1}^{m} + \left(\frac{n+1}{2n+1}\right)^{1/2}\mathbf{Y}_{n,n+1}^{m}\right]$$

$$\mathbf{N}_{nm}^{(+),2}(k_b\mathbf{r}) = (n+1)h_n^{(+)}(k_b r)\left[\left(\frac{n+1}{2n+1}\right)^{1/2}\mathbf{Y}_{n,n-1}^{m} - \left(\frac{n}{2n+1}\right)^{1/2}\mathbf{Y}_{n,n+1}^{m}\right]$$
$$- k_b r h_{n+1}^{(+)}(k_b r)\left[\left(\frac{n+1}{2n+1}\right)^{1/2}\mathbf{Y}_{n,n-1}^{m} - \left(\frac{n}{2n+1}\right)^{1/2}\mathbf{Y}_{n,n+1}^{m}\right]$$

$$\mathbf{N}_{nm}^{(+),1}(k_b\mathbf{r}) + \mathbf{N}_{nm}^{(+),2}(k_b\mathbf{r}) = h_n^{(+)}(k_b r)\,\mathbf{Y}_{n,n-1}^{m}\left[\sqrt{n\,(n+1)}\left(\frac{n}{2n+1}\right)^{1/2} + (n+1)\left(\frac{n+1}{2n+1}\right)^{1/2}\right]$$
$$+ h_n^{(+)}(k_b r)\,\mathbf{Y}_{n,n+1}^{m}\left[\sqrt{n\,(n+1)}\left(\frac{n+1}{2n+1}\right)^{1/2} - (n+1)\left(\frac{n}{2n+1}\right)^{1/2}\right]$$
$$- k_b r h_{n+1}^{(+)}(k_b r)\left[\left(\frac{n+1}{2n+1}\right)^{1/2}\mathbf{Y}_{n,n-1}^{m} - \left(\frac{n}{2n+1}\right)^{1/2}\mathbf{Y}_{n,n+1}^{m}\right]$$

$$\mathbf{N}_{nm}^{(+),1}(k_b\mathbf{r}) + \mathbf{N}_{nm}^{(+),2}(k_b\mathbf{r}) = \sqrt{(2n+1)(n+1)}h_n^{(+)}(k_br)\,\mathbf{Y}_{n,n-1}^m - k_brh_{n+1}^{(+)}(k_br)\left[\left(\frac{n+1}{2n+1}\right)^{1/2}\mathbf{Y}_{n,n-1}^m - \left(\frac{n}{2n+1}\right)^{1/2}\mathbf{Y}_{n,n+1}^m\right]$$

$$\mathbf{N}_{nm}^{(+),1}(k_b\mathbf{r}) + \mathbf{N}_{nm}^{(+),2}(k_b\mathbf{r}) = \sqrt{(2n+1)(n+1)}h_n^{(+)}(k_br)\,\mathbf{Y}_{n,n-1}^m - k_brh_{n+1}^{(+)}(k_br)\left(\frac{n+1}{2n+1}\right)^{1/2}\mathbf{Y}_{n,n-1}^m + k_brh_{n+1}^{(+)}(k_br)\left(\frac{n}{2n+1}\right)^{1/2}\mathbf{Y}_{n,n+1}^m$$

$$h_{n+1}^{(+)}(k_br) = \frac{2n+1}{k_br}h_n^{(+)}(k_br) - h_{n-1}^{(+)}(k_br)$$

$$\mathbf{N}_{nm}^{(+),1}(k_b\mathbf{r}) + \mathbf{N}_{nm}^{(+),2}(k_b\mathbf{r}) = \sqrt{(2n+1)(n+1)}h_n^{(+)}(k_br)\,\mathbf{Y}_{n,n-1}^m - k_br\left[\frac{2n+1}{k_br}h_n^{(+)}(k_br) - h_{n-1}^{(+)}(k_br)\right]\left(\frac{n+1}{2n+1}\right)^{1/2}\mathbf{Y}_{n,n-1}^m + k_brh_{n+1}^{(+)}(k_br)\left(\frac{n}{2n+1}\right)^{1/2}\mathbf{Y}_{n,n+1}^m$$

$$\mathbf{N}_{nm}^{(+),1}(k_b\mathbf{r}) + \mathbf{N}_{nm}^{(+),2}(k_b\mathbf{r}) = \left[\sqrt{(2n+1)(n+1)} - (2n+1)\left(\frac{n+1}{2n+1}\right)^{1/2}\right]h_n^{(+)}(k_br)\mathbf{Y}_{n,n-1}^m + k_brh_{n-1}^{(+)}(k_br)\left(\frac{n+1}{2n+1}\right)^{1/2}\mathbf{Y}_{n,n-1}^m + k_brh_{n+1}^{(+)}(k_br)\left(\frac{n}{2n+1}\right)^{1/2}\mathbf{Y}_{n,n+1}^m$$

$$\mathbf{N}_{nm}^{(+),1}(k_b\mathbf{r}) + \mathbf{N}_{nm}^{(+),2}(k_b\mathbf{r}) = k_brh_{n-1}^{(+)}(k_br)\left(\frac{n+1}{2n+1}\right)^{1/2}\mathbf{Y}_{n,n-1}^m + k_brh_{n+1}^{(+)}(k_br)\left(\frac{n}{2n+1}\right)^{1/2}\mathbf{Y}_{n,n+1}^m$$

$$\mathbf{N}_{nm}^{(+)}(k_b\mathbf{r}) = \frac{1}{k_br}\{\mathbf{N}_{nm}^{(+),1}(k_b\mathbf{r}) + \mathbf{N}_{nm}^{(+),2}(k_b\mathbf{r})\} = h_{n-1}^{(+)}(k_br)\left(\frac{n+1}{2n+1}\right)^{1/2}\mathbf{Y}_{n,n-1}^m + h_{n+1}^{(+)}(k_br)\left(\frac{n}{2n+1}\right)^{1/2}\mathbf{Y}_{n,n+1}^m$$

$$\mathbf{Y}_{n,l}^m = \sum_{\mu=-1}^{1}(l, m-\mu; 1, \mu \mid n, m)Y_{l,m-\mu}\boldsymbol{\chi}_\mu$$

$$\mathbf{N}_{nm}^{(+)}(k_b\mathbf{r}) = \sum_{\mu=-1}^{1}\left[\left(\frac{n+1}{2n+1}\right)^{1/2}(n-1,m-\mu;1,\mu\mid n,m)h_{n-1}^{(+)}(k_br)Y_{n-1,m-\mu}\right.$$
$$+\left(\frac{n}{2n+1}\right)^{1/2}(n+1,m-\mu;1,\mu\mid n,m)h_{n+1}^{(+)}(k_br)Y_{n+1,m-\mu}$$
$$\left.+\left(\frac{n}{2n+1}\right)^{1/2}(n+1,m-\mu;1,\mu\mid n,m)h_{n+1}^{(+)}(k_br)Y_{n+1,m-\mu}\right]\boldsymbol{\chi}_\mu$$

$$h_n^{(+)}(k_br)\,Y_{nm}(\widehat{\mathbf{r}}) = \frac{1}{2\pi i^n k_b}\int d\mathbf{K}\,Y_{nm}\left(\widehat{\mathbf{k}}\right)\frac{\exp\left(\pm i\mathbf{k}\cdot\mathbf{r}\right)}{k_z} \qquad z \gtrless 0$$

$$\mathbf{N}_{nm}^{(+)}(k_b\mathbf{r}) = \frac{1}{2\pi i^{n-1}k_b}\int d\mathbf{K}\sum_{\mu=-1}^{1}\left[\left(\frac{n+1}{2n+1}\right)^{1/2}(n-1,m-\mu;1,\mu\mid n,m)Y_{n-1,m-\mu}\left(\widehat{\mathbf{k}}\right)\right.$$
$$\left.-\left(\frac{n}{2n+1}\right)^{1/2}(n+1,m-\mu;1,\mu\mid n,m)\,Y_{n+1m-\mu}\left(\widehat{\mathbf{k}}\right)\right]\frac{\exp\left(\pm i\mathbf{k}\cdot\mathbf{r}\right)}{k_z}\boldsymbol{\chi}_\mu$$

We get

$$\mathbf{N}_{nm}^{(+)}(k_b\mathbf{r}) = \frac{i^{-n+1}}{2\pi k_b}\int d\mathbf{K}\,\mathbf{Z}_{nm}\left(\widehat{\mathbf{k}}\right)\frac{\exp\left(\pm i\mathbf{k}\cdot\mathbf{r}\right)}{k_z} \qquad z \gtrless 0$$

$$Y_{n,m}(\theta,\phi) \equiv c_{n,m}P_n^m(\cos\theta)e^{im\phi}$$

$$c_{n,m} = \left[\frac{2n+1}{4\pi}\frac{(n-m)!}{(n+m)!}\right]^{\frac{1}{2}}$$

$$\mathbf{N}_{n1}^{(+)}(k_b\mathbf{r}) = \frac{i^{-n+1}}{2\pi k_b}\int d\mathbf{K}\frac{\exp\left(\pm i\mathbf{k}\cdot\mathbf{r}\right)}{k_z}$$
$$\times\begin{bmatrix}\left[\left(\frac{n+1}{2n+1}\right)^{1/2}(n-1,2;1,-1\mid n,1)Y_{n-1,2}-\left(\frac{n}{2n+1}\right)^{1/2}(n+1,2;1,-1\mid n,1)Y_{n+1,2}\right]\boldsymbol{\chi}_{-1}\\ \left[\left(\frac{n+1}{2n+1}\right)^{1/2}(n-1,1;1,0\mid n,1)Y_{n-1,1}-\left(\frac{n}{2n+1}\right)^{1/2}(n+1,1;1,0\mid n,1)Y_{n+1,1}\right]\boldsymbol{\chi}_0\\ \left[\left(\frac{n+1}{2n+1}\right)^{1/2}(n-1,0;1,1\mid n,1)Y_{n-1,0}-\left(\frac{n}{2n+1}\right)^{1/2}(n+1,0;1,1\mid n,1)Y_{n+1,0}\right]\boldsymbol{\chi}_1\end{bmatrix} \qquad z \gtrless$$

$$\mathbf{N}_{n1}^{(+)}(k_b\mathbf{r}) = \frac{i^{-n+1}}{2\pi k_b}\int\int KdKd\phi_k \frac{\exp\left(iK.r_{//}\cos(\phi_k-\phi)+ik_z|z|\right)}{k_z}$$
$$\times\begin{bmatrix} \frac{1}{\sqrt{2}}\begin{bmatrix} \left(\frac{n+1}{2n+1}\right)^{1/2}(n-1,2;1,-1\mid n,1)c_{n-1,2}P_{n-1}^{2}(\cos\theta_k) \\ -\left(\frac{n}{2n+1}\right)^{1/2}(n+1,2;1,-1\mid n,1)c_{n+1,2}P_{n+1}^{2}(\cos\theta_k)\end{bmatrix} e^{i2\phi_k}\{\widehat{\mathbf{x}}-i\widehat{\mathbf{y}}\} \\ \begin{bmatrix} \left(\frac{n+1}{2n+1}\right)^{1/2}(n-1,1;1,0\mid n,1)c_{n-1,1}P_{n-1}^{1}(\cos\theta_k) \\ -\left(\frac{n}{2n+1}\right)^{1/2}(n+1,1;1,0\mid n,1)c_{n+1,1}P_{n+1}^{1}(\cos\theta_k)\end{bmatrix} e^{i\phi_k}\widehat{\mathbf{z}} \\ \frac{-1}{\sqrt{2}}\begin{bmatrix} \left(\frac{n+1}{2n+1}\right)^{1/2}(n-1,0;1,1\mid n,1)c_{n-1,0}P_{n-1}^{0}(\cos\theta_k) \\ -\left(\frac{n}{2n+1}\right)^{1/2}(n+1,0;1,1\mid n,1)c_{n-1,0}P_{n+1}^{0}(\cos\theta_k)\end{bmatrix}\{\widehat{\mathbf{x}}+i\widehat{\mathbf{y}}\}\end{bmatrix} \qquad z\gtrless 0$$

We know that [52] (p. 395)

$$\int_0^{2\pi}\exp(ix\cos(\phi_k-\phi))\exp(in\phi_k)d\phi_k = 2\pi i^n J_n(x)\exp(in\phi) \tag{B.18}$$

$$\mathbf{N}_{n1}^{(+)}(k_b\mathbf{r}) = \frac{i^{-n+1}}{k_b}\int KdK\frac{\exp\left(ik_z|z|\right)}{k_z}$$
$$\times\begin{bmatrix} \frac{-1}{\sqrt{2}}J_2(K.r_{//})\begin{bmatrix} \left(\frac{n+1}{2n+1}\right)^{1/2}(n-1,2;1,-1\mid n,1)c_{n-1,2}P_{n-1}^{2}(\cos\theta_k) \\ -\left(\frac{n}{2n+1}\right)^{1/2}(n+1,2;1,-1\mid n,1)c_{n+1,2}P_{n+1}^{2}(\cos\theta_k)\end{bmatrix} e^{2i\phi}\{\widehat{\mathbf{x}}-i\widehat{\mathbf{y}}\} \\ iJ_1(K.r_{//})\begin{bmatrix} \left(\frac{n+1}{2n+1}\right)^{1/2}(n-1,1;1,0\mid n,1)c_{n-1,1}P_{n-1}^{1}(\cos\theta_k) \\ -\left(\frac{n}{2n+1}\right)^{1/2}(n+1,1;1,0\mid n,1)c_{n+1,1}P_{n+1}^{1}(\cos\theta_k)\end{bmatrix} e^{i\phi}\widehat{\mathbf{z}} \\ \frac{-1}{\sqrt{2}}J_0(K.r_{//})\begin{bmatrix} \left(\frac{n+1}{2n+1}\right)^{1/2}(n-1,0;1,1\mid n,1)c_{n-1,0}P_{n-1}^{0}(\cos\theta_k) \\ -\left(\frac{n}{2n+1}\right)^{1/2}(n+1,0;1,1\mid n,1)c_{n+1,0}P_{n+1}^{0}(\cos\theta_k)\end{bmatrix}\{\widehat{\mathbf{x}}+i\widehat{\mathbf{y}}\}\end{bmatrix} \qquad z\gtrless 0$$

Assuming m = -1

$$\mathbf{N}_{nm}^{(+)}(k_b\mathbf{r}) = \frac{1}{2\pi i^{n-1}k_b}\int d\mathbf{K}\sum_{\mu=-1}^{1}\left[\left(\frac{n+1}{2n+1}\right)^{1/2}(n-1,m-\mu;1,\mu\mid n,m)Y_{n-1,m-\mu}\left(\widehat{\mathbf{k}}\right)\right.$$
$$\left.-\left(\frac{n}{2n+1}\right)^{1/2}(n+1,m-\mu;1,\mu\mid n,m)\,Y_{n+1m-\mu}\left(\widehat{\mathbf{k}}\right)\right]\frac{\exp\left(\pm i\mathbf{k}\cdot\mathbf{r}\right)}{k_z}\boldsymbol{\chi}_\mu$$

$$\mathbf{N}_{n-1}^{(+)}(k_b\mathbf{r}) = \frac{i^{-n+1}}{2\pi k_b}\int d\mathbf{K}\frac{\exp\left(\pm i\mathbf{k}\cdot\mathbf{r}\right)}{k_z}$$
$$\times\begin{bmatrix} \left[\left(\frac{n+1}{2n+1}\right)^{1/2}(n-1,-2;1,1\mid n,-1)Y_{n-1,-2}-\left(\frac{n}{2n+1}\right)^{1/2}(n+1,-2;1,1\mid n,-1)Y_{n+1,-2}\right]\boldsymbol{\chi}_1 \\ \left[\left(\frac{n+1}{2n+1}\right)^{1/2}(n-1,-1;1,0\mid n,-1)Y_{n-1,-1}-\left(\frac{n}{2n+1}\right)^{1/2}(n+1,-1;1,0\mid n,-1)Y_{n+1,-1}\right]\boldsymbol{\chi}_0 \\ \left[\left(\frac{n+1}{2n+1}\right)^{1/2}(n-1,0;1,-1\mid n,-1)Y_{n-1,0}-\left(\frac{n}{2n+1}\right)^{1/2}(n+1,0;1,-1\mid n,-1)Y_{n+1,0}\right]\boldsymbol{\chi}_{-1}\end{bmatrix}$$

We know that [52] (p. 395)

$$\int_0^{2\pi} \exp(ix\cos(\phi_k-\phi))\exp(in\phi_k)d\phi_k = 2\pi i^n J_n(x)\exp(in\phi) \tag{B.19}$$

$$\mathbf{N}^{(+)}_{n-1}(k_b\mathbf{r}) = \frac{i^{-n+1}}{k_b}\int KdK\frac{\exp(ik_z|z|)}{k_z}$$
$$\times\begin{bmatrix} \frac{-1}{\sqrt{2}}J_2(K.r_{//})\begin{bmatrix} \left(\frac{n+1}{2n+1}\right)^{1/2}(n-1,-2;1,-1\mid n,-1)c_{n-1,-2}P^{-2}_{n-1}(\cos\theta_k) \\ -\left(\frac{n}{2n+1}\right)^{1/2}(n+1,-2;1,-1\mid n,-1)c_{n+1,-2}P^{-2}_{n+1}(\cos\theta_k)\end{bmatrix}e^{-2i\phi}\{\widehat{\mathbf{x}}+i\widehat{\mathbf{y}}\} \\ iJ_1(K.r_{//})\begin{bmatrix} \left(\frac{n+1}{2n+1}\right)^{1/2}(n-1,-1;1,0\mid n,-1)c_{n-1,-1}P^{-1}_{n-1}(\cos\theta_k) \\ -\left(\frac{n}{2n+1}\right)^{1/2}(n+1,-1;1,0\mid n,-1)c_{n+1,-1}P^{-1}_{n+1}(\cos\theta_k)\end{bmatrix}e^{-i\phi}\widehat{\mathbf{z}} \\ \frac{-1}{\sqrt{2}}J_0(K.r_{//})\begin{bmatrix} \left(\frac{n+1}{2n+1}\right)^{1/2}(n-1,0;1,-1\mid n,1)c_{n-1,0}P^{0}_{n-1}(\cos\theta_k) \\ -\left(\frac{n}{2n+1}\right)^{1/2}(n+1,0;1,-1\mid n,1)c_{n+1,0}P^{0}_{n+1}(\cos\theta_k)\end{bmatrix}\{\widehat{\mathbf{x}}-i\widehat{\mathbf{y}}\}\end{bmatrix} \qquad z\gtrless 0$$

B.2.2 Scattered field

For a circularly right polarized incident beam, the scattered field can be expressed as:

$$\overrightarrow{\mathbf{E}}_{scat}(r_{//},\phi,z) = E_0\int_0^\infty \frac{K}{k_b}d\frac{K}{k_b}\begin{bmatrix} A(\frac{K}{k_b},\phi,z)J_0(Kr_{//})\frac{\{\widehat{\mathbf{x}}+i\widehat{\mathbf{y}}\}}{\sqrt{2}} \\ B(\frac{K}{k_b},\phi,z)J_1(Kr_{//})\widehat{\mathbf{z}} \\ C(\frac{K}{k_b},\phi,z)J_2(Kr_{//})\frac{\{\widehat{\mathbf{x}}-i\widehat{\mathbf{y}}\}}{\sqrt{2}}\end{bmatrix} \tag{B.20}$$

$$\mathbf{E}_{\text{scat}}(r_{//},\phi,z) = E_0\int_0^\infty \frac{K}{k_b}d\frac{K}{k_b}\begin{bmatrix} A(\frac{K}{k_b},\phi,z)J_0(Kr_{//})\frac{\{\hat{\mathbf{x}}+i\hat{\mathbf{y}}\}}{\sqrt{2}} \\ B(\frac{K}{k_b},\phi,z)J_1(Kr_{//})\hat{\mathbf{z}} \\ C(\frac{K}{k_b},\phi,z)J_2(Kr_{//})\frac{\{\hat{\mathbf{x}}-i\hat{\mathbf{y}}\}}{\sqrt{2}}\end{bmatrix}\text{with}\begin{aligned} A &= \sum_{n=0}^{\infty} f_n^{(h)}A_n^{(h)} + f_n^{(e)}A_n^{(e)} \\ B &= \sum_{n=0}^{\infty} f_n^{(h)}B_n^{(h)} + f_n^{(e)}B_n^{(e)} \\ C &= \sum_{n=0}^{\infty} f_n^{(h)}C_n^{(h)} + f_n^{(e)}C_n^{(e)}\end{aligned}$$

$$\begin{aligned} A_n^{(h)} &= \tfrac{-1}{i^{n+1}}(n,0;1,1|n,1)c_{n,0}P^0_n(\sqrt{1-\tfrac{K}{k_b}})\frac{e^{ik_b|z|\sqrt{1-\frac{K}{k_b}}}}{\sqrt{1-\frac{K}{k_b}}} \\ B_n^{(h)} &= \tfrac{1}{i^n}(n,1;1,0|n,1)c_{n,1}P^1_n(\sqrt{1-\tfrac{K}{k_b}})e^{i\phi}\frac{e^{ik_b|z|\sqrt{1-\frac{K}{k_b}}}}{\sqrt{1-\frac{K}{k_b}}} \\ C_n^{(h)} &= \tfrac{-1}{i^{n+1}}(n,2;1,-1|n,1)c_{n,2}P^2_n(\sqrt{1-\tfrac{K}{k_b}})e^{2i\phi}\frac{e^{ik_b|z|\sqrt{1-\frac{K}{k_b}}}}{\sqrt{1-\frac{K}{k_b}}}\end{aligned}$$

$$A_n^{(e)} = \frac{-1}{i^{n-1}} \left[\begin{array}{l} \sqrt{\frac{n+1}{2n+1}}(n-1,0;1,1|n,1)c_{n-1,0}P_{n-1}^0(\sqrt{1-\frac{K}{k_b}}) \\ +\sqrt{\frac{n}{2n+1}}(n+1,0;1,1|n,1)c_{n+1,0}P_{n+1}^0(\sqrt{1-\frac{K}{k_b}}) \end{array} \right] \frac{e^{ik_b|z|\sqrt{1-\frac{K}{k_b}}}}{\sqrt{1-\frac{K}{k_b}}}$$

$$B_n^{(e)} = \frac{i}{i^{n-1}} \left[\begin{array}{l} \sqrt{\frac{n+1}{2n+1}}(n-1,1;1,0|n,1)c_{n-1,1}P_{n-1}^1(\sqrt{1-\frac{K}{k_b}}) \\ +\sqrt{\frac{n}{2n+1}}(n+1,1;1,0|n,1)c_{n+1,1}P_{n+1}^1(\sqrt{1-\frac{K}{k_b}}) \end{array} \right] e^{i\phi} \frac{e^{ik_b|z|\sqrt{1-\frac{K}{k_b}}}}{\sqrt{1-\frac{K}{k_b}}}$$

$$C_n^{(e)} = \frac{-1}{i^{n-1}} \left[\begin{array}{l} \sqrt{\frac{n+1}{2n+1}}(n-1,2;1,-1|n,1)c_{n-1,2}P_{n-1}^2(\sqrt{1-\frac{K}{k_b}}) \\ +\sqrt{\frac{n}{2n+1}}(n+1,2;1,-1|n,1)c_{n+1,2}P_{n+1}^2(\sqrt{1-\frac{K}{k_b}}) \end{array} \right] e^{2i\phi} \frac{e^{ik_b|z|\sqrt{1-\frac{K}{k_b}}}}{\sqrt{1-\frac{K}{k_b}}}$$

B.2.3 Ingoing irregular waves

B.2.3.1 Direct expansion via Clebsch Gordon coefficients:

Irregular ingoing magnetic waves We suppose that:

$$\mathbf{M}_{nm}^{(-)}(k_b\mathbf{r}) \equiv h_n^{(-)}(k_b r)\,\mathbf{X}_{nm}(\theta,\phi)$$

Similarly to outgoing waves, one can expand $\mathbf{X}_{nm}$ on the Cartesian base of spherical harmonics.

$$\begin{aligned} \mathbf{M}_{nm}^{(-)}(k_b\mathbf{r}) &= h_n^{(-)}(k_b r)\,\frac{\mathbf{Y}_{n,n}^m}{i} \\ &= \frac{1}{i}\sum_{\mu=-1}^{1}(n,m-\mu;1,\mu \mid n,m)h_n^{(-)}Y_{n,m-\mu}\boldsymbol{\chi}_\mu \end{aligned}$$

But

$$h_n^{(-)}(k_b r)\,Y_{nm}(\widehat{\mathbf{r}}) = \frac{(-1)^m}{2\pi(-i)^n k_b}\iint_{-\infty}^{\infty} dk_x dk_y\, Y_{nm}^*\left(\widehat{\mathbf{k}}\right)\frac{\exp\left(\mp i\mathbf{k}^*\cdot\mathbf{r}\right)}{k_z^*}$$

Thus

$$\mathbf{M}_{nm}^{(-)}(k_b\mathbf{r}) = \frac{1}{2\pi(-i)^n k_b}\iint_{-\infty}^{\infty} dk_x dk_y \sum_{\mu=-1}^{1}(n,m-\mu;1,\mu \mid n,m)\frac{(-1)^{m-\mu}Y_{nm-\mu}^*\left(\widehat{\mathbf{k}}\right)}{i}\boldsymbol{\chi}_\mu\frac{\exp\left(\mp i\mathbf{k}^*\cdot\mathbf{r}\right)}{k_z^*}$$

$$\begin{aligned} \mathbf{M}_{nm}^{(-)}(k_b\mathbf{r}) = \frac{1}{2\pi(-i)^n k_b}\iint_{-\infty}^{\infty} dk_x dk_y \frac{\exp\left(\mp i\mathbf{k}^*\cdot\mathbf{r}\right)}{k_z^*} \\ \times\left[\begin{array}{c} (n,m+1;1,-1 \mid n,m)\frac{(-1)^{m+1}Y_{nm+1}^*\left(\widehat{\mathbf{k}}\right)}{i}\boldsymbol{\chi}_{-1} \\ (n,m;1,0 \mid n,m)\frac{(-1)^m Y_{nm-1}^*\left(\widehat{\mathbf{k}}\right)}{i}\boldsymbol{\chi}_0 \\ (n,m-1;1,1 \mid n,m)\frac{(-1)^{m-1}Y_{nm-1}^*\left(\widehat{\mathbf{k}}\right)}{i}\boldsymbol{\chi}_1 \end{array} \right] \end{aligned}$$

We suppose that $m = 1$

$$\mathbf{M}_{n1}^{(-)}(k_b\mathbf{r}) = \frac{1}{2\pi(-i)^n k_b}\int_0^\infty\int_0^{2\pi} KdKd\phi_k \frac{\exp\left(-iK.r_{//}\cos(\phi_k-\phi)-ik_z^*|z|\right)}{k_z^*} \times\begin{bmatrix} -(n,2;1,-1\mid n,1)\frac{Y_{n2}^*(\widehat{\mathbf{k}})}{i\sqrt{2}}\{\widehat{\mathbf{x}}+\widehat{\mathbf{iy}}\} \\ -(n,1;1,0\mid n,1)\frac{Y_{n1}^*(\widehat{\mathbf{k}})}{i}\widehat{\mathbf{z}} \\ (n,0;1,1\mid n,1)\frac{Y_{n0}^*(\widehat{\mathbf{k}})}{i\sqrt{2}}\{\widehat{\mathbf{x}}-\widehat{\mathbf{iy}}\} \end{bmatrix}$$

$$Y_{n,m}(\theta,\phi) \equiv c_{n,m}P_n^m(\cos\theta)e^{im\phi}$$

with

$$c_{n,m} = \left[\frac{2n+1}{4\pi}\frac{(n-m)!}{(n+m)!}\right]^{\frac{1}{2}}$$

and

$$Y_{n,m}^*(\theta,\phi) = c_{n,m}P_n^m([\cos\theta]^*)e^{-im\phi}$$

$$\mathbf{M}_{n1}^{(-)}(k_b\mathbf{r}) = \frac{1}{2\pi(-i)^n k_b}\int_0^\infty\int_0^{2\pi} KdKd\phi_k \frac{\exp\left(-iK.r_{//}\cos(\phi_k-\phi)-ik_z^*|z|\right)}{k_z^*} \times\begin{bmatrix} -(n,2;1,-1\mid n,1)\frac{c_{n,2}P_n^2(\frac{k_z^*}{k_b})e^{-2i\phi_k}}{i\sqrt{2}}\{\widehat{\mathbf{x}}+\widehat{\mathbf{iy}}\} \\ -(n,1;1,0\mid n,1)\frac{c_{n,1}P_n^1(\frac{k_z^*}{k_b})e^{-i\phi_k}}{i}\widehat{\mathbf{z}} \\ (n,0;1,1\mid n,1)\frac{c_{n,0}P_n^0(\frac{k_z^*}{k_b})}{i\sqrt{2}}\{\widehat{\mathbf{x}}-\widehat{\mathbf{iy}}\} \end{bmatrix}$$

We know that [52] (p. 395))

$$\frac{i^{-n}}{2\pi}\int_0^{2\pi}\exp(ix\cos(\alpha))\exp(in\alpha)d\alpha = J_n(x) \tag{B.21}$$

By conjugating, as $J_n(x)$ is a real number, we get:

$$\frac{(-i)^{-n}}{2\pi}\int_0^{2\pi}\exp(-ix\cos(\alpha))\exp(-in\alpha)d\alpha = J_n(x)$$

$$\frac{(-i)^{-n}}{2\pi}\int_0^{2\pi}\exp(-ix\cos(\phi_k-\phi))\exp(-in(\phi_k-\phi))d(\phi_k-\phi) = J_n(x)$$

$$\int_0^{2\pi}\exp(-ix\cos(\phi_k-\phi))\exp(-in\phi_k)d\phi_k = 2\pi(-i)^n J_n(x)\exp(-in\phi)$$

$$\mathbf{M}_{n1}^{(-)}(k_b\mathbf{r}) = \frac{1}{(-i)^n k_b}\int_0^\infty KdK\frac{\exp\left(-ik_z^*|z|\right)}{k_z^*} \times \begin{bmatrix} (n,2;1,-1\mid n,1)J_2(K.r_{//})\frac{c_{n,2}P_n^2(\frac{k_z^*}{k_b})e^{-2i\phi}}{i\sqrt{2}}\{\widehat{\mathbf{x}}+\widehat{\mathbf{iy}}\} \\ (n,1;1,0\mid n,1)J_1(K.r_{//})c_{n,1}P_n^1(\frac{k_z^*}{k_b})e^{-i\phi}\widehat{\mathbf{z}} \\ (n,0;1,1\mid n,1)J_0(K.r_{//})\frac{c_{n,0}P_n^0(\frac{k_z^*}{k_b})}{i\sqrt{2}}\{\widehat{\mathbf{x}}-\widehat{\mathbf{iy}}\} \end{bmatrix}$$

Irregular ingoing electric waves

$$\mathbf{N}_{nm}^{(-)}(k_b\mathbf{r}) \equiv \frac{1}{k_b r}\left\{\sqrt{n\,(n+1)}h_n^{(-)}(k_b r)\,\mathbf{Y}_{nm}(\theta,\phi) + \left[k_b r h_n^{(-)}(k_b r)\right]'\mathbf{Z}_{nm}(\theta,\phi)\right\}$$

$$\left[xh_n^{(-)}(x)\right]' = h_n^{(-)}(x) + xh_n^{(-)\prime}(x) = h_n(x) + x\left[-h_{n+1}(x) + \frac{nh_n(x)}{x}\right] = (n+1)h_n^{(-)}(x) - xh_{n+1}^{(-)}(x)$$

$$\mathbf{N}_{nm}^{(-)}(k_b\mathbf{r}) \equiv \frac{1}{k_b r}\left\{\sqrt{n\,(n+1)}h_n^{(-)}(k_b r)\,\mathbf{Y}_{nm}(\theta,\phi) + \left[(n+1)h_n^{(-)}(k_b r) - k_b r h_{n+1}^{(-)}(k_b r)\right]\mathbf{Z}_{nm}(\theta,\phi)\right\}$$

we obtain

$$\mathbf{Z}_{nm} = \left(\frac{n+1}{2n+1}\right)^{1/2}\mathbf{Y}_{n,n-1}^m - \left(\frac{n}{2n+1}\right)^{1/2}\mathbf{Y}_{n,n+1}^m \tag{B.22}$$

$$\mathbf{Y}_{nm} = \left(\frac{n}{2n+1}\right)^{1/2}\mathbf{Y}_{n,n-1}^m + \left(\frac{n+1}{2n+1}\right)^{1/2}\mathbf{Y}_{n,n+1}^m \tag{B.23}$$

and

$$\mathbf{Y}_{n,l}^m = \sum_{\mu=-1}^{1}(l,m-\mu;1,\mu\mid n,m)Y_{l,m-\mu}\boldsymbol{\chi}_\mu$$

$$\begin{aligned}\mathbf{N}_{nm}^{(-)}(k_b\mathbf{r}) &= \frac{1}{k_b r}\left\{\sqrt{n\,(n+1)}h_n^{(-)}(k_b r)\left[\left(\frac{n}{2n+1}\right)^{1/2}\mathbf{Y}_{n,n-1}^m + \left(\frac{n+1}{2n+1}\right)^{1/2}\mathbf{Y}_{n,n+1}^m\right]\right. \\ &\left. + \left[(n+1)h_n^{(-)}(k_b r) - k_b r h_{n+1}^{(-)}(k_b r)\right]\left[\left(\frac{n+1}{2n+1}\right)^{1/2}\mathbf{Y}_{n,n-1}^m - \left(\frac{n}{2n+1}\right)^{1/2}\mathbf{Y}_{n,n+1}^m\right]\right\} \\ &= \frac{1}{k_b r}\left\{N_{n,m}^{(-),1} + N_{n,m}^{(-),2}\right\}\end{aligned}$$

$$N_{n,m}^{(-),1} = \sqrt{n\,(n+1)}h_n^{(-)}(k_b r)\left[\left(\frac{n}{2n+1}\right)^{1/2}\mathbf{Y}_{n,n-1}^m + \left(\frac{n+1}{2n+1}\right)^{1/2}\mathbf{Y}_{n,n+1}^m\right]$$

$$N_{n,m}^{(-),2} = \left[(n+1)h_n^{(-)}(k_b r) - k_b r h_{n+1}^{(-)}(k_b r)\right]\left[\left(\frac{n+1}{2n+1}\right)^{1/2}\mathbf{Y}_{n,n-1}^m - \left(\frac{n}{2n+1}\right)^{1/2}\mathbf{Y}_{n,n+1}^m\right]$$

$$\begin{aligned} N_{n,m}^{(-),2} &= (n+1)h_n^{(-)}(k_b r)\left[\left(\frac{n+1}{2n+1}\right)^{1/2}\mathbf{Y}_{n,n-1}^m - \left(\frac{n}{2n+1}\right)^{1/2}\mathbf{Y}_{n,n+1}^m\right] \\ &\quad - k_b r h_{n+1}^{(-)}(k_b r)\left[\left(\frac{n+1}{2n+1}\right)^{1/2}\mathbf{Y}_{n,n-1}^m - \left(\frac{n}{2n+1}\right)^{1/2}\mathbf{Y}_{n,n+1}^m\right] \end{aligned}$$

$$\begin{aligned} N_{n,m}^{(-),1} + N_{n,m}^{(-),2} &= h_n^{(-)}(k_b r)\,\mathbf{Y}_{n,n-1}^m\left[\sqrt{n(n+1)}\left(\frac{n}{2n+1}\right)^{1/2} + (n+1)\left(\frac{n+1}{2n+1}\right)^{1/2}\right] \\ &\quad + h_n^{(-)}(k_b r)\,\mathbf{Y}_{n,n+1}^m\left[\sqrt{n(n+1)}\left(\frac{n+1}{2n+1}\right)^{1/2} - (n+1)\left(\frac{n}{2n+1}\right)^{1/2}\right] \\ &\quad - k_b r h_{n+1}^{(-)}(k_b r)\left[\left(\frac{n+1}{2n+1}\right)^{1/2}\mathbf{Y}_{n,n-1}^m - \left(\frac{n}{2n+1}\right)^{1/2}\mathbf{Y}_{n,n+1}^m\right] \end{aligned}$$

$$N_{n,m}^{(-),1}+N_{n,m}^{(-),2} = h_n^{(-)}(k_b r)\,\mathbf{Y}_{n,n-1}^m\sqrt{(n+1)(2n+1)} - k_b r h_{n+1}^{(-)}(k_b r)\left[\left(\frac{n+1}{2n+1}\right)^{1/2}\mathbf{Y}_{n,n-1}^m - \left(\frac{n}{2n+1}\right)^{1/2}\mathbf{Y}_{n,n+1}^m\right]$$

$$N_{n,m}^{(-),1}+N_{n,m}^{(-),2} = h_n^{(-)}(k_b r)\,\mathbf{Y}_{n,n-1}^m\sqrt{(n+1)(2n+1)} - k_b r h_{n+1}^{(-)}(k_b r)\left(\frac{n+1}{2n+1}\right)^{1/2}\mathbf{Y}_{n,n-1}^m + k_b r h_{n+1}^{(-)}(k_b r)\left(\frac{n}{2n+1}\right)^{1/2}\mathbf{Y}_{n,n+1}^m$$

$$h_{n+1}^{(-)}(k_b r) = \frac{2n+1}{k_b r}h_n^{(-)}(k_b r) - h_{n-1}^{(-)}(k_b r)$$

$$\begin{aligned} N_{n,m}^{(-),1} + N_{n,m}^{(-),2} &= h_n^{(-)}(k_b r)\,\mathbf{Y}_{n,n-1}^m\sqrt{(n+1)(2n+1)} \\ &\quad - k_b r\left[\frac{2n+1}{k_b r}h_n^{(-)}(k_b r) - h_{n-1}^{(-)}(k_b r)\right]\left(\frac{n+1}{2n+1}\right)^{1/2}\mathbf{Y}_{n,n-1}^m + k_b r h_{n+1}^{(-)}(k_b r)\left(\frac{n}{2n+1}\right)^{1/2}\mathbf{Y}_{n,n+1}^m \end{aligned}$$

$$N_{n,m}^{(-),1} + N_{n,m}^{(-),2} = k_b r h_{n-1}^{(-)}(k_b r)\left(\frac{n+1}{2n+1}\right)^{1/2}\mathbf{Y}_{n,n-1}^m + k_b r h_{n+1}^{(-)}(k_b r)\left(\frac{n}{2n+1}\right)^{1/2}\mathbf{Y}_{n,n+1}^m$$

$$\mathbf{N}_{nm}^{(-)}(k_b\mathbf{r}) = \frac{1}{k_b r}\left\{N_{n,m}^{(-),1} + N_{n,m}^{(-),2}\right\} = h_{n-1}^{(-)}(k_b r)\left(\frac{n+1}{2n+1}\right)^{1/2}\mathbf{Y}_{n,n-1}^m + h_{n+1}^{(-)}(k_b r)\left(\frac{n}{2n+1}\right)^{1/2}\mathbf{Y}_{n,n+1}^m$$

$$\begin{aligned} \mathbf{N}_{nm}^{(-)}(k_b\mathbf{r}) = \sum_{\mu=-1}^{1}\Bigg[&h_{n-1}^{(-)}(k_b r)\left(\frac{n+1}{2n+1}\right)^{1/2}(n-1, m-\mu; 1, \mu \mid n, m)Y_{n-1,m-\mu} \\ &+ h_{n+1}^{(-)}(k_b r)\left(\frac{n}{2n+1}\right)^{1/2}(n+1, m-\mu; 1, \mu \mid n, m)Y_{n+1,m-\mu}\Bigg]\boldsymbol{\chi}_\mu \end{aligned}$$

but

$$h_n^{(-)}(k_b r)\, Y_{nm}(\widehat{\mathbf{r}}) = \frac{(-1)^m}{2\pi(-i)^n k_b} \iint_{-\infty}^{\infty} dk_x dk_y\, Y_{nm}^*\left(\widehat{\mathbf{k}}\right) \frac{\exp\left(\mp i\mathbf{k}^*\cdot\mathbf{r}\right)}{k_z^*}$$

Assuming $m = 1$, we get

$$\mathbf{N}_{n1}^{(-)}(k_b\mathbf{r}) = \frac{i^{-n}}{2\pi(-1)^{n+1}k_b} \iint_{-\infty}^{\infty} dk_x dk_y \frac{\exp\left(\mp i\mathbf{k}^*\cdot\mathbf{r}\right)}{k_z^*}$$
$$\times \begin{bmatrix} \begin{bmatrix} i\left(\frac{n+1}{2n+1}\right)^{1/2}(n-1,2;1,-1\mid n,1)\, Y_{n-1,2}^*\left(\widehat{\mathbf{k}}\right) \\ -i\left(\frac{n}{2n+1}\right)^{1/2}(n+1,2;1,-1\mid n,1)\, Y_{n+1,2}^*\left(\widehat{\mathbf{k}}\right) \end{bmatrix}\boldsymbol{\chi}_{-1} \\ -\begin{bmatrix} i\left(\frac{n+1}{2n+1}\right)^{1/2}(n-1,1;1,0\mid n,1) Y_{n-1,1}^*\left(\widehat{\mathbf{k}}\right) \\ -i\left(\frac{n}{2n+1}\right)^{1/2}(n+1,1;1,0\mid n,1)\, Y_{n+1,1}^*\left(\widehat{\mathbf{k}}\right) \end{bmatrix}\boldsymbol{\chi}_0 \\ \begin{bmatrix} i\left(\frac{n+1}{2n+1}\right)^{1/2}(n-1,0;1,1\mid n,1)\, Y_{n-1,1}^*\left(\widehat{\mathbf{k}}\right) \\ -i\left(\frac{n}{2n+1}\right)^{1/2}(n+1,0;1,1\mid n,1)\, Y_{n+1,0}^*\left(\widehat{\mathbf{k}}\right) \end{bmatrix}\boldsymbol{\chi}_1 \end{bmatrix}$$

$$\mathbf{N}_{n1}^{(-)}(k_b\mathbf{r}) = \frac{1}{2\pi(-i)^{n+1}k_b} \int_0^{\infty}\int_0^{2\pi} KdKd\phi_k \frac{\exp\left(-iK.r_{//}\cos(\phi_k-\phi) - ik_z^*|z|\right)}{k_z^*}$$
$$\times \begin{bmatrix} \begin{bmatrix} -\left(\frac{n+1}{2n+1}\right)^{1/2}(n-1,2;1,-1\mid n,1)\, Y_{n-1,2}^*\left(\widehat{\mathbf{k}}\right) \\ +\left(\frac{n}{2n+1}\right)^{1/2}(n+1,2;1,-1\mid n,1)\, Y_{n+1,2}^*\left(\widehat{\mathbf{k}}\right) \end{bmatrix}\boldsymbol{\chi}_{-1} \\ -\begin{bmatrix} -\left(\frac{n+1}{2n+1}\right)^{1/2}(n-1,1;1,0\mid n,1) Y_{n-1,1}^*\left(\widehat{\mathbf{k}}\right) \\ +\left(\frac{n}{2n+1}\right)^{1/2}(n+1,1;1,0\mid n,1)\, Y_{n+1,1}^*\left(\widehat{\mathbf{k}}\right) \end{bmatrix}\boldsymbol{\chi}_0 \\ \begin{bmatrix} -\left(\frac{n+1}{2n+1}\right)^{1/2}(n-1,0;1,1\mid n,1)\, Y_{n-1,1}^*\left(\widehat{\mathbf{k}}\right) \\ +\left(\frac{n}{2n+1}\right)^{1/2}(n+1,0;1,1\mid n,1)\, Y_{n+1,0}^*\left(\widehat{\mathbf{k}}\right) \end{bmatrix}\boldsymbol{\chi}_1 \end{bmatrix}$$

$$Y_{n,m}^*(\theta,\phi) = c_{n,m}P_n^m([\cos\theta]^*)e^{-im\phi}$$

$$\mathbf{N}_{n1}^{(-)}(k_b\mathbf{r}) = \frac{1}{2\pi(-i)^{n+1}k_b} \int_0^{\infty}\int_0^{2\pi} KdKd\phi_k \frac{\exp\left(-iK.r_{//}\cos(\phi_k-\phi) - ik_z^*|z|\right)}{k_z^*}$$
$$\times \begin{bmatrix} \begin{bmatrix} -\left(\frac{n+1}{2n+1}\right)^{1/2}(n-1,2;1,-1\mid n,1)\, c_{n-1,2}P_{n-1}^2([\cos\theta_k]^*) \\ +\left(\frac{n}{2n+1}\right)^{1/2}(n+1,2;1,-1\mid n,1)\, c_{n+1,2}P_{n+1}^2([\cos\theta_k]^*) \end{bmatrix} e^{-i2\phi_k}\boldsymbol{\chi}_{-1} \\ -\begin{bmatrix} -\left(\frac{n+1}{2n+1}\right)^{1/2}(n-1,1;1,0\mid n,1) c_{n-1,1}P_{n-1}^1([\cos\theta_k]^*) \\ +\left(\frac{n}{2n+1}\right)^{1/2}(n+1,1;1,0\mid n,1)\, c_{n+1,1}P_{n+1}^1([\cos\theta_k]^*) \end{bmatrix} e^{-i\phi_k}\boldsymbol{\chi}_0 \\ \begin{bmatrix} -\left(\frac{n+1}{2n+1}\right)^{1/2}(n-1,0;1,1\mid n,1) c_{n-1,0}P_{n-1}^0([\cos\theta_k]^*) \\ +\left(\frac{n}{2n+1}\right)^{1/2}(n+1,0;1,1\mid n,1)\, c_{n+1,0}P_{n+1}^0([\cos\theta_k]^*) \end{bmatrix}\boldsymbol{\chi}_1 \end{bmatrix}$$

$$\int_0^{2\pi} \exp(-ix\cos(\phi_k-\phi))\exp(-in\phi_k)d\phi_k = 2\pi(-i)^n J_n(x)\exp(-in\phi)$$

$$\mathbf{N}_{n1}^{(-)}(k_b\mathbf{r}) = \frac{1}{(-i)^{n+1}k_b}\int_0^{\infty} KdK\frac{\exp\left(-ik_z^*|z|\right)}{k_z^*}$$
$$\times\begin{bmatrix} -J_2(K.r_{//})\begin{bmatrix} -\left(\frac{n+1}{2n+1}\right)^{1/2}(n-1,2;1,-1\mid n,1)\,c_{n-1,2}P_{n-1}^2(\frac{k_z}{k_b}^*) \\ +\left(\frac{n}{2n+1}\right)^{1/2}(n+1,2;1,-1\mid n,1)\,c_{n+1,2}P_{n+1}^2(\frac{k_z}{k_b}^*)\end{bmatrix}\frac{e^{-i2\phi}}{\sqrt{2}}\{\widehat{\mathbf{x}}-\widehat{\mathbf{iy}}\} \\ iJ_1(K.r_{//})\begin{bmatrix} -\left(\frac{n+1}{2n+1}\right)^{1/2}(n-1,1;1,0\mid n,1)c_{n-1,1}P_{n-1}^1(\frac{k_z}{k_b}^*) \\ +\left(\frac{n}{2n+1}\right)^{1/2}(n+1,1;1,0\mid n,1)\,c_{n+1,1}P_{n+1}^1(\frac{k_z}{k_b}^*)\end{bmatrix}e^{-i\phi}\widehat{\mathbf{z}} \\ -J_0(K.r_{//})\begin{bmatrix} -\left(\frac{n+1}{2n+1}\right)^{1/2}(n-1,0;1,1\mid n,1)c_{n-1,0}P_{n-1}^0(\frac{k_z}{k_b}^*) \\ +\left(\frac{n}{2n+1}\right)^{1/2}(n+1,0;1,1\mid n,1)\,c_{n+1,0}P_{n+1}^0(\frac{k_z}{k_b}^*)\end{bmatrix}\frac{1}{\sqrt{2}}\{\widehat{\mathbf{x}}+\widehat{\mathbf{iy}}\}\end{bmatrix}$$

B.2.4 Regular waves

B.2.4.1 Magnetic regular waves

$$Rg\{\mathbf{M}_{n,1}(k_b\mathbf{r})\} = \frac{1}{2}\left[\mathbf{M}_{n1}^{(+)}(k_b\mathbf{r}) + \mathbf{M}_{n1}^{(-)}(k_b\mathbf{r})\right]$$

B.2.4.2 Electric regular waves

$$Rg\{\mathbf{N}_{n,1}(k_b\mathbf{r})\} = \frac{1}{2}\left[\mathbf{N}_{n1}^{(+)}(k_b\mathbf{r}) + \mathbf{N}_{n1}^{(-)}(k_b\mathbf{r})\right]$$

Appendix C

Spontaneous emission in the multipolar framework

C.1 Introduction

The nanoscale structuration of the near field of a single emitter such as fluorescent molecules or quantum dots can strongly modify its radiation properties i) the total decay rate enhancement Γ_{tot}, ii) the radiative decay rate enhancement Γ_{tot} iii) the quantum efficiency η iv) the directionality. This quantities are related to the emitted power and the radiative power. A basic way to acces this physical quantities is to integrate the Poynting vector over a surface surrounding the isolated dipole to obtain the total emitted power and the whole structure to calculate the electromagnetic power radiated in the far field. In the case of spherical particles, the decay rates enhancements and the quantum efficiency can be analytically calculated by a matricial approach. In this appendix, we demonstrate a multipole formalism for the direct calculation of the radiative properties of a single dipolar emitter. This approach enables fast calculations of dipolar emission for different positions in the aggregate.

C.2 Power emitted by a point dipole source

The time average power emitted by a point dipole is

$$\langle P_e \rangle_\omega = \frac{\omega}{2} \mathrm{Im}\{\mathbf{E}_0(\mathbf{x}_j).\mathbf{p}_0^*(\mathbf{x}_j)\} \tag{C.1}$$

For a homogeneous medium decribed by a dielectric constant ε_b,we have:

$$\nabla \times (\nabla \times \mathbf{E}) - k_b^2 \mathbf{E} = i\omega\mu_0 \mathbf{j}_{src} \tag{C.2}$$

where $k_b = \frac{2\pi\varepsilon_b}{\lambda_0}$ is the wavevector in the homogeneous background medium.
We can solve the equation for any arbitrary source current

$$\nabla \times (\nabla \times \overleftrightarrow{\mathbf{G}}_0(\mathbf{r}, \mathbf{r}')) - k_b^2 \overleftrightarrow{\mathbf{G}}_0(\mathbf{r}, \mathbf{r}') = \boldsymbol{\delta}^3(\mathbf{r} - \mathbf{r}') \overleftrightarrow{\mathbb{I}} \tag{C.3}$$

The solution electric field created by a source current in a homogeneous medium can be readily formulated in terms of the Green function

$$\mathbf{E}_0(\mathbf{r}) = i\omega\mu_0 \int d\mathbf{r}' \overleftrightarrow{\mathbf{G}}_0(\mathbf{r}, \mathbf{r}') \mathbf{j}_{src}(\mathbf{r}') \tag{C.4}$$

For our point source

$$\mathbf{j}_j(\mathbf{r}') = -i\omega\mathbf{p}\delta^3(\mathbf{r}' - \mathbf{r}_j) \tag{C.5}$$

we have

$$\mathbf{E}_0(\mathbf{r}) = \omega^2\mu_0 \overleftrightarrow{\mathbf{G}}_0(\mathbf{r}_j, \mathbf{r}_j).\mathbf{p}(\mathbf{r}_j) \tag{C.6}$$

The power emitted by a dipole source is

$$\langle P_e \rangle_\omega = \frac{\omega}{2}\,\mathrm{Im}\{\mathbf{p}^*(\mathbf{r}_j).\mathbf{E}(\mathbf{r}_j)\} \tag{C.7}$$

$$\langle P_e \rangle_\omega = \frac{\omega^3\mu_0}{2}\,\mathrm{Im}\{\mathbf{p}^*(\mathbf{r}_j).\overleftrightarrow{\mathbf{G}}(\mathbf{r}_j, \mathbf{r}_j).\mathbf{p}(\mathbf{r}_j)\} \tag{C.8}$$

C.3 Green function in the multipole framework

The Green function can be expressed in terms of multipole waves

$$\overleftrightarrow{\mathbf{G}}_0(\mathbf{r}, \mathbf{r}') = ik_b \sum_{n=1}^{\infty}\sum_{m=-n}^{n} \mathbf{M}_{n,m}(k_b r)Rg\{\widetilde{\mathbf{M}}_{n,m}(k_b r')\} + \mathbf{N}_{n,m}(k_b r)Rg\{\widetilde{\mathbf{N}}_{n,m}(k_b r')\} - \frac{\mathbf{rr}}{k_0^2}\delta^3(r - r') \tag{C.9}$$

Where we supposed that $|r'|^2 < |r|^2$ and $\widetilde{\mathbf{M}}_{n,m}$ and $\widetilde{\mathbf{N}}_{n,m}$ are defined as:

$$\begin{aligned}\widetilde{\mathbf{M}}_{n,m} &\equiv \frac{1}{kr}\{\sqrt{2}j_n(kr)\widehat{\mathbf{r}}Y^*_{n,m}(\widehat{\mathbf{r}}) + [krj_n(kr)]'\mathbf{Z}^*_{n,m}(\widehat{\mathbf{r}})\} \\ \widetilde{\mathbf{N}}_{n,m} &\equiv j_n(kr)\mathbf{X}^*_{n,m}(\widehat{\mathbf{r}})\end{aligned} \tag{C.10}$$

We chose that the origin lies at r'

$$\overleftrightarrow{\mathbf{G}}_0(\mathbf{r}, \mathbf{0}) = ik_b \sum_{n=1}^{\infty}\sum_{m=-n}^{n} \mathbf{M}_{n,m}(k_b r)Rg\{\widetilde{\mathbf{M}}_{n,m}(k_b, 0)\} + \mathbf{N}_{n,m}(k_b r)Rg\{\widetilde{\mathbf{N}}_{n,m}(k_b; 0)\} - \frac{\mathbf{rr}}{k_0^2}\delta^3(r) \tag{C.11}$$

$$= ik_b \sum_{m=-n}^{n} \mathbf{N}_{1,m}(k_b r)Rg\{\widetilde{\mathbf{N}}_{1,m}(k_b; 0)\} \tag{C.12}$$

$$\mathbf{E}_0(\mathbf{r}) = \omega^2\mu_0 \overleftrightarrow{\mathbf{G}}_0(\mathbf{r}_j, \mathbf{r}_j).\mathbf{p}(\mathbf{r}_j) \tag{C.13}$$

$$\mathbf{E}_0(\mathbf{r}) = \omega^2\mu_0 ik_b \sum_{m=-1}^{1} \mathbf{N}_{1,m}(k_b r)Rg\{\widetilde{\mathbf{N}}_{1,m}(k_b; 0)\}.\widehat{\mathbf{n}}.p \tag{C.14}$$

$$f_{1,m} = \omega^2\mu_0 ik_b Rg\{\widetilde{\mathbf{N}}_{1,m}(k_b; 0)\}.\widehat{\mathbf{n}} \tag{C.15}$$

In spherical coordinates, we get

$$Rg\{\widetilde{\mathbf{N}}_{1,0}(\mathbf{0})\} = \frac{1}{\sqrt{6\pi}}\widehat{\mathbf{r}} \tag{C.16}$$

$$Rg\{\widetilde{\mathbf{N}}_{1,1}(\mathbf{0})\} = \frac{1}{2\sqrt{3\pi}}(-\widehat{\boldsymbol{\theta}} + i\widehat{\boldsymbol{\phi}}) \tag{C.17}$$

$$Rg\{\widetilde{\mathbf{N}}_{1,-1}(\mathbf{0})\} = \frac{1}{2\sqrt{3\pi}}(\widehat{\boldsymbol{\theta}} + i\widehat{\boldsymbol{\phi}}) \tag{C.18}$$

$$\mathbf{E}_0(\mathbf{r}) = p\sum_{m=-1}^{1}\mathbf{N}_{1,m}(k_b r).f_{1,m} \tag{C.19}$$

C.3.1 Multipole formulation for the emitted power

$$\langle P_e\rangle_\omega = \frac{\omega}{2}\,\mathrm{Im}\{\mathbf{p}^*(\mathbf{r}_j).\mathbf{E}(\mathbf{r}_j)\} \tag{C.20}$$

$$\lim_{kr\to 0^+}\mathbf{N}_{1,0}(kr) = \frac{1}{\sqrt{6\pi}}\widehat{\mathbf{r}} \tag{C.21}$$

$$\lim_{kr\to 0^+}\mathbf{N}_{1,1}(kr) = \frac{1}{4\sqrt{3\pi}}(\widehat{\boldsymbol{\theta}} + i\widehat{\boldsymbol{\phi}}) \tag{C.22}$$

$$\lim_{kr\to 0^+}\mathbf{N}_{1,-1}(kr) = \frac{1}{4\sqrt{3\pi}}(\widehat{\boldsymbol{\theta}} - i\widehat{\boldsymbol{\phi}}) \tag{C.23}$$

The power emitted in the homogeneous medium is

$$\langle P_{e,0}\rangle_\omega = \frac{\omega}{2}\,\mathrm{Im}\{\mathbf{p}^*(\mathbf{r}_j).\mathbf{E}_0(\mathbf{r}_j)\} \tag{C.24}$$

$$\langle P_{e,0}\rangle_\omega = \frac{\omega^3\mu_0}{2}|p|^2\,\mathrm{Re}\{k_b\sum_{m=-1}^{1}\mathbf{N}_{1,m}(\mathbf{0}^+).f_{1,m}\} \tag{C.25}$$

$$\langle P_{e,0}\rangle_\omega = \frac{\omega^3\mu_0}{12\pi}|p|^2\,\mathrm{Re}\{k_b\} \tag{C.26}$$

The power emitted in presence of the nanoparticles is

$$\langle P_e\rangle_\omega = \langle P_{e,0}\rangle_\omega + \frac{\omega^3\mu_0}{2}|p|^2\,\mathrm{Re}\left\{k_b\sum_{j,l=1}^{N_p}f^\dagger H^{(0,j)}T^{(j,l)}H^{(j,0)}f\right\} \tag{C.27}$$

where $H^{(j,0)}$and $H^{(0,j)}$ are the irregular translation/addition martix and $T = \left[T^{(i,j)}\right]$ is the transfert matrix of the agregate of particles.

The radiative decay rate enhancement is then

$$\frac{\langle\Gamma_e\rangle_\omega}{\langle\Gamma_{e,0}\rangle_\omega} = 1 + \frac{6\pi}{\mathrm{Re}\{k_b\}}\,\mathrm{Re}\left\{k_b\sum_{j,l=1}^{N_p}f^\dagger H^{(0,j)}T^{(j,l)}H^{(j,0)}f\right\} \tag{C.28}$$

C.4 Multipole formulation for the radiated power

In the far field domain, the Poynting vector $\mathbf{S}$ can be expressed

$$\lim_{kr\to\infty} \mathbf{S} = \frac{1}{2}\frac{k_b}{\omega\mu_0}\,\mathrm{Re}\left\{\widehat{\mathbf{r}}.(\mathbf{E}.\mathbf{E}^*)\right\} \tag{C.29}$$

$$\lim_{kr\to\infty} \mathbf{M}_{n,m}(kr) = i^n \frac{\exp(ikr)}{ikr}\mathbf{X}^*_{n,m}(\widehat{\mathbf{k}}) \tag{C.30}$$

$$\lim_{kr\to\infty} \mathbf{N}_{n,m}(kr) = i^{n-1} \frac{\exp(ikr)}{ikr}\mathbf{Z}^*_{n,m}(\widehat{\mathbf{k}}) \tag{C.31}$$

One finds the radiated power in free space as

$$\langle P_{r,0}\rangle_\omega = \frac{1}{2}\frac{k_b}{\omega\mu_0}\int \mathbf{E}_0.\mathbf{E}_0^* d\Omega \tag{C.32}$$

$$\mathbf{E}_0(\mathbf{r}) = p\sum_{m=-1}^{1}\mathbf{N}_{1,m}(k_b r).f_{1,m} = p\frac{\exp(ikr)}{ikr}\sum_{m=-1}^{1}\mathbf{Z}^*_{1,m}(\widehat{\mathbf{k}})f_{1,m} \tag{C.33}$$

$$\langle P_{r,0}\rangle_\omega = \frac{1}{2}\frac{k_b}{\omega\mu_0}\int p\frac{\exp(ikr)}{ikr}\sum_{m=-1}^{1}\mathbf{Z}^*_{1,m}(\widehat{\mathbf{k}})f_{1,m}.\left[p\frac{\exp(ikr)}{ikr}\sum_{m=-1}^{1}\mathbf{Z}^*_{1,m}(\widehat{\mathbf{k}})f_{1,m}\right]^* d\Omega \tag{C.34}$$

$$= \frac{1}{2}\frac{k_b}{\omega\mu_0}|p|^2\int\frac{\omega^4\mu_0^2}{r^2}\sum_{m=-1}^{1}\mathbf{Z}^*_{1,m}(\widehat{\mathbf{k}})Rg\{\widetilde{\mathbf{N}}_{1,m}(k_b;0)\}.\widehat{\mathbf{n}}.\left[\sum_{m=-1}^{1}\mathbf{Z}^*_{1,m}(\widehat{\mathbf{k}})Rg\{\widetilde{\mathbf{N}}_{1,m}(k_b;0)\}.\widehat{\mathbf{n}}\right]^* d\Omega \tag{C.35}$$

$$\langle P_{r,0}\rangle_\omega = |p|^2\frac{\omega^3\mu_0}{12\pi}k_b \tag{C.36}$$

The total electric field is given as the sum of the dipole field $\mathbf{E}_0$ and the scattered field $\mathbf{E}_s$

$$\mathbf{E}(\mathbf{r}) = \mathbf{E}_0 + \mathbf{E}_s \tag{C.37}$$

$$= p\sum_{m=-1}^{1}\mathbf{N}_{1,m}(k_b r).f_{1,m} + \mathbf{E}_0(\mathbf{r}) \tag{C.38}$$

$$= p\sum_{m=-1}^{1}\mathbf{N}_{1,m}(k_b r).f_{1,m} + p\sum_{m=-1}^{1}\sum_{j,l=1}^{N_p}\left[\mathbf{N}_{1,m}(k_b r_j),\mathbf{M}_{1,m}(k_b r_j)\right].T^{(j,l)}H^{(l,0)}f_{1,m} \tag{C.39}$$

$$\mathbf{E}_s = p\sum_{m=-1}^{1}\sum_{j,l=1}^{N_p}\left[\mathbf{N}_{1,m}(k_b 0),\mathbf{M}_{1,m}(k_b 0)\right]J^{(0,j)}.T^{(j,l)}H^{(l,0)}f_{1,m} \tag{C.40}$$

$$\frac{\langle\Gamma_r\rangle_\omega}{\langle\Gamma_{r,0}\rangle_\omega} = \left\{\begin{array}{c} 1+6\pi\displaystyle\sum_{i,j,k,l=1}^{N_p}\left[T^{(i,j)}.H^{(i,0)}.f\right]^\dagger.J^{(j,k)}.T^{(k,l)}.H^{(l,0)}.f \\ +12\pi\,\mathrm{Re}\left\{\displaystyle\sum_{j,k=1}^{N_p} f^\dagger.J^{(0,k)}.T^{(k,j)}.H^{(j,k)}.f\right\}\end{array}\right\} \tag{C.41}$$

Bibliography

[1] B. Stout, J. C. Auger, and A. Devilez, "Recursive T-matrix algorithm for resonant multiple scattering: applications to localized plasmon excitation," J. Opt. Soc. Am. A **25**, 2549–2557 (2008). 1, 54, 75

[2] A. Devilez, B. Stout, N. Bonod, and E. Popov, "Spectral analysis of three-dimensional photonic jets," Opt. Express **16**, 14200 – 14212 (2008). 1, 2, 28

[3] B. Stout, A. Devilez, B. Rolly, and N. Bonod, "Multipole methods for nanoantennas design: applications to Yagi-Uda configurations," J. Opt. Soc. Am. A (in preparation). 1, 56

[4] P. Ferrand, J. Wenger, M. Pianta, H. Rigneault, A. Devilez, B. Stout, N. Bonod, and E. Popov, "Direct imaging of photonic nanojet," Opt. Express **16**, 6930–6940 (2008). 2, 19

[5] D. Gérard, A. Devilez, H. Aouani, B. Stout, N. Bonod, J. Wenger, E. Popov, and H. Rigneault, "Efficient excitation and collection of single molecule fluorescence close to a dielectric microspheres," J. Opt. Soc. Am. B. **26**, 1473–1478 (2009). 2, 36, 47, 49, 85, 90

[6] D. Gérard, J. Wenger, A. Devilez, D. Gachet, B. Stout, N. Bonod, E. Popov, and H. Rigneault, "Strong electromagnetic confinement near dielectric microspheres to enhance single-molecule fluorescence," Opt. Express **16**, 15297–15303 (2008). 2, 47, 49

[7] A. Devilez, N. Bonod, J. Wenger, D. Gérard, B. Stout, H. Rigneault, and E. Popov, "Three-dimensional subwavelength confinement of light with dielectric microspheres," Opt. Express **17**, 2089 (2009). 2, 36, 38, 90

[8] A. Devilez, J. Wenger, B. Stout, and N. Bonod, "Transverse and longitudinal confinement of photonic nanojets by compound dielectric microspheres," Proc. of SPIE **7393**, 7393E–1–9 (2009). 2, 39

[9] A. Devilez, B. Stout, and N. Bonod, "Mode-balancing far field control of light localization in nanoantennas," Phys. Rev. B **81**, 245128 (2010). 2, 61, 62

[10] N. Bonod, A. Devilez, B. Rolly, S. Bidault, and B. Stout, "Ultracompact and unidirectional metallic antennas," Phys. Rev. B (in press). 2, 75, 82, 83

[11] A. Devilez, B. Stout, and N. Bonod, "Compact metallo-dielectric optical antenna for ultra directional and enhanced radiative emission," ACS NANO **4**, 3390–3396 (2010). 2, 74

[12] H. C. van de Hulst, *Light Scattering by Small Particles* (Dover Publication, Inc., 1981). 3

[13] F. Vollmer, D. Braun, A. Libchaber, M. Khoshsima, I. Teraoka, and S. Arnold, "Protein detection by optical shift of a resonant microcavity," Appl. Phys. Lett. **80**, 4057–4059 (2002). 5, 13

[14] C. G. B. Garret, W. Kaiser, and W. L. Bond, "Stimulated emission into optical whispering modes of spheres," Phys. Rev. **124**, 1807–1809 (1961). 5, 13

[15] Y. Hara, T. Mukaiyama, K. Takeda, and M. Kuwata-Gonokami, "Photonic molecule lasing," Optics Letters **28**, 2437–2439 (2003). 5, 13

[16] A. Yariv, Y. Xu, R. K. Lee, and A. Scherer, "Coupled-resonator optical waveguide: a proposal and analysis," Opt. Lett. **24**, 711–713 (1999). 5, 13

[17] J. D. Jackson, *Classical electrodynamics, second edition* (Wiley, 1975), chap. Multipole fields, pp. 739–779. 5, 11

[18] L. W. Davis, "Theory of electromagnetic beams," Phys. Rev. A **19**, 1177–1179 (1978). 12, 36

[19] G. Gouesbet, J. A. Lock, and G. Gréhan, "Partial-wave representations of laser beams for use in light-scattering calculations," Appl. Opt. **34**, 2133–2143 (1995). 12

[20] J. A. Lock, J. T. Hodges, and G. Gousebet, "Failure of the optical theorem for gaussian-beam scattering by a spherical-particle," Journal of the Optical Society of America A-optics Image Science and Vision **12**, 2708–2715 (1995).

[21] G. Gouesbet and G. Gréhan, "Generalized Lorentz-Mie theories, from past to future," Atomization and sprays **10**, 277–333 (2000). 12

[22] C. J. R. Sheppard and S. Saghafi, "Electromagnetic Gaussian beams beyond the paraxial approximation," J. Opt. Soc. Am. A **16**, 1381–1386 (1999). 12, 36

[23] B. Richards and E. Wolf, "Electromagnetic diffraction in optical systems. II. structure of the image field in an aplanetic system," Proc. R. Soc. Lond. A **253**, 358–379 (1959). 12, 36

[24] M. L. Gorodestsky, A. A. Savchenkov, and V. S. Ilchenko, "Ultimate Q of optical microsphere resonators," Opt. Lett. **21**, 453–455 (1996). 13, 90

[25] A. Chiasera, Y. Dumeige, P. Feron, M. Ferrari, Y. Jestin, G. N. Conti, S. Pelli, S. Soria, and G. C. Righini, "Spherical whispering-gallery-mode microresonators," Laser & photonic reviews **4**, 457–482 (2010). 13

[26] S. Deng, W. Cai, and V. N. Astratov, "Numerical study of light propagation via whispering gallery modes in microcylinders coupled resonator optical waveguides," Opt. Express **12**, 6468–6480 (2004). 13

[27] V. N. Astratov, J. P. Franchak, and S. P. Ashili, "Optical coupling and transport phenomena in chains of spherical dielectric microresonators with size disorder," Appl. Phys. Lett. **85**, 5508–5510 (2004). 13

[28] J. K. S. Poon, J. Scheuer, Y. Xu, and A. Yariv, "Designing coupled-resonator optical waveguide delay lines," J. Opt. Soc. Am. B **21**, 1665–1673 (2004). 13

[29] C. C. Lam, P. T. Leung, and K. Young, "Explicit asymptotic formulas for the position, widths and strengths in resonances in Mie scattering," J. Opt. Soc. Am. B **9**, 1585–1592 (1992). 14, 15

[30] B. R. Johnson, "Theory of morphology-dependent resonances: Shape resonances and width formulas," J. Opt. Soc. Am. A **10**, 243–352 (1992). 14, 90

[31] M. Born and E. Wolf, *Principles of Optics* (Pergamon Press, 1986), chap. Geometrical theory of optical imaging, pp. 133–202. 18, 23, 31

[32] M. Born and E. Wolf, *Principles of Optics* (Pergamon Press, 1986), chap. The diffraction theory of aberrations, pp. 459–490. 18

[33] B. S. Luk'yanchuk, N. Arnold, S. M. Huang, Z. B. Wang, and M. H. Hong, "Three-dimensional effects in dry laser cleaning," Appl. phys. A **77**, 209–215 (2003). 19

[34] D. Grojo, P. Delaporte, and A. Cros, "Removal of particles by impulsional laser," Journal de Physique IV **127**, 145–149 (2005). 19

[35] S. M. Huang, M. H. Hong, B. Luk'yanchuk, and T. C. Chong, "Nanostructures fabricated on metal surfaces assisted by laser with optical near-field effects," Appl. Phys. A: Mater. Sci. Process. **77**, 293–296 (2003). 19

[36] W. Guo, Z. B. Wuang, L. Li, D. J. Whitehead, B. Luk'yanchuk, and Z. Liu, "Near-field laser parallel nanofabrication of arbitrary-shaped patterns," Appl. Phys. Lett. **90**, 243101 (2007). 19

[37] Z. Chen, A. Taflove, and V. Backman, "Photonic nanojet enhancement of backscattering of light by nanoparticles: A potential novel visible-light ultramicroscopy technique," Opt. Express **12**, 1214–1220 (2004). 19, 20

[38] X. Li, Z. Chen, A. Taflove, and V. Backman, "Optical analysis of nanoparticles via enhanced backscattering facilitated by 3-D photonic nanojets," Opt. Express **13**, 526–533 (2005). 19

[39] Z. Chen, A. Taflove, X. Li, and V. Backman, "Superenhanced backscattering of light by nanoparticles," Opt. Lett. **31**, 194–198 (2006). 19

[40] A. Heifetz, K. Huang, A. V. Sahakian, X. Li, A. Taflove, and V. Backman, "Experimental confirmation of backscattering enhancement induced by a photonic jet," Appl. Phys. Lett. **89**, 221118 (2006). 19

[41] S. Lecler, S. Haache, N. Lecong, O. Crégut, J. L. Rehspringer, and C. Hirlimann, "Photonic jet driven non-linear optics: Example of two-photon fluorescence enhancement by dielectric microspheres," Opt. Express **15**, 4935–4942 (2007). 19, 20

[42] S. Lecler, Y. Takakura, and P. Meyrueis, "Properties of a 3D photonic jet," Opt. Lett. **30**, 2641–2643 (2005). 19

[43] K. J. Yi, H. Wang, Y. F. Lu, and Z. Y. Yang, "Enhanced Raman scattering by self-assembled silica spherical microparticles," J. Appl. Phys. **101**, 063528 (2007). 19

[44] S.-C. Kong, A. Sahahkian, A. Taflove, and V. Backman, "Photonic nanojet-enabled optical data storage," Opt. Express **16**, 13713–13719 (2008). 19

[45] S. Li, C. Du, X. Dong, L. Shi, X. Luo, X. Wei, and Y. Zhang, "Superlens nano-patterning technology based on the distributed polystyrene spheres," Opt. Express **16**, 14397–14403 (2008). 19

[46] E. McLeod and C. B. Arnold, "Subwavelength direct-write nanopatterning using optically trapped microspheres," Nature Nanotechnol. **3**, 413–417 (2008). 20, 35

[47] A. V. Itagi and W. A. Challener, "Optics of photonic nanojets," J. Opt. Soc. Am. A **22**, 2847–2858 (2005). 20, 28

[48] J. Durnin, "Exact solution for nondiffracting beams. I. The scalar theory," J. Opt. Soc. Am. A **4**, 651–654 (1986). 29

[49] R. M. Herman and T. A. Wiggins, "Production and uses of diffractionless beams," J. Opt. Soc. Am. A **8**, 932–942 (1991). 30

[50] J. D. Jackson, *Classical electrodynamics* (Wiley, 1999), chap. Boundary-value problem in electrostatic: II, pp. 95–144. 30

[51] J. Durnin, J. Miceli, J. J., and J. H. Eberly, "Diffraction-free beams," Phys. Rev. Lett. **58**, 1499–1501 (1987). 30

[52] M. Born and E. Wolf, *Principles of Optics* (Pergamon Press, 1986), chap. Element of the Theory of Diffraction, pp. 370–458. 30, 103, 104, 108, 109, 111

[53] V. Garcés-Chávez, D. McGloin, H. Melville, W. Sibbett, and K. Dholakia, "Simultaneous micromanipulation in multiple planes using a self-reconstructing light beam," Nature **419**, 145–147 (2002). 31

[54] S.-C. Kong, A. Taflove, and V. Backman, "Quasi one-dimensional light beam generated by a graded-index microsphere," Opt. Express **17**, 3722–3731 (2009). 32

[55] K. Li, M. I. Stockman, and D. J. Bergman, "Self-similar chain of metal nanospheres as an efficient nanolens," Phys. Rev. Lett. **91**, 227402 (2003). 44, 52, 57, 63, 69

[56] H. Rigneault, J. Capoulade, J. Dintinger, J. Wenger, N. Bonod, E. Popov, T. W. Ebbesen, and P. F. Lenne, "Enhancement of single-molecule fluorescence detection in subwavelength apertures," Phys. Rev. Lett. **96**, 117401 (2005). 47, 48, 69

[57] R. W. Wood, "On a remarkable case of uneven distribution of light in a diffraction grating spectrum," Philos. Mag. **4**, 396–402 (1902). 51

[58] K. Kneipp, H. Wang, Y. Kneipp, L. T. Perelman, I. Itzkan, R. Dasari, and M. S. Feld, "Single molecule detection using surface-enhanced Raman scattering (SERS)," Phys. Rev. Lett. **78**, 1667–1670 (1997). 51

[59] W. Rechberger, A. Hohenau, A. Leitner, J. R. Krenn, B. Lamprecht, and F. R. Aussenegg, "Optical properties of two interacting gold nanoparticles," Opt. Commun. **220**, 137–141 (2003). 52, 57, 59, 63, 69, 91

[60] D. J. Bergman and D. Strout, "Theory of resonances in the electromagnetic scattering by macroscopic bodies," Phys. Rev. B **22**, 3527 (1980).

[61] H. Tamaru, H. Kuwata, H. T. Miyazaki, and K. Miyano, "Resonant light scattering from individual Ag nanoparticles and particle pairs," Appl. Phys. Lett. **80**, 1826 (2002). 69

[62] P. Nordlander, C. Ourbe, E. Prodan, K. Li, and M. I. Stockman, "Plasmon hybridization in nanoparticle dimers," Nano Lett. **4**, 899–903 (2004). 52, 58

[63] J. B. Lassiter, J. Aizpurua, L. I. Hernandez, D. W. Brandl, I. Romero, S. Lal, J. H. Hafner, P. Nordlander, and N. J. Halas, "Close encounter between two nanoshells," Nano Lett. **8**, 1212–1218 (2008).

[64] S.-C. Yang, H. Kobori, C.-H. He, M.-H. Lin, H.-Y. Chen, C. Li, M. Kanehara, T. Teranishi, and S. Gwo, "Plasmon hybridization in individual gold nanocrystal dimers: direct observation of bright and dark modes," Nano Lett. **10**, 632–637 (2010). 52, 57, 63

[65] S. Bidault, F. J. García de Abajo, and A. Polman, "Plasmon-based nanolenses assembled on a well-defined DNA template," J. Am. Chem. Soc **130**, 2750–2751 (2008). 52, 69, 80, 92

[66] L. Rogobete, F. Kaminski, M. Agio, and V. Sandoghdar, "Design of plasmonic nanoantennae for enhancing spontaneous emission," Opt. Lett. **32**, 1623–1625 (2007). 52, 69, 91

[67] H. Mertens, A. F. Koenderink, and A. Polman, "Plasmon-enhanced luminescence near noble-metal nanospheres: Comparison of exact theory and an improved Gersten and Nitzan model," Phys. Rev. B **76**, 115123 (2007). 52, 69, 70

[68] E. Prodan, C. Radloff, N. J. Halas, and P. Nordlander, "A hybridization model for the plasmon response of complex nanostructures," Science **302**, 419–422 (2003). 52, 57, 58

[69] E. D. Palik, *Handbook of optical constants of solids* (Academic Press, New York, 1985). 52, 60, 76, 89, 92

[70] G. Mie, Ann. phys. **25**, 377 (1908). 52

[71] M. Born and E. Wolf, *Principles of Optics* (Pergamon Press, 1986), chap. Optics of Metals, pp. 611–614. 52

[72] J. D. Jackson, *Classical electrodynamics, Second Edition* (Wiley, 1975), chap. Simple radiating systems,scattering and diffraction, pp. 391–468. 55

[73] J. D. Jackson, *Classical electrodynamics, second edition* (Wiley, 1975), chap. Multipoles, electrotatics of Macroscopic Media, Dielectrics, pp. 136–167. 55

[74] M. Meier and A. Wokaun, "Enhanced fields on large metal particles: dynamic depolarization," Opt. Lett. **8**, 581–583 (1983). 56

[75] A. F. Koenderink and A. Polman, "Complex response and polariton-like dispersion splitting in periodic metal nanoparticle chains," Phys. Rev. B **74**, 033402 (2006). 56, 88

[76] G. Volpe, S. Cherukulappurath, R. J. Parramon, G. Molina-Terriza, and R. Quidant, "Controlling the optical near field of nanoantennas with spatial phase-shaped beams," Nano Lett. **9**, 3608 (2009). 61, 62

[77] M. I. Stockman, S. V. Faleev, and D. J. Bergman, "Coherent control of femtosecond energy localization in nanosystems," Phys. Rev. Lett. **88**, 067402 (2002). 61

[78] M. Aeschlimann, M. Bauer, D. Bayer, T. Brixner, F. J. García de Abajo, W. Pfeiffer, M. Rohmer, C. Spindler, and F. Steeb, "Adaptative subwavelength control of nano-optical fields," Nature **446**, 301 (2007). 61

[79] A. F. Koenderink, J. V. Hernandez, F. Rochibeaux, L. D. Noordam, and A. Polman, "Programmable nanolithography with plasmon nanoparticle arrays," Nano Lett. **7**, 745–749 (2007). 61

[80] J. Le Perchec, P. Quémerais, A. Barbara, and T. Lopez-Rios, "Controlling strong electromagnetic fields at subwavelength scales," Phys. Rev. Lett. **97**, 036405 (2006). 62

[81] M. Quinten and U. Kreibig, "Absorption and elastic scattering of light by particle aggregates," Appl. Opt. **32**, 6137 (1993). 64

[82] S. Zhang, D. A. Genov, Y. Wang, M. Liu, and X. Zhang, "Plasmon-induced transparency in metamaterials," Phys. Rev. Lett. **101**, 047401 (2008). 65

[83] N. Verellen, Y. Sonnefraud, H. Sobhani, F. Hao, V. V. Moshchalkov, P. V. Dorpe, and S. M. P. Nordlander, "Fano resonances in individual coherent plasmonic nanocavities," Nano Lett. **9**, 1663 (2009). 65

[84] D. Gérard, J. Wenger, H. Rigneault, F. Mahdavi, S. Blair, J. Dintinger, and T. W. Ebbesen, "Nanoaperture-enhanced fluorescence: Towards higher detection rates with plasmonic metals," Phys. Rev. B **77**, 045413 (2008). 69

[85] N. Bonod, E. Popov, D. Gérard, J. Wenger, and H. Rigneault, "Field enhancement in a circular aperture surrounded by a single channel groove," Opt. Express **16**, 2276–2287 (2008).

[86] A. Kinkhabwala, Z. Yu, S. Fan, Y. Avlasevich, K. Müllen, and W. E. Moerner, "Large single-molecule fluorescence enhancements produced by a bowtie nanoantenna," Nat. Photon. **3**, 654–657 (2009). 91

[87] J.-W. Liaw, J.-S. Chen, and J.-H. Chen, "Enhancement and quenching effect of metallic nanodimer on spontaneous emission," J. Quant. Spectrosc. Radiat. Transf. **111**, 454–465 (2010). 69, 91

[88] J. N. Farahani, D. W. Pohl, H.-J. Eisler, and B. Hecht, "Single quantum dot coupled to a scanning optical antenna: a tunable superemitter," Phys. Rev. Lett. **95**, 017402 (2005). 69, 74, 88, 91

[89] P. Anger, P. Bharadwaj, and L. Novotny, "Enhancement and quenching of single-molecule fluorescence," Phys. Rev. Lett. **96**, 113002 (2006). 73

[90] R. Carminati, J.-J. Greffet, C. Henkel, and J. M. Vigoureux, "Radiative and non-radiative decay of single molecule close to a metallic nanoparticle," Opt. Commun. **261**, 368–375 (2006).

[91] Y. Chen, K. Munechika, and D. S. Ginger, "Dependence of fluorescence intensity on the spectral overlap between fluorophores and plasmon resonant single silver nanoparticles," Nano Lett. **7**, 690–696 (2007).

[92] G. Colas des Francs, A. Bouhelier, E. Finot, J. C. Weeber, A. Dereux, and E. Dujardin, "Fluorescence relaxation in the near-field of a mesoscopic metallic particle: distance dependence and role of plasmon modes," Opt. Express **16**, 17654 (2008). 69, 70, 73

[93] C. Vandenbem, D. Brayer, L. S. Froufe-Pérez, and R. Carminati, "Controlling the quantum yield of a dipole emitter with coupled plasmonic modes," Phys. Rev. B **81**, 085444 (2010).

[94] M. Ringler, A. Schwemer, M. Wunderlich, A. Nichtl, K. Kürzinger, T. A. Klar, and J. Feldmann, "Shaping emission spectra of fluorescent molecules with single plasmonic nanoresonators," Phys. Rev. Lett. **100**, 203002 (2008). 70, 91

[95] A. Alù and N. Engheta, "Hertzian plasmonic nanodimer as an efficient nanoantenna," Phys. Rev. B **78**, 195111 (2008). 70

[96] T. H. Taminiau, F. D. Stefani, F. B. Segerink, and N. F. van Hulst, "Optical antennas direct single-molecule emission," Nat. Photon. **2**, 234–237 (2008). 70, 73

[97] P. Mühlschlegel, H.-J. Eisler, O. J. F. Martin, B. Hecht, and D. W. Pohl, "Resonant optical antennas," Science **308**, 1607 (2005). 70

[98] J.-J. Greffet, "Antennas for light emission," Science **308**, 1561 (2005).

[99] P. Bharadwaj, B. Deutsch, and L. Novotny, "Optical antennas," Adv. Opt. Photon. **1**, 438–483 (2009). 70, 71

[100] A. F. Koenderink, "Plasmon nanoparticle array waveguides for single photon and single plasmon sources," Nano Lett. **9**, 4228–4233 (2009). 70, 74, 79, 83, 85, 88, 92

[101] P. Bharadwaj and L. Novotny, "Spectral dependence of single molecule fluorescence enhancement," Opt. Express **15**, 14266 (2007). 73, 93

[102] H. Gersen, M. F. Garcia-Parajo, L. Novotny, J. A. Veerman, L. Kuipers, and N. F. van Hulst, "Influencing the angular emission of a single molecule," Phys. Rev. Lett. **85**, 5312–5315 (2000). 73

[103] S. Kuhn, G. Mori, M. Agio, and V. Sandoghdar, "Modification of single molecule fluorescence close to a nanostructure: radiation pattern, spontaneous emission and quenching," Molecular Physics **106**, 893–908 (2008). 73

[104] J. Li, A. Salindrino, and N. Engheta, "Shaping light beams in the nanometer scale: A Yagi-Uda nanoantenna in the optical domain," Phys. Rev. B **76**, 245403 (2007). 74, 75, 79, 85, 86, 92

[105] H. F. Hofman, T. Kosako, and Y. Kadoya, "Design parameters for a nano-optical Yagi-Uda antenna," New J. Phys. **9**, 217 (2007). 74, 75, 79, 86

[106] T. Pakizeh and M. Käll, "Unidirectional ultracompact optical antennas," Nano Lett. **9**, 2343–2349 (2009). 74, 82

[107] M. Lax, "Multiple scattering of waves," Rev. Mod. Phys. **23**, 287–310 (1951). 75

[108] W. J. Wiscombe, "Improving Mie scattering algorithms," Appl. Opt. **19**, 1505–1509 (1980). 75

[109] T. H. Taminiau, F. D. Stefani, and N. F. van Hulst, "Enhanced directional excitation and emission of single emitters by a nano-optical Yagi-Uda antenna." Opt. Express **16**, 16858–16866 (2008). 79, 83, 85, 92

[110] T. Kosako, Y. Kadoya, and H. F. Hofmann, "Directional control of light by a nano-optical Yagi-Uda antenna," Nat. Photon. **4**, 1–4 (2010). 79, 85, 86, 88, 92

[111] J. Seelig, K. Leslie, A. Renn, S. Kuhn, V. Jacobsen, M. van de Corput, C. Wyman, and V. Sandoghdar, "Nanoparticle-induced fluorescence lifetime modification as nanoscopic ruler: Demonstration at the single molecule level," Nano Lett. **7**, 685–689 (2007). 80

[112] C. Huang, A. Bouhelier, G. C. des Francs, A. Bruyant, A. Guenot, E. Finot, J. C. Weeber, and A. Dereux, "Gain, detuning, and radiation patterns of nanoparticle optical antennas," Phys. Rev. B **78** (2008). 81

[113] A. G. Curto, G. Volpe, T. H. Taminiau, M. P. Kreuzer, R. Quidant, and N. F. van Hulst, "Unidirectional emission of a quantum dot coupled to a nanoantenna," Science **329**, 930–933 (2010). 85, 86, 88

[114] B. J. Soller, H. R. Stuart, and D. G. Hall, "Energy transfer at optical frequencies to silicon-on-insulator structures," Opt. Lett. **26**, 1421–1423 (2001). 85

[115] J. J. Schwartz, S. Stavrakis, and S. R. Quake, "Colloidal lenses allow high-temperature single-molecule imaging and improve fluorophore photostability," Nature Nanotechnol. **5**, 127–132 (2009). 85, 89, 90

[116] G. Pellegrini, G. Mattei, and P. Mazzoldi, "Light extraction with dielectric nanoantenna arrays," ACS Nano **3**, 2715–2721 (2009). 85

[117] M. Quinten, A. Leitner, J. R. Krenn, and F. R. Aussenegg, "Electromagnetic transport via linear chains of silver nanoparticles," Opt. Lett. **23**, 1331–1333 (1998). 88

[118] S. A. Maier, M. L. Brongersma, P. G. Kik, and A. Atwater, "Observation of near field coupling in metal nanoparticle chains using far-field polarization spectroscopy," Phys. Rev. B **65**, 193408 (2002). 88

[119] W. H. Weber and G. W. Ford, "Propagation of optical excitations by dipolar interactions in metal nanoparticle chains," Phys. Rev. B **70**, 125429 (2004). 88

[120] Y. Yamada, H. Uyama, S. Watanabe, and H. Nozoye, "Deposition at low substrate temperatures of high-quality TiO_2 films by radical beam-assisted evaporation," Appl. Opt. **38**, 6638–6641 (1999). 89, 91

[121] K. Koyama, M. Yishita, M. Baba, T. Suemoto, and H. Akiyama, "High collection efficiency in fluorescence microscopy with a solid immergion lens," Appl. Phys. Lett. **75**, 1667–1669 (1999). 90

[122] J. Merlein, M. Kahl, A. Zuschlag, A. Sell, A. Halm, J. Boneberg, P. Leiderer, A. Leitenstorfer, and R. Bratschitsch, "Nanomechanical control of an optical antenna," Nat. Photon. **2**, 230–233 (2008). 92

[123] R. Carminati, M. Nieto-Vesperinas, and J.-J. Greffet, "Reciprocity of evanescent electromagnetic waves," J. Opt. Soc. Am. A **15**, 706–712 (1998). 93